Density functional theory studies of Fe and Mn substituted $CoCr_2O_4$

Debashish Das

Supervisor: Prof. Subhradip Ghosh

Department of Physics
Indian Institute of Tecnology Guwahati

This dissertation is submitted for the degree of
Doctor of Philosophy

November 2017


Indian Institute of Technology Guwahati

I would like to dedicate this thesis to my loving parents . . .

Declaration

I hereby declare that, the work in this thesis is based on research carried out at the Department of Physics, Indian Institute of Technology Guwahati, India under the supervision of Dr. Subhradip Ghosh. No part of this thesis has been submitted elsewhere for any other degree or qualification. Works presented in the thesis are all my own unless referenced to the contrary in the text.

Debashish Das
November 2017

Certificate

It is certified that the work contained in the thesis titled “Density functional theory studies of Fe and Mn substituted $CoCr_2O_4$” by Mr. Debashish Das , a student of the Department of Physics, IIT Guwahati was carried out under my supervision and has not been submitted elsewhere for award of any degree.

Prof. Subhradip Ghosh
November 2017

Acknowledgements

First I express my sincere gratitude to my thesis supervisor Prof. Subhradip Ghosh for giving me the opportunity to work under him. I have learned the basic concepts of Density functional theory from him. I am very much grateful to him for his guidance, finding appropriate problems for my thesis, revising my manuscripts and annual progress seminar reports and correcting my thesis detailed with great patience. I must thank him for his constant support and motivations.

I would also like to acknowledge my doctoral committee members Dr. Dillip Pal, Dr. P. K. Padmanabhan and Dr. Sandip Paul who examined my PhD work and made me improve by making valuable suggestions. I would also like to thank to our HOD Prof. P. Poulose and our former HODs Prof. Saurabh Basu and Prof. S. Ravi for departmental supports. I would like to thank all the office staff in Physics Department and special thanks to Basabda for his technical help.

I would also like to acknowledge Dr. Biplab Sanyal and Dr. Shreemoyee Ganguly from Uppsala University, Sweden for their collaborative efforts because without them my thesis would not have been complete. I would also sincerely thank Dr. Dilip Pal as the experimental studies had been done by him and his student, Padam bhaiya, which I had taken up for theoretical study and latter we had great collaboration with him and his students, Ram and Padam bhaiya. This collaboration has great impact on my research and help me to understand the problem from the experimentalists perspective. I would also like to thank my senior Souvikda as I have learned a lot. I would also like to acknowledge my super senior Dr. Biswanath Dutta as I have learnt the calculations on phonon studies by working with him. I am also thankful to some of the talks and lectures by our department faculties Dr. Charudatt Y Kadolkar, Prof. Saurabh Basu, Prof. Perumal Alagarsamy and Prof. Girish Setlur which have strong impacts on my understanding of condensed matter physics. I also like to thank SINC-HPC2N, Sweden, CDAC, Pune, and Numerical laboratory, Department of physics, IIT Guwahati for access of their HPC facilities. I would also like to thank MHRD for financial support during my PhD period.

I would like to thank my group juniors Asish, Srikrishna and Sheuly with whom I have shared many experience and also learnt by discussing with them. I would like to thank my batchmates Kartik, Tapas, Arnab, Biplob, Sandeep, Sabuj, Charan, Debashish Sarkar, Santa, Gyan, Bipul, Samit, Ranganath, Ramakrishna and Mahesh for creating friendly environment. I thank my seniors Bhagaban bhai, Bisuda, Rameshda and Obida for their help and suggestions. I must thank all my juniors Shibananda, Omkar, Ramiz, Kallol, Pratap, Kajwal, Indu, Nawaz, Joy, Sunyanana, Sasmita and others for their constant support and help. I also like to thank Santosh Bhai, Pradeep Bhai, Harikrushna and Ananda for making my hostel life easier.

I must also mention that I have very good friends in my MSc days Radhanath, Udaya, Jyotiprakash, Abhaya, Purna, Girija, Aparna and Parbati from whom I learned and got inspired. I am very grateful to have some of great teachers Prof. Karmadev Maharana, Prof. Naresh Mishra and Prof. Lambodar Prasad Singh in my MSc days who are my sources of inspiration.

Last but not least, I want to thank my family for unconditional love and support. I would also like to thank my elder brother Subhasis Das for taking care of my family, which made me focus on my PhD work.

Abstract

Spinel compound $CoCr_2O_4$ is found to be a promising multiferroic material as it exhibits switchable electric polarization under reversal of magnetic field. In a bid to enhance the functional properties of $CoCr_2O_4$, recent experiments attempted substitution of Cr by a another magnetic atom. Substitution of Fe and Mn in place of Cr led to fascinating phenomena like temperature and composition dependent magnetic compensations, magnetostrsiction effects, composition dependent tunable exchange bias which are not observed in pristine $CoCr_2O_4$. The experimental results on various thermal, structural and magnetic properties in Fe and Mn substituted $CoCr_2O_4$ implied that there can be significant cation disorder present in these systems which renormalizes the magnetic exchange interactions and in turn is responsible for the anomalous behavior of the physical quantities with changes in the compositions of the system. In order to gain fundamental understandings into various effects like the cation disorder, the crystal fields, the magnetic exchange interactions and their interplay, the electron-electron correlations, the spin-lattice coupling on the properties of these systems and thus provide interpretations of the available experimental results, in this dissertation. We have performed systematic investigations into the structural, electronic and magnetic and vibrational properties of $Co(Cr_{1-x}Fe_x)_2O_4$, 0≤x≤1, with first-principles Density functional theory (DFT) based DFT+U method. Our investigations into the pristine compounds $CoCr_2O_4$, $CoMn_2O_4$ and $CoFe_2O_4$ demonstrated the changes in their electronic structures as one of the magnetic component is changed systematically, and thus helped in understanding the roles of crystal fields, magnetic exchanges, structural distortions, electron-electron correlations. Such fundamental understanding helped in interpreting thee differences in their ground state magnetic structures as well and provided enough insights into the possible scenario when one of the magnetic atom is substituted with the other. Our investigations into $Co(Cr_{1-x}Fe_x)_2O_4$, 0≤x≤1 quantified the degree of cation inversion at each composition and for a range of temperatures. Based upon this, calculations of the structural properties and the magnetic exchange interactions enabled us to discover the roles of sites-occupancies in influencing, in particular, the emergence of a collinear magnetic order from a non-collinear one with increase in the Fe content in the system. The electronic structures as a function of composition and degree of cation inversion provided the micro-

scopic picture of the competing magnetic exchange interactions and thus a complete picture of the physical mechanism of the magnetic properties in this system. In a similar way, $Co(Cr_{1-x}Mn_x)_2O_4$, 0≤x≤1, was investigated. The variations in the degree of cation inversion in this system was non-regular in comparison to that with $Co(Cr_{1-x}Fe_x)_2O_4$. We found that the non-regular variations in the degree of cation disorder can be used to explain the experimentally observed non-regular variations in the magnetization, and in particular the phenomena of composition dependent magnetic compensations. We showed that the cation disorder affects the charge state, and the impart substantial influence on the variations in the overall physical properties in this system. The information on the fundamental mechanisms in these two substituted systems could be achieved due to quantification of the degree of cation disorder, for which we generalized an existing thermodynamic model and coupled it with first-principles calculations. This development is a significant contribution in this dissertation. A quest into the effects of cation disorder onto the vibrational properties in these systems, further led to a qualitative understanding of the effects of symmetry lowering due to chemical substitution and degree of cation inversion on the phonon dispersion in pristine and substituted $CoCr_2O_4$. As a further exploration into the possible coupling between magnetic and the lattice degrees of freedom, as suggested in experiments, we generalized an existing model to compute the spin-phonon coupling strength in AB_2O_4 spinels having two magnetic atoms. The result identified the vibrational modes and associated atom pairs responsible for significant spin-phonon coupling. Overall, the results presented in this thesis shed enough light on the interplay of various factors and their role in influencing the physical properties in these multi-functional systems.

Table of contents

List of figures

List of tables

Chapter 1

Introduction

Recent years have seen an enormous increase in research activity on functional materials, systems which possess particular native properties and functions of their own. Examples are ferroelectricity, piezoelectricity, magnetism and energy storage functions. In order to achieve enhanced functional properties in existing materials, or to discover new systems with better functionalities, material scientists have tried different tricks such as forming an alloy or a composite, growing hetrostructures, growing the materials in thin-film etc. In many cases they have succeeded in obtaining what was sought for. Magnetic materials, although had always received considerable attention, have recently seen a surge in the interests in them. This has happened after new and novel functionalities like spintronics applications [110, 10], magnetic shape memory applications[132] and magneto-caloric applications [122] have been discovered. The magnetism driven functionalities are gaining currency due to the fact that the response of the spin degrees of freedom are much faster to the charge degrees of freedom, and hence are more desirable in device applications. Functionalities of these devices are further boosted up if materials exhibit more than one ferroic ordering. Recent discovery of multiferroic materials, in which there is a coupling between magnetic and electric degrees of freedom is one prime example of such novel functional properties. In fact, this discovery has triggered significant interests and hence large scale investigations of various magnetic materials as the strong magnetoelectric coupling in multiferroics is potentially useful for application in capacitors, sensors and data storage devices.

Oxides materials are an important class of systems which have displayed their usefulness in multiple applications. They have been successfully utilized as diodes[22], sensors[53], solar cells[18], transport conductors[3], organic photovoltaic[145], and random asses memories[65]. The transition metal oxides where at least one of the constituents in a transition metal, have a very special place among the research community working on oxides. It is because of the fact that these materials exhibit strong electron-electron correlations which helps understanding phenomena such as metal-insulator transitions and properties such as high-temperature superconductivity and colossal magnetoresistances. The orbital degrees of freedom occasionally play an important role in these phenomena and its correlation causes a variety of phenomena through strong coupling with charge, spin and lattice dynamics[123].

Oxides with the spinel structure are some of the most studied substances in the solid state sciences. This is because of the fact that there is abundance of oxide materials in spinel structure which have a simple chemical formula of AB_2O_4 with A and B are cation of either charge states 2+ and 3+ or of 4+ and 2+ [87]. The abundances of spinel compounds is partly because the structure can accommodate very large number of cations of different valencies. The spinel oxides are among some of very important magnetic materials[119, 67, 99, 137] and refractories[9]. Magnesium based spinels are found to be substantially constitute the earth's mantle, while Iron-titanium spinel are important component to understand rock's magnetism. The magnetic spinel oxides form a sub-class of system in the broader class of oxides which are structurally simple, can accommodate large number of different degrees of freedom as has been mentioned earlier. In the next few subsections, we outline various basic concepts to understand the fundamental physics of the magnetic spinel oxides.

1.1 Concepts to understand the fundamental physics of magnetic spinel oxides

In this section, we discuss various basic concepts required to understand the structure-property relationships in magnetic spinel oxides.

1.1.1 The crystal structure

The spinel structure can be described with space group Fd$\bar{3}$m (space group 225). The structure can be described as an approximately close-packed arrangement of oxygen anions with the metal cations distributed among the A sites having tetrahedral symmetry (and hence also called tetrahedral sites) and the B sites having octahedral symmetry (and hence called octahedral sites). The cations at the tetrahedral sites forms a diamond structure and those at the octahedral sites forms a pyrochlore structure. The smallest unit cell of the spinel structure can, thus, be described with a 14 atom cell. The crystal structure is shown in Figure1.1 and the positions in the unit cell are listed in Table 1.1

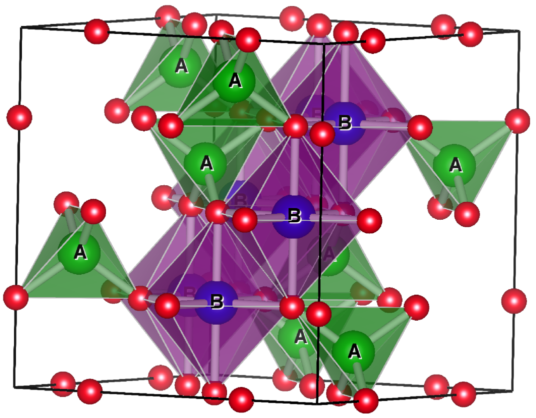

Fig. 1.1 The crystal structure of spinel compound AB_2O_4. The A, B and oxygen atoms are shaded in green, purple and red respectively. The B atoms are in octahedral positions and A atoms are in tetrahedral positions.

Table 1.1 The positions of the atoms (in fractional crystallographic coordinates), in an unit cell of spinel structure. The Wyckoff positions are also given.

Type of atom	position of the atoms	Wyckoff position in $Fd\bar{3}m$ space group
A_1	7/8 7/8 7/8	8a
A_2	1/8 1/8 1/8	
B_1	1/2 1/2 1/2	16d
B_2	0 1/2 1/2	
B_3	1/2 0 1/2	
B_4	1/2 1/2 0	
O_1	1/4 1/4 1/4	32e
O_2	3/4 1/4 1/4	
O_3	1/4 3/4 1/4	
O_4	1/4 1/4 3/4	
O_5	3/4 3/4 3/4	
O_6	1/4 3/4 3/4	
O_7	3/4 1/4 3/4	
O_8	3/4 3/4 1/4	

1.1.2 Magnetic Geometrical Frustration

The energy of magnetic interaction, E, between two neighbouring atoms denoted by their spin vectors S_i and S_j can be expressed as

$$E = -J_{ij}(\vec{S}_i.\vec{S}_j)$$

.

J_{ij} is the magnetic exchange parameter and decides the magnetic order of the system. If $J_{ij} > 0$, the interaction is ferromagnetic and if $J_{ij} < 0$, the interaction is antiferromagnetic. For ferromagnetic interactions, all the spins align in the same direction and the ground state can be easily determined. In case of antiferromagnetic interaction between neighbouring spins, a problem occurs, for examples, in case of triangular networks. If one has to consider antiferromagnetic interaction (antiparallel alignment) between two sets of neighbours, then the alignment of the remaining set of neighbour will always be parallel. Thus, the system fails to minimize the energy of all pairwise magnetic interactions simultaneously. This leads to an infinite number of possible ground states. The appearance of such frustration in spin is due to the geometrical constrains and is called Magnetic geometrical Frustration[30]. The main outcome of this frustration is the inability of the system to form a collinear magnetic ground states, thus leading to emergence of unconventional non-collinear ground states[6, 42].

The diamond structure, which the tetrahedrally coordinated A cations in AB_2O_4 spinels form, can be thought of as corner shared triangles in one dimension. The pyrochlore lattice formed by the B cations, on the other hand, can be thought of as corner shared tetrahedra. As a result, if both A and B cations are magnetic, the magnetic geometrical frustration is bound to be present in both sub-lattices. In case of only the B cations are magnetic, the geometry causes unusual magnetic frustration leading to emergent excitations of spin states. Prime examples are $ZnCr_2O_4$[66] and $CdCr_2O_4$[23] where the macroscopic degeneracy caused by the frustration is lifted by lowering of the lattice symmetry, resulting in complicated non-collinear spin structures. In case only the A cations are magnetic, frustration due to competing nearest neighbour and next nearest neighbour magnetic exchange interactions lead to non-collinear magnetic ground states. Examples of this kind are $MnAl_2O_4$, $FeAl_2O_4$ and $CoAl_2O_4$[51],[73].

If both A and B cations are magnetic, then the interaction between A and B cations provide an alternative to release the frustration associated with the pyrochlore lattice. This happens when the A-B exchange interactions compete with the B-B interactions. This reduces the magnetic geometric frustration to a reasonable extent and is known as “Weak Magnetic Geometrical Frustration”[124].

1.1.3 Elements of crystal field theory

The crystal field theory[78] describe the effects of environment on the energetics of solids with predominantly electrostatic interactions among its constituents. This, thus, is quite useful in describing nearly ionic crystals like the transition metal oxides. When a transition-metal cation is surrounded by six anions such as oxygen, in a regular octahedral arrangements, the five cation d-orbitals no longer remain degenerate but split into two groups: a lower triplet t_{2g} (d_{xy},d_{yz} and d_{zx}) and an upper doublet e_g ($d_{x^2-y^2}$ and d_{z^2}). The physical basis of such splitting is purely electronic repulsion between the d-electrons and the surrounding anions. The e_g orbitals, in an octahedral environment, point directly at the anions and their energy increase due to the direct repulsion. The t_{2g} orbitals, on the other hand points in the directions where the field is least and thus can get away with lower energies. The difference in energy between the two sets of orbitals, Δ_o is called the octahedral crystal field[12]. In case of a tetrahedral environment, the order of the t_{2g} triplet and e_g doublet are reversed with respect to the octahedral case[17],[32]. The corresponding tetrahedral crystal field, Δ_t, is actually smaller, the relation between the two crystal fields being,

$$\Delta_t = -\frac{4}{9}\Delta_o \tag{1.1}$$

The crystal fields are founds to be dependent on the cation-anion distance a, the following way

$$\Delta \propto a^{-5} \tag{1.2}$$

Thus, in case of a smaller cation-anion distance, the strength of the crystal field increases rapidly, and vice versa.

As electrons are gradually inducted into the d-shells, they occupy the lowest available orbitals. Thus the electronic configurations of the d-electron associated with octahedral crystal fields are $(t_{2g}^m)(e_g^n)$; m, n are integers, in general while the electronic configurations associated with tetrahedral crystal fields are $(e_g^m)(t_{2g}^n)$ in general [Table 1.2]. However, in case of d^4-d^7configurations with octahedral environments, the sub-shells can be filled in two different ways. If the energy require to pair two electrons, P, known as pairing energy is smaller than Δ_o, then after filling up of the t_{2g} orbitals corresponding to one spin direction, the electrons instead of filling up the e_g orbitals, fill up the t_{2g} levels corresponding to the other spin direction, thus leading to a low-spin state. Otherwise, the usual filling up of orbitals gradually leads to a high-spin state. Example are shown in Table 1.2. This does not happen in tetrahedral environments, as Δ_t is lower than Δ_o and thus the order of magnitude of P is never lower than that of Δ_t.

Two important quantities that are associated with the formation of transition metal oxides in spinel structure are the crystal field stabilization energy (CFSE) and the octahedral site preference energy (OSPE). The CFSE is defined as the difference between the total electronic energy of a cation in presence of crystal field and that of a cation in an isotropic field.

$$CFSE = E_{crystal field} - E_{isotropic field} \tag{1.3}$$

The CFSE can be computed in terms of Δ_t and Δ_o in cases of tetrahedral and octahedral field respectively. The CFSE for different d-shell configurations are tabulated in Table 1.2. The OSPE, on the other hand, signifies the preference of a cation to occupy the sites with octahedral symmetry, and is defined as

$$OSPE = CFSE_{oct} - CFSE_{tet} \tag{1.4}$$

where $CFSE_{oct}$ and $CFSE_{tet}$ stand for CFSE associated with octahedral and tetragonal sites. A positive value of OSPE would imply that the cation has a preference for the octahedral sites. From the calculation of CFSE and OSPE, the site preference of various cation in various charge states have been successfully predicted[75].

1.1.4 Jahn-Teller distortion

Jahn and Teller have shown[48] that if the electronic state of a non-linear molecule is orbitally degenerate then its ground state will undergo a geometrical distortion that removes orbital degeneracy. The extent of such distortion depends on the bonding and anti bonding power of the degenerate electrons.

In order to illustrate, we take the example of an octahedrally coordinated d^7 cation with electronic configuration ($t_{2g}^6 e_g^1$). In this case, the t_{2g} levels are completely filled and e_g levels are degenerate. The degeneracy is lifted by invoking an elongation along the z-axis and a simultaneous contraction in the xy-plane. As simple electrostatic argument tells us that this will split the e_g levels into d_z^2 and $d_{x^2-y^2}$ levels where d_z^2 levels are somewhat stabilized (due

Table 1.2 The configurations of d-shells for high spin and low spin situations, The Crystal field stabilization energy(CFSE) and octahedral site preference energy (OSPE) of $d^1 - d^{10}$ are tabulated for both octahedral and tetrahedral environments[20]. For each electronic configuration, the strength of Jahn teller distortion is given. We refers to “weak distortion”, S stands for “strong distortion”[32].

	Octahedral						Tetrahedral			
	High spin			Low spin			High spin			
	Config.	dist.	CFSE	Config.	dist.	CFSE	Config.	dist.	CFSE	OSPE
d^1	$(t_{2g})^1$	W	$-2/5\Delta_o$				$(e_g)^1$	W	$-3/5\Delta_t$	$-6/45\Delta_o$
d^2	$(t_{2g})^2$	W	$-4/5\Delta_o$				$(e_g)^2$	-	$-6/5\Delta_t$	$-12/45\Delta_o$
d^3	$(t_{2g})^3$	-	$-6/5\Delta_o$				$(e_g)^2(t_{2g})^1$	S	$-4/5\Delta_t$	$-38/45\Delta_o$
d^4	$(t_{2g})^3(e_g)^1$	S	$-3/5\Delta_o$	$(t_{2g})^4$	W	$-8/5\Delta_O+P$	$(e_g)^2(t_{2g})^2$	S	$-2/5\Delta_t$	$-19/45\Delta_o$
d^5	$(t_{2g})^3(e_g)^2$	-	0	$(t_{2g})^5$	W	$-10/5\Delta_O+2P$	$(e_g)^2(t_{2g})^3$	-	0	0
d^6	$(t_{2g})^4(e_g)^2$	W	$-2/5\Delta_o$	$(t_{2g})^6$	-	$-12/5\Delta_O+P$	$(e_g)^3(t_{2g})^3$	W	$-3/5\Delta_t$	$-6/45\Delta_o$
d^7	$(t_{2g})^5(e_g)^2$	W	$-4/5\Delta_o$	$(t_{2g})^6(e_g)^1$	S	$-9/5\Delta_O+P$	$(e_g)^4(t_{2g})^3$	-	$-6/5\Delta_t$	$-12/45\Delta_o$
d^8	$(t_{2g})^6(e_g)^2$	-	$-6/5\Delta_o$				$(e_g)^4(t_{2g})^4$	S	$-4/5\Delta_t$	$-38/45\Delta_o$
d^9	$(t_{2g})^6(e_g)^3$	S	$-3/5\Delta_o$				$(e_g)^4(t_{2g})^5$	S	$-2/5\Delta_t$	$-19/45\Delta_o$
d^{10}	$(t_{2g})^6(e_g)^4$	-	0				$(e_g)^4(t_{2g})^6$	-	0	0

to its lower energy) and $d_{x^2-y^2}$ completely destabilized. The single electron thus fills only the d_z^2 orbital leaving $d_{x^2-y^2}$ empty. This deviation from the regular octahedral symmetry stabilizes the complex and the distortion proceeds till the extra stability gained this way is balanced by the energy required to distort the bonds. For the octahedral coordination, the t_{2g} orbitals are relatively non-bonding and thus small distortions are expected from configurations that are degenerate with respect to t_{2g} orbitals. However, significant distortions are expected for configurations having degeneracy with respect to e_g orbitals. Due to the orientations of the splitted e_g levels, that is since they are directed towards the negative charged ions (compare $d_{x^2-y^2}$ with d_{xy} in Figure 1.3), pure electrostatic consideration validates the larger distortion associated with degenerate e_g levels. Table 1.2 summarizes this assertion. In tetrahedral environments, it is the e_g orbitals which are relatively non-bonding. Once again, this can be understood from the orientations of the orbitals as depicted in Figure 1.3. Thus large distortions from regular tetrahedral symmetry are expected for configurations which are degenerate with respect to t_{2g} orbitals only. The full list of possible configurations and expected distortions are listed in Table 1.2. Upon tetragonal distortion, the splitting and subsequent positioning of the splitted levels associated with either e_g or t_{2g} orbitals depend on the ratio c/a. In Figure 1.2, a schematic energy level diagram of the d-orbitals under different crystal fields is shown.

In a cubic crystal where one can visualize the system as a collection of ions arranged in a cubic lattice, the effect of Jahn-Teller distortion would mean that each ion will undergo a set of equivalent distortions and if these are not too large, the neighboring ions would not be influenced by each other. Under these circumstances, the overall cubic symmetry of the lattice would be retained as at any point of time each ion will be in one of three equivalent distorted configurations (one along each of the cubic axes) independent of the state of its neighbours. If the distortions are substantial, the neighboring ions will influence each other and the lattice would minimize the energy by adjusting itself to a lower symmetry, giving rise to a deviation from the ground state. This picture has been confirmed from the ground state experimental structures of many oxides with spinel structure [32]. Thus Jahn-Teller mechanism is an useful tool to understand the structural aspects of spinel compounds.

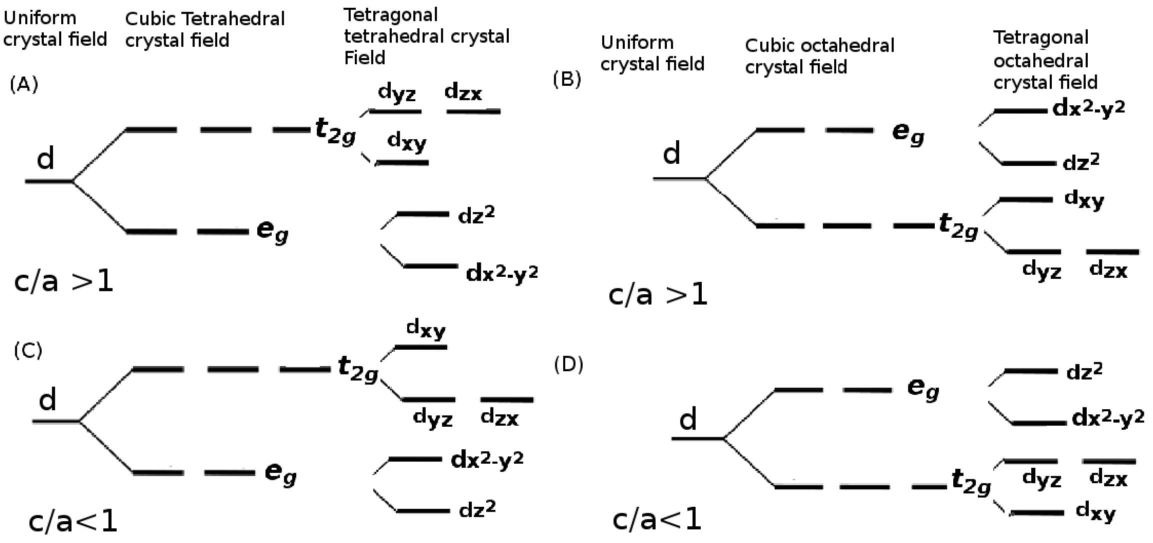

Fig. 1.2 Schematic energy level diagram of d-levels under various crystal fields and tetragonal distortions. (A) and (C) stands for tetrahedral crystal fields while (B) and (D) are for octahedral crystal fields.

1.1.5 Hybridisations and magnetic exchange interactions

Figure 1.3 depicts the directions of various d-orbitals in a magnetic oxide in spinel structure. One can clearly see that the e_g orbitals associated with the octahedral sites and the t_{2g} orbitals associated with the tetrahedral sites point directly towards the anion O^{2-} and hence hybridisation between these d-orbitals and the p-orbitals of O^{2-} are possible. Such hybridisations are responsible for the indirect cation-cation interactions (super exchange). The hybridisation between e_g orbitals of the nearest neighbor octahedral cation via the oxygen p-orbitals give rise to cation-anion-cation 90° B-B super exchange. Similarly, hybridisations between t_{2g} orbitals of tetrahedral cations and e_g orbitals of octahedral cations via the oxygen p state lead to cation-anion-cation 125° A-B super exchange. Apart from such indirect interactions, the other substantial magnetic interaction takes place due to the hybridisations of t_{2g} orbitals of nearest neighbor octahedral cations, known as B-B direct interaction. The relative strengths of these various magnetic interactions are decided by the configurations of the cation d-orbitals. Using simple electrostatic consideration, Goodenough[136] provided an estimation of the strengths of different exchange interactions. The fundamental equations are:

$$J_{ij}^{c-c}(halffilled,halffilled) = -2b_{ij}^2/4S^2U \tag{1.5}$$

$$J_{ij}^{c-c}(halffilled,empty) = +2b_{ij}^2 J^{intra}/4S^2U^2 \tag{1.6}$$

$$J_{ij}^{c-c}(halffilled,full) = +2b_{ij}^2 J^{intra}/4S^2U^2 \tag{1.7}$$

J_{ij}^{c-c} is the cation-cation exchange interaction between sites i and j, b_{ij} is the transfer integral, S is the spin of the Cation, U is the energy difference between excited states with one transferred electron and the ground state, J^{intra} is the exchange integral associated with two different orbitals of the same cation. Equations 1.5-1.7 respectively stand for the cases when both cation orbitals are half-filled, one is half filled and the other is empty, one is half filled and other is full. Based upon these equations, postulates about relative strength of exchange interactions in a spinel are coined as follows[135][136]:

1. If both tetragonal(A) t_{2g} and octahedral(B) e_g orbitals are half filled (or less than half filled and degenerate), then A-B interaction (tetrahedral-octahedral) is strongly antiferromagnetic.

2. If tetrahedral t_{2g} and/or octahedral e_g orbitals are empty, the A-B interaction is relatively weaker and antiferromagnetic.

3. If octahedral(B) t_{2g} orbitals are half filled (or less than half filled and degenerate), direct B-B interaction is possible. The strength of these antiferromagnetic interactions depend strongly on inter-cation distances and anion shielding.

4. If the t_{2g} orbitals of neighboring octahedral sites (one or both of two cations) are full (or more than half-full degenerate), no direct B-B direct interactions occur between them.

5. For the case of cation-anion-cation 90° super exchange, the sign of interaction varies with situation. Using equation 1.5-1.7 the interactions can be calculated.

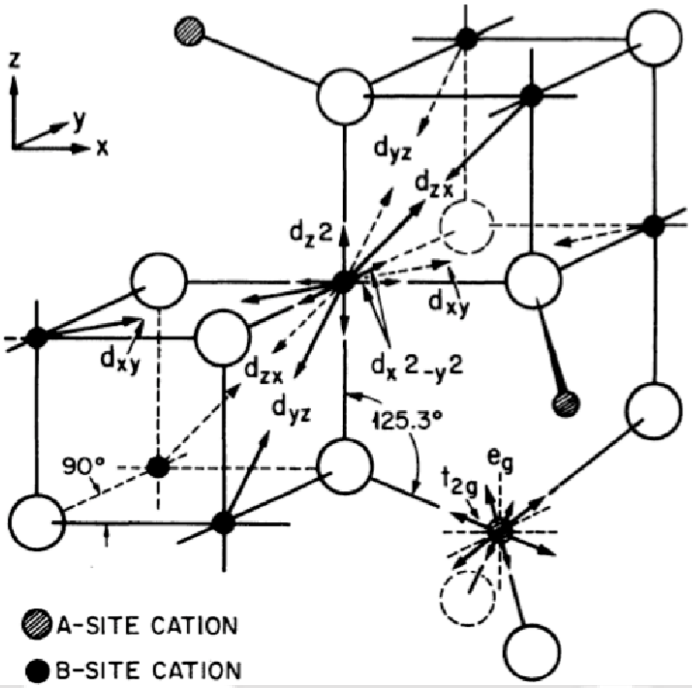

Fig. 1.3 Figure shows a schematic diagram of spinel structure and the direction of d-orbitals in octahedral and tetrahedral environments[136].

1.1.6 Degree of cation disorder

The fascinating structure-property relationships and consequent controlled engineering of functional properties in oxide spinels are understood to be due to the presence of significant cation disorder over the two cation sublattices[58, 77, 5, 25, 133, 115, 16, 19, 44]. The spinel is considered to be cation-disordered when there is considerable mixing of A and B cations. The degree of cation disorder, also known as "inversion parameter", is represented by a single parameter y which can take values between 0 and 1. The spinels in which there is no mixing of A and B cations are termed "Normal spinels" with y=0. The other extreme is the case of "inverse spinels" with y=1 where tetrahedral sites are occupied by the B atoms while the octahedral sites are occupied by equal amounts of A and B atoms. Thus, a general representation of AB_2O_4 spinels with cation disorder is $(A_{1-y}B_y)[B_{1-y/2}A_{y/2}]_2O_4$. The degree of cation disorder in a material depends on experimental conditions such as the annealing temperature[15, 76, 86] or the control of the non-equilibrium disorder[84]. Various studies on different spinels have established that the electrical[50, 84], electronic[129] and thermal[106, 101] properties of these compounds can be controlled by manipulations of their degrees of cation disorder. Thus, a precise knowledge about the degree of cation disorder in a spinel compound is very important to understand its fundamental properties. In Table 1.3, we list a few prominent magnetic spinels with their degrees of cation disorder. The results listed show that different investigations on the same compound yielded different values of the inversion parameter y. This implies that the inversion parameter is extremely sensitive to the experimental conditions for example, the heat treatment.

Table 1.3 The degree of cationic disorder for various spinel compounds.

Compound	y	Reference
$FeCr_2O_4$	0.0	[8],[105],[99]
$FeCr_2S4$	0.0	[105],[99]
$FeMn_2O_4$	0.5	[60],[108]
	0.9	[16], [19],[99]
$FeMn_2S_4$	0.3	[111]
$FeCo_2O_4$	0.5	[38]
	0.6	[69],[118]
	0.7	[79]
	1.0	[118], [38],[99]
$FeCo_2S_4$	0.5	[99]
$CoFe_2O_4$	0.8	[38],[63]
	0.6	[79],[80]
$CoMn_2O_4$	0.4	[15]
	0.2	[41]

1.2 The pristine and substituted $CoCr_2O_4$

The magnetic oxide material $CoCr_2O_4$ has been the subject of intense investigations in recent times after the discovery of its multiferroic properties (coexistence and coupling of ferroelectricity and ferromagnetism)[140]. The magnetic phase diagram of this material is quite rich and versatile. At 97 K, a paramagnetic to a collinear ferrimagnetic transition is found to occur in this system. Below 87 K, the magnetic structure consists of a short range conical spiral. Ferroelectric transition is detected at 25 K below which it develops an incommensurate long range conical spin order. The direction of the spontaneous electric polarization is normal to both magnetization easy axis and the direction of propagation of spin spirals. A further transition from the incommensurate to a commensurate sprial state is found to occur at 14 K[127]. The origin of the devlopment of the non-collinear spiral states is believed to be due to magnetic geometric frustration. The electric polarisation developed in the system can be well understood by both spin current model and the theory of inverse Dzyaloshinskii-Moriya interaction [140] . The magneto-electric coupling, thus can be expressed as,

$$P = a\hat{e}_{ij} \times (\vec{S}_i \times \vec{S}_j) \tag{1.8}$$

where, $\vec{S}_i$ and $\vec{S}_j$ are the spins at i and j, $\hat{e}_{ij}$ is the vector joining the spins. This clearly shows how a switchable electric polarisation can be obtained in this material by reversing the magnetic field.

The complicated magnetic structures of $CoCr_2O_4$ at low temperature has made it a candidate for testing analytical models which based upon magnetic exchange parameters, can provide an idea about the magnetic structure. In case of cubic spinel compound, one such model was proposed by Lyons, Kaplan, Dwight, and Menyuk [72]. Using a model of classical Heisenberg spins and considering only the BB and AB nearest neighbour magnetic interaction, this model, known as LKDM, showed that the ground state magnetic structure is determined by the parameter

$$\tilde{u} = \frac{4J_{BB}\vec{S}_B.\vec{S}_B}{3J_{AB}\vec{S}_A.\vec{S}_B} \tag{1.9}$$

J_{BB}, J_{AB} are the exchange interactions between nearest neighbor octahedral-octahedral(BB) and tetrahedral-octahedral(AB) pairs respectively, $\vec{S}_A$ and $\vec{S}_B$ are the spin vectors at the tetrahedral and octahedral sites respectively. The range of values of $\tilde{u}$ determines the ground state magnetic structure the following way: $\tilde{u} \leq \frac{8}{9}$ implies the collinear *Néel* configuration where spins at a given sub-lattice are all aligned and are anti-aligned with spin at another sub-lattice, is the ground state. A stable ferrimagnetic spiral configuration becomes ground state if $\frac{8}{9} < \tilde{u} < 1.298$. For $\tilde{u} > 1.298$, the ferrimagnetic spiral is unstable. The neutron scattering data for $CoCr_2O_4$[82] when fitted to the LKDM model, produced $\tilde{u} \sim 2$ which implies that the ground state structure is an unstable spiral. Very recent neutron diffraction experiments by Tomiyasu *et al*[124] explained this anomaly by suggesting that the magnetic structure below the ferrimagnetic transition temperature is a mixture of a ferrimagnetic long range order and a spiral component, which exhibits only short-range order even in the lowest temperature phase. They also found that the ferromagnetic domains behave as re-entrant spin glass. They related the emergence of spiral short-range order, local instability and re-entrant spin glass behavior the following way: since the ferrimagnetic spiral long-range configuration is locally unstable, the spiral component exhibits short-range order. The freezing and the fluctuation of the spin-spiral component brings about the re-entrant spin glass behavior of the ferrimagnetic domain. In addition, they proposed the concept of weak magnetic geometrical frustration (weak MGF) and classified the origin of the local instability into usual MGF and weak MGF. They proposed that the weak MGF causes the spiral short range order below a characteristic temperature. Thus $CoCr_2O_4$ stands as a prototype spinel chromite to apply the concepts discuss in the previous sub-sections to understand the fundamental physics governing the physical properties of oxide spinels with two magnetic cations. Recent Infra-red spectroscopic result [94][81] predicted a coupling between magnetic and lattice degrees of freedom in $CoCr_2O_4$, thus enhancing its importance for applications of concepts and testing of models.

The discovery of multiferrocity and the observation of complex magnetic structure in $CoCr_2O_4$ naturally propelled the researchers to investigate the effects of substituting one of the magnetic atoms by a new one and thus widen the scope of its functionality. From the point of view of a broader understanding of the structure-property relationships in this class of materials, such studies are necessary. Experimental results on substituted $CoCr_2O_4$, where Cr is replaced by Mn and Fe have started to come only recently. The results are quite encouraging. Magnetic measurements on 10% and 15% Fe substituted $CoCr_2O_4$ reported a magnetisation reversal and a sizable exchange bias around a critical temperature, accompanied by non-monotonic changes in the local moments[89, 88]. Magnetic and specific heat measurements for upto 50% Fe substitution in $CoCr_2O_4$[142] observed a magnetostriction and a possible suppression of the conical spin structure giving way to a collinear magnetic structure. Substitution of Cr by Mn in $CoCr_2O_4$ led to an anomalous behavior in the structural parameters and in the magnetization[143]. The observations indicated that these anomalous behavior in the physical properties emerge as a result of complicated natures of the magnetic interactions arising out of unconventional site-occupancies with the changes in the composition. The Fe and Mn substituted $CoCr_2O_4$, thus are in need of computations and subsequent in depth analysis of the interplay between various factors like site occupancies, crystal fields and magnetic interactions as a function of compositions and the impacts on the observed physical properties.

1.3 First-principles electronic structure calculations towards exploring materials properties

The discussions in the previous subsections clearly demonstrate that the fundamental physics associated with the spinel oxides could be quite fascinating, yet, tricky to deal within simplistic theoretical frameworks. The many body effects like the strong electron-electron correlations are integral to these systems. In order to gain knowledge about the microscopic mechanism governing the properties in a material, *ab initio* calculations of its electronic structure is necessary. This implies that one has to obtain the solution of schrödinger equation for the many body electron system, which is simply intractable for a solid. The situation can be salvaged by appropriate approximations. The Density Functional Theory (DFT)[45][56] which projects the many body interacting system onto a non-interacting single particle one; where the many body interactions are taken care of in an average way through a single term, has made the required breakthrough to arrive at parameter-free, "First principles" methods so that robust and accurate results on materials properties can be obtained. Integration of DFT based first-principles methods with advanced softwares made tackling of complex problems accurately within reasonable time period. Over the year, applications of these methods in calculating properties of magnetic materials with complex spin structure, [59, 98], dynamical properties of the materials[100, 7] and simultaneous comparison of these results with experimental observations confirmed the accuracy of these methods. These sophisticated tools successfully dealt with the problem of sub-lattice disorder like the cation disorder in spinels also[128]. Over the years these methods have found wide acceptability due to their capabilities in not only interpreting experimental results but also for predicting properties of new materials where experimental evidences are not present. Thus, the DFT based first-principles methods are the essential tool for fundamental understanding of materials that I have planned to investigate during my doctoral research.

1.4 Outline of the thesis

In this dissertation, we, therefore, have extensively investigated the effects of compositions and the degree of cation disorder on the structural, magnetic and vibrational properties of Fe and Mn substituted $CoCr_2O_4$ with the focus being on gaining fundamental insights into the inter-relations of these properties and how the composition and cation distribution over different sites play a role in understanding them. We have used Density Functional Theory based electronic structure methods, along with thermodynamical models, wherever necessary, for our calculations. The analysis of the results are done with the help of the computed electronic structures and the elements from crystal field theory. Apart from exploring the fundamental physics in these systems, we have provided generalized methods for dealing with cation disorder for systems having more than two elements being affected by disorder, and for quantification of spin-phonon coupling for systems having more than one magnetic atom.

Chapter 1 introduces the reader with magnetic spinels and their various aspects. This chapter contains brief descriptions about magnetic and geometric frustrations, crystal field effects, Jahn-Teller distortions, magnetic exchange interactions and cation disorder, in the context of magnetic spinel compounds. Suitable examples are provided for easy references.

Chapter 2 contains a description of the theoretical background on the computational techniques used. The chapter starts with a brief description of the Density Functional Theory (DFT) formalism, a robust and efficient tool to solve many-body condensed matter systems in a computationally tractable way. Since electron-electron correlation is prevalent in oxides, a description of it is necessary for the systems under investigation in this work. The DFT is unable to do justice to this as exchange and correlation effects are treated in an average way in the formalism. However, necessary corrections towards electron-electron correlation is taken care of by the DFT+U formalism. A brief description of the DFT+U formalism, therefore, follows. In this work Plane-wave, Pseudo potential implementation of the DFT+U is used for all calculations. Reliable and robust pseudo potentials constructed through Projector Augmented Wave (PAW) prescription have been used, which increases the accuracy of the results. The details of these implementations are described in the rest of this chapter.

In **Chapter3**, we perform a systematic investigations into the structural and magnetic properties of the three spinel compounds $CoCr_2O_4$, $CoMn_2O_4$ and $CoFe_2O_4$. This has not been done before. Our motivation was to first understand, in somewhat detail, the similarities and differences in the structural and magnetic properties among these, with the help of the elements in crystal field theory and the calculated electronic structures. We get significant insights into the emergence of the properties as one of the magnetic element changes, by quantifying the relative strength of the crystal field and the magnetic exchange field through an analysis of their electronic structures. We find that the electron-electron correlations are very significant in these materials. Without it's incorporation, the correct ground state crystal structures can not be obtained. The electron-electron correlations bring in local structural distortions at the octahedral sites for all three and drives the $CoMn_2O_4$ system to a tetragonal ground state. This correlation is also responsible for the electronic properties such as the electronic band gaps and their variations across the compound series. We find that the electronic structures too change significantly with changes in the magnetic cation at the octahedral site. This, in turn, is found to affect the inter-atomic magnetic exchange interactions considerably and is responsible for very different spin structures of these compounds. Although the knowledges about the properties of these compounds were already available, but this work attempts at a structured understanding of the trends in the physical properties by proper quantification of physical properties and by providing necessary explanations from the trends in the structural parameters and the electronic structures. The importance of the results of this chapter is in providing necessary input to help understand the properties of the systems when one magnetic cation is systematically substituted with others.

In **Chapter 4**, we carry out investigations into the thermodynamics of cation disorder and it's influences on electronic structure, structural properties and magnetic properties in Mn substituted $CoCr_2O_4$ system, $Co\left(Cr_{1-x}Mn_x\right)_2O_4$, for x between 0 and 1. In this work, we generalize a thermodynamic model for computations of the degree of cation disorder, the "inversion parameter", for AB_2O_4 spinels to the case of $A(B_{1-x}C_x)_2O_4$ spinels. We use this generalized thermodynamic model, in conjunction with the DFT, to compute the "inversion parameter" for a given x and at a particular temperature. This quantitative evaluation of the dependence of "inversion parameter" on compositions is used to explain the experimentally observed non-regular behavior in the variations of the magnetization with the composition. The work in this chapter explores the inter-relations between the degree of cation disorder, the crystal fields associated with different atoms and their charge states, the structural and magnetic properties. The results demonstrate that the non-regular behavior of the magnetization and the structural properties can be traced back to the features in the variations in the electronic structures as a function of composition and the degree of cation disorder. The formalism and subsequent method of analysis presented in the chapter has an appeal that goes beyond the system discussed in this chapter. It has provided useful means to compute the thermodynamics of cation disorder in any $A\left(B_{1-x}C_x\right)_2O_4$ magnetic spinel and perform subsequent analysis to understand the fundamental physics of such systems.

In **chapter 5**, we use the formulations of chapter 4 to investigate the interplay of composition, degree of cation disorder, structural and magnetic properties and analyze them from trends in the electronic structures in Fe substituted $CoCr_2O_4$. A major focus in this chapter is on the evolution of the magnetic exchange interactions with increase in the concentration of Fe. This has more importance than the Mn substituted case as Fe substitution gradually leads the system from a non-collinear spin structure to a collinear one, and thus pinpointing the exact roles of composition and cation disorder are important. In this case, we find that the system always has a tendency towards "inversion" that is for moderate concentrations of Fe, the tetrahedral sub-lattice are shared by Co and Fe, while for high Fe concentration (more than 50%), the system tends to order in a "complete inverted" structure. We find that such distributions of cations over sub-lattices have serious consequences for magnetic interactions. While zero cation disorder leads to competing octahedral-tetrahedral and octahedral-octahedral magnetic exchange interactions, significant cation disorder leads to a stronger tetrahedral-octahedral magnetic exchange leading to a collinear spin structure. The structural parameters, the local structural distortions, and consequently the electronic structures and the magnetization, are found out to be intricately related to the degree of cation disorder for the Fe substituted $CoCr_2O_4$. Our elaborate addressing of these not only bring in good agreement between theory and experiment, but also provide the microscopic picture necessary to understand the physics in this system.

In **Chapter 6**, we address the effects of substitution and cation disorder on the vibrational properties for pristine as well as Fe and Mn substituted $CoCr_2O_4$. The motivation in this work is to understand the effects of cation disorder on the vibrational properties of the system. We perform systematic computations of the phonon dispersion and the vibrational densities of states by changing the compositions and the degree of cation disorder. We find that for both pristine and substituted systems, the vibrational properties depend significantly on each of these factors leading us to make a picture of the dependences between the sub-lattices occupancy and the vibrational properties. We also attempted at providing a quantitative estimate of the strength of the spin-phonon coupling by generalizing the model for spinels with single magnetic atom [61]. However, due to prohibitively large computational requirements, we were able to apply this model to only $CoCr_2O_4$. The results presented in this chapter qualitatively agree with the experimental observations from Infra-red spectroscopy. The contents of this chapter, thus, are extremely important in both qualitative understanding of the nuances of the vibrational properties of the systems studied.

Chapter 7 concludes with a summary of the main results of the thesis. The importance of these results along with the possible extensions are discussed thereafter.

Chapter 2

Methodology

2.1 Introduction

Calculations of the electronic structure of a solid system so that a microscopic picture of the prevailing interactions can evolve, requires solution of the stationary schrödinger equation. However, this becomes an impossible task as the number of atoms in the solid is of the order of 10^{23}. The conventional wave function based methods like the Hartree-Fock method, thus, can only be applied in cases of atoms or small molecules. Density functional theory (DFT), proposed in the 1960s, circumvented this difficulty in an efficient way and has become the backbone of the state-of-art electronic structure methods since then. In spite of its remarkable success for description of ground-state properties of large material classes starting from elemental solids to systems as complex as heterostructures, it has severe limitations in the descriptions of systems in which electron-electron correlation is very strong, for example, oxides. A notable failure of DFT is in the case of NiO, which predicts a near metallic ground state as the DFT computed band gap is less than 1 eV when the NiO ground state is insulating with a band gap of 4-4.3 eV[21, 85]. This problem with the DFT is addressed by incorporating the effects of on-site coulomb repulsion described in Hubbard model[47], thus introducing a correction term in DFT computed total energies so that the conduction and valence bands are separated by a gap of the order of energy that represents the on-site coulomb repulsion. The method is known as DFT+U method. This method has been used for the calculations presented in this thesis. In the next few-sections we briefly describe DFT, and DFT+U formalisms along with their implementations used throughout.

2.2 The many-body problem in solids

A solid is considered as a many body interacting system consisting of N nuclei and n electrons. The Hamiltonian of the system describes the motion of each individual electron and nucleus for every atoms, and takes the following form:

$$\mathscr{H} = -\frac{\hbar^2}{2}\sum_{I}^{N}\frac{\nabla_I^2}{2M_I} - \frac{\hbar^2}{2}\sum_{i}^{n}\frac{\nabla_i^2}{2m_i} + \frac{1}{2}\sum_{I\neq J}^{N}\frac{Z_I Z_J e^2}{\mid R_I - R_J\mid} + \frac{1}{2}\sum_{i\neq j}^{n}\frac{e^2}{\mid r_i - r_j\mid} - \frac{1}{2}\sum_{i}^{n}\sum_{I}^{N}\frac{Z_I e^2}{\mid R_I - r_i\mid} \tag{2.1}$$

where first and second term are the kinetic energies of nuclei and electrons. The 3^{rd}, 4^{th} and 5^{th} terms represent the coulomb interactions between the nuclei, the electrons and between electron and nucleus respectively. M_I, R_I are the mass and position of I^{th} nucleus and m_i, r_i are mass and positions of i^{th} electron. Z_I denotes the atomic number, of I^{th} atom.

We have to solve the following schrödinger equation in order to compute the electronic structure of the many body system

$$\mathscr{H}\Psi(r_1, r_2, ...r_i..r_n, R_1, R_2, ...R_I..R_N) = \mathscr{E}\Psi(r_1, r_2, ...r_i..r_n, R_1, R_2, ...R_I..R_N) \tag{2.2}$$

Ψ is the many body wavefunction and contains all the information of all electrons and nuclei. $\mathscr{E}$ is the Total energy of the system.

Since the mass of electron is much smaller compared to mass of nuclei ($m_e << M_I$), the velocity of electron is $\sim 10^8$ cm/s, where as the ion velocity is of of the order of $\sim 10^5$ cm/s. Due to such differences in order of magnitude of their velocities, the time scales associated with motions of electrons and nuclei are substantially different. Thus the electronic degrees of freedom can be decoupled from nuclear degrees of freedom. Thus, the ions can be considered in rest and only electronic motion can be considered. This approximation is known as Adiabatic approximation[14]. The total wavefunction of the system can now be written as product of electronic and ionic wavefunctions ($\Psi = \Psi_e(r,R)\Psi_I(R)$). This leads to two separate equations associated with electronic and ionic degrees of freedom.

$$H_e\psi_e = E_e\psi_e \tag{2.3}$$

and

$$\left(-\frac{\hbar^2}{2}\sum_{I}^{N}\frac{\nabla_I^2}{2M_I}+\frac{1}{2}\sum_{I\neq J}^{N}\frac{Z_IZ_Je^2}{\mid R_I-R_J\mid}+E_e\right)\Psi_I(R)=\mathscr{E}\Psi_I(R) \tag{2.4}$$

The electronic Hamiltonian (H_e) is given by,

$$H_e=-\frac{\hbar^2}{2}\sum_{i}^{n}\frac{\nabla_i^2}{2m_i}+\frac{1}{2}\sum_{i\neq j}^{n}\frac{e^2}{\mid r_i-r_j\mid}-\frac{1}{2}\sum_{i}^{n}\sum_{I}^{N}\frac{Z_Ie^2}{\mid R_I-r_i\mid} \tag{2.5}$$

$$=T+V_{int}+V_{ext}$$

E_e represent the electronic energy levels. T is the kinetic energy, V_{int} is the coulomb energy due to electron-electron interaction and V_{ext} represents the electron-nucleus interaction.

2.3 Density functional theory

By applying adiabatic approximation, we can separate the nuclear motion and electron motion and we can treat electron and ion dynamics as nearly independent. But the complicacy of tackling a many body system is hardly reduced as one has to still deal with a many electron system. The DFT immensely simplies the problem by constructing the ground state properties as functionals of single particle electronic charge density.

DFT[45] is based upon two major theorems:

Theorem I: For any system of interacting particles in an external potential $V_{ext}(r)$, the potential $V_{ext}(r)$ is determined uniquely, except for a constant, by the ground state particle density $n_0(r)$[74].

Theorem II:A universal functional for the energy $E[n]$ in terms of $n(r)$ can be defined, which is valid for any external potential $v_{ext}(r)$. The exact ground state energy of the system is the global minimum value of this functional, and the density that minimizes the functional is the exact ground state density $n_0(r)$[74] .

Although these two theorems provide a tractable way to calculate the ground state energy, it cannot be put into a formal procedure because of the the unknown functional $E[n]$. Kohn and Sham salvaged this procedural problem by replacing the many body system with an auxiliary non-interacting system that can be easily solved[56]. Kohn-sham ansatz assumed that the ground state density $n_0(r)$ of interacting system as the ground state density of the non-interacting system in an effective potential V_{eff}. This procedure along with variational principle leads to schrödinger-like equations

$$\left(\frac{1}{2}\nabla_i^2 + V_{eff}\right)\phi_i = \varepsilon_i\phi_i \tag{2.6}$$

The $\{\varepsilon_i\}$,$\{\phi_i\}$ are the single particle eigen values and eigen function of the non-interacting Kohn-Sham system. The single-particle density of the system now is

$$n(r) = \sum_{i=1}^{N} \mid \phi_i \mid^2 \tag{2.7}$$

with

$$V_{eff} = V_{ext}(r) + -\frac{1}{2}\int \frac{n(r)n(r')}{\mid r-r' \mid} drdr' + V_{xc} \tag{2.8}$$

where first term is the external potential (that is electron-nucleus interaction potential), second term is the Hartree term (electron-electron interaction) and the last term is the exchange-correlation potential. The exchange-correlation potential (V_{xc}) includes the many-body effects associated with the kinetic and potential energy terms.

The ground-state energy functional for the many body system, within the Kohn-Sham scheme, is given by

$$E_{KS} = -\frac{1}{2}\sum_{i=1}^{N}\langle\phi_i|\frac{\nabla_i^2}{2}|\phi_i\rangle + \int drV_{ext}(r)n(r) + \int drdr'\frac{n(r)n(r')}{\mid r-r' \mid} + \int drV_{xc}(r)n(r) + E_{II} \tag{2.9}$$

where E_{II} is the interaction between the nuclei. Equation 2.6-2.8 can be solved self-consistently and the ground state energy can be calculated from equation 2.9 with the resultant density. Although the above formulation is for non-spin polarized systems, it can be easily extended to include spin polarization by introducing two spin-densities $n_{\uparrow}(r)$ and $n_{\downarrow}(r)$ with an additional requirement that $n_{\uparrow}(r) + n_{\downarrow}(r) = N$, total number of electrons.

Now, to solve the many body problem by using Kohn-Sham formalism, there is a difficulty to calculate the V_{xc} in equation 2.8, as the exact functional is not known for real situations. The key to solve this problem is that the functional for homogeneous electron gas is known. The most widely used approximation, the local density approximation (LDA), to the exchange correlation potential, assumes that the exchange-correlation energy E_{xc}, related to V_{xc} as $V_{xc} = \frac{\delta E_{xc}[n]}{\delta n}$, can be approximated to be that obtained from the exchange-correlation enery density $\varepsilon_{xc}^{homo}(n(r))$ in a homogeneous electron gas the following way,

$$E_{xc}^{LDA} = \int drn(r)\varepsilon_{xc}^{homo}(n(r)) \tag{2.10}$$

Generalized Gradient Approximation (GGA), a correction over the LDA, includes local gradients of density as well into the functional and is given by

$$E_{xc}^{GGA} = \int drn(r)\varepsilon_{xc}^{GGA}(n(r), \nabla n(r)) \tag{2.11}$$

There are several different forms of ε_{xc}^{GGA} which have provided wonderful results [144], [4], [138], [92]. Several other approximations to exchange and correlations have also evolved over the years.[43]

2.4 Beyond DFT to treat correlated electron: DFT+U formalism

As is mentioned in section 2.1, one of the well documented failures of DFT is in treating electrons that are strongly correlated. When the electrons are strongly localized their motion becomes correlated and their wave function assumes a many-body character. Describing such systems within DFT becomes problematic due to the expression of the electron-electron interaction as a functional of charge density and to the use of an effective single-particle representation of this quantity. The failure of the standard LDA or GGA exchange-correlation functional for correlated electron systems can be traced back to their tendencies to over-delocalise the valence electrons as both the exchange and correlation are treated together on equal footing.

One of the simplest models to take into account the physics of correlated materials, is the Hubbard model[47]. The real-space second quantisation formalism is best suited to describe systems with electrons localised on atomic orbitals. The simplest one-band Hubbard Hamiltonian can be written as

$$\hat{H}_{Hub} = -t \sum_{<ij>,\sigma} \hat{a}_{i\sigma}^{\dagger}\hat{a}_{j\sigma} + U\sum_{i}\hat{n}_{i\uparrow}\hat{n}_{i\downarrow} \tag{2.12}$$

$< i, j >$ denotes nearest neighbor atomic sites, $a_{i\sigma}^{\dagger}$, $a_{i\sigma}$ and $n_{i\sigma}$ are electronic creation, annihilation and number operators for electrons of spin σ on site i. For localised electrons, their motion is described by hopping from one atomic site to its neighbors whose amplitude is proportional to the band width. The first term of Equation 2.12 represents this process.

Due to strong localisation the relevant coulomb repulsion is the one for electrons on the same atomic site only. The second term of equation 2.12 represents this and the strength of the coulomb repulsion is denoted by the parameter U, known as “Hubbard”. The balance between t and U is the deciding factor for the electronic ground state of a system. DFT can describe the system where the single-particle terms of the energy dominate ($t >> U$) but fails for the cases where electrons cannot hop around due to insufficient kinetic energy to overcome the repulsion from other electrons on neighboring sites ($t << U$).

The DFT+U is the simplest corrective approach that improves the accuracy of DFT functionals in describing the ground states of correlated systems. The idea is to use the Hubbard model to describe the strongly correlated electrons (typically, localized d or f orbitals) while the rest of the valence electrons are treated within standard DFT. The energy functional, within this approximation, can be expressed as

$$E_{DFT+U} = E_{DFT} + E_{Hub} - E_{dc} \tag{2.13}$$

Here E_{Hub} is the term that contains electron-electron interactions modeled by the Hubbard Hamiltonian, and is given by

$$E_{Hub} = \frac{U}{2}\sum_{i\sigma} n_{i,\sigma}n_{i,-\sigma} \tag{2.14}$$

E_{dc}, known as the double-counting term, is to be subtracted as E_{DFT} contains a part of the interaction energy expressed in E_{Hub}. The form of E_{dc} is

$$E_{dc} = \frac{U}{2}\sum_{\sigma} N_{\sigma}(N_{-\sigma} - 1) \tag{2.15}$$

where N_{σ} is the number of localized electrons with a given projection of spin σ, and are eigenvalues of the number operators. A particularly simple and useful form of the DFT+U total energy expression is proposed by Dudarav et al [31] which can be written as

$$E_{DFT+U} = E_{DFT}[n(\vec{r})] + \frac{(U-J)}{2}\sum_{l,j,\sigma} \rho^{\sigma}_{jl}\rho^{\sigma}_{jl} \tag{2.16}$$

here ρ^{σ}_{jl} is the density matrix of localised electrons. For an individual atom this density matrix is diagonal in the orbital representation and its eigenvalue are given by $n_{m\sigma}$ where m

are the localised orbitals. U and J are the spherically averaged screened coulomb interactions. While U corresponds to Hubbard U, J is known as the "Hunds's coupling parameter". We have used this particular DFT+U formulation in all our calculations.

Different choices of the basis sets to express Kohn-Sham orbitals, the solutions of Equation 2.6 led to the construction of different electronic structure method. One of the easily tractable methods is the plane wave Pseudopotential method. In this thesis, all calculations are done with a particular implementation of this method which is known as Projector Augmented Wave (PAW) method. In the next two sections we briefly discuss the ideas behind the PseudoPotential method and the PAW formalism.

2.5 The Pseudopotential method

In the free electron model, the eigen states of a solid are represented by plane waves. Even after introduction of a crystal potential, as per Bloch's theorem, the eigen states are periodic modulations of the plane waves. Thus, plane waves are the natural basis set to be chosen to describe electronic states in a solid. Also, they are computationally inexpensive. However, a serious disadvantage pops up when the wavefunction in the core region are described in terms of plane waves. The orthogonality of the valence and core region forces the valence wavefunctions in the core region to be rapidly oscillating. The computational cost increases in such circumstances as very large number of plane waves are required to describe such wave functions.

The Pseudopotential method provides a solution to this problem. In this method, the strong core potential of an atom is replaced by a pseudopotential. It is done in such a way that the ground state wavefunction corresponding to the Pseudo-Hamiltonian mimics all electron valence wavefunctions outside a cut-off radius. The construction of the pseudopotentials removes wiggles in the wave functions in the core region, resulting in a continuation of smooth valence wavefunction there. Thus, the pseudo-wavefunctions can be represented by a reasonable number of plane waves, making the method computationally tractable. In its earlier days of development, the pseudopotentials were constructed with the constraint of "norm conservation"[114, 125]. In the 1990's vanderbilt and co-workers made this formalism more tractable by doing away with the constraint of norm conservation and allowing the pseudopotential to be as soft as possible inside a cut-off radius. This construction, known as ultrasoft pseudopotential [130] have enhanced the applicability of the formalism to a larger class of systems.

2.5.1 Projector Augmented Wave (PAW) method

A major drawback of the pseudopotential method is that all information in the core region is lost and thus affects the calculations of hyper-fine parameters and electric field gradients. The projector Augmented Wave (PAW) [11], introduced by Blöchl, an extension of both Augmented Plane Wave (APW) method[70, 109] and pseudopotential method, adresses the difficulties associated with the conventional pseudopotential methods. In this method the wavefunction is divided into two parts: a partial wave expansion within an atom centered sphere and an envelop function outside. The two parts are then smoothly matched at the edge of the sphere. A brief description of the formalism is as follows.

Let $\hat{T}$ be an linear transformation operator which maps smooth auxiliary pseudo wavefunction $|\tilde{\psi}\rangle$ to physical all-electron wavefunction $|\psi\rangle$

$$|\psi_n\rangle = \hat{T}\,|\tilde{\psi}_n\rangle \tag{2.17}$$

where n is the quantum level consisting of band, spin and $\vec{k}$-indices. Since the true wave function matches with smooth wavefunction at a certain minimum distance from core, $\hat{T}$ should only modify the wave function close to the nuclei. That means the transformation is unitary beyond the augmentation cut-off and a sum of atom-centered contributions inside

$$\hat{T} = I + \sum_a \hat{T}^a \tag{2.18}$$

Where $\hat{T}^a$ are transformation operators associated with atom centers a and have no effect out side cutoff radius r_c^a. The cutoff radius r_c^a should be chosen such that there is no overlap of the augmentation spheres.

Now both the all-electron wavefunction $|\psi_n\rangle$ and the auxiliary smooth function $|\tilde{\psi}_n\rangle$ can be expanded in terms of partial waves, within the augmentation region,

$$|\psi_n\rangle = \sum_i C_{ni}\,|\phi_i\rangle \tag{2.19}$$

and

$$|\tilde{\psi}_n\rangle = \sum_i C_{ni}\,|\tilde{\phi}_i\rangle \tag{2.20}$$

with identical coefficient C_{ni} in both these expression. Subtracting equation 2.20 from equation 2.19 and re arranging we get

$$|\psi_n\rangle = |\tilde{\psi}_n\rangle - \sum_i C_{ni} |\tilde{\phi}_i\rangle + \sum_i C_{ni} |\phi_i\rangle \tag{2.21}$$

For transformation operator $\hat{T}$ to be linear, C_{ni} must be scalar product and

$$C_{ni} = \langle \tilde{p}_i | \tilde{\psi}_n \rangle \tag{2.22}$$

where $\langle \tilde{p}_i|$ is a projector operator. The Transformation operator $\hat{T}$ is found to be

$$\hat{T} = I + \sum_i (|\phi_i\rangle - |\tilde{\phi}_i\rangle) \langle \tilde{p}_i| \tag{2.23}$$

Due to this transformation the kohn-sham equation becomes

$$H |\psi_n\rangle = H\hat{T} |\tilde{\psi}_n\rangle = \varepsilon_n \hat{T} |\tilde{\psi}_n\rangle$$

$$\Rightarrow \hat{T}^{\dagger} H \hat{T} |\tilde{\psi}_n\rangle = \varepsilon_n \hat{T}^{\dagger} \hat{T} |\tilde{\psi}_n\rangle \tag{2.24}$$

Therefore, by solving the modified Kohn-sham equation 2.24 we get smooth wavefunction $|\tilde{\psi}_n\rangle$ and after that we can find the true all-electron wavefunction $|\psi_n\rangle$ by using 2.17.

2.6 Summary

In this chapter we have briefly discussed the DFT and it's extension DFT+U method which addresses the localised strongly correlated electrons. The most tractable and widely used Pseudopotential-PAW implementation of the DFT is also discussed. For the magnetic oxides, DFT+U with Pseudopotential-PAW implementation is quite suitable as DFT+U provides reasonable estimates of the ground state properties of strongly correlated electron systems while the Pseudopotential-PAW implementation allows one to do computations with reasonable resources and without compromising accuracy. There are various other implementations of the DFT+U but we refrained from discussing them here as throughout the thesis we have used the Pseudopotential-PAW implementation only.

Chapter 3

Systematic investigations into the structural and magnetic properties of $CoCr_2O_4$, $CoMn_2O_4$ and $CoFe_2O_4$ [†]

3.1 Introduction

In section 1.2 we had introduced the fascinating and complex behaviors of structural, magnetic and thermal properties of $CoCr_2O_4$ when substituted with Fe or Mn. The anomalous behaviors in the physical properties in either cases depended heavily upon the concentration of the substituting elements, that is Fe or Mn. For example, a temperature depended magnetic compensation was found in $Co(Cr_{0.95}Fe_{0.05})_2O_4$ which was absent for higher Fe concentrations, as well as for pristine $CoCr_2O_4$ [142, 89, 88, 96]. Mn-substitution at the Cr site resulted in different variations of magnetisation in different composition regime[143]. These results imply that the substitution of Cr by another magnetic atom renormalizes the inter-sublattice magnetic interactions and can be directly connected to such unusual phenomena. In order to understand the basic physics of such complex behavior, one first need to have a clearer understanding of the physics involved with the end compounds $CoCr_2O_4$, $CoMn_2O_4$ and $CoFe_2O_4$. This can be achieved when these three systems, which differ only in the chemical element B occupying about 30 % of the sites, are investigated in a systematic manner and various physical properties of these materials are understood at a microscopic level, that is, from their electronic structures. Although these are results available from electronic structure calculations of $CoCr_2O_4$[34, 28] and of $CoFe_2O_4$[39, 46, 40] only, no systematic study exploring the fundamentals associated with the interplay of sub-

---

[†] Most of the contents of this chapter are published in [26]

lattice occupancy, magnetic interactions and structural properties of these materials on the basis of their electronic structures is available. In this chapter, we present the results of our systematic investigations addressing these aspects by first-principles calculations.

3.2 Computational Details

We have used DFT+U [2] method for all our calculations in order to address the electron electron strong correlation effects which is necessary for oxide systems. As mentioned in section 2.4, we have used the approach of Dudarev *et al* [31] where the effects of on-site Coulomb correlation and Hund's coupling are represented through an effective parameter $U_{eff} = U - J$, U being the strength of the Coulomb interaction and J the Hund's coupling. In our calculations, J has been kept at 1 eV as previous DFT calculations for a number of transition metal oxides showed that J remains nearly constant for the entire transition metal series [112]. The coulomb parameter U has been taken to be 3 eV for Cr, 4 eV for Mn and Fe, 5 eV for Co. The choice of U at a B site being smaller than that at A site rests upon the rationale that the screening at the six-folded coordinated B site would be more effective than the screening at the four-fold coordinate A site. The absolute values of U for different cations are chosen after careful inspection of available information from DFT calculation and experiments [93, 24, 36, 37]. The self-consistent kohn-sham equations are solved using the projector augmented wave (PAW) [11] basis set as implemented in VASP code [57]. The exchange correlation part of the Hamiltonian is treated with the PBE-GGA [91] functional. A plane wave cut off of 550 eV and a $5 \times 5 \times 5$ mesh centered at Γ point for Brillouin zone integrations have been used throughout to ensure an energy convergence of 10^{-7} eV. For structural relaxations the convergence criteria of force on each atom is set to be 10^{-4} eV/Å. In Table 3.1, we demonstrate that such cut-offs provide good convergences in physical properties. Although here we show results only for the structural parameters with respect to kinetic energy cut-off and the energy convergence criteria, convergences have been ensured with respect to k-mesh size and forces on atoms.

3.3 Results and discussions

3.3.1 Modeling of the sub-lattice occupancy and spin configuration

The spinel structure and the corresponding atomic arrangement have already been presented in Figure 1.1 and Table 1.1. Among the three compounds under consideration, the $CoCr_2O_4$ is found to be crystallising in 'Normal spinel' structures [82]. In case of $CoMn_2O_4$, although

Table 3.1 Dependence of lattice parameters on plane wave cut-offs and convergences in energy.

plane wave cut-off in eV	Energy convergence (eV)	Lattice Constant in Å								
		$CoCr_2O_4$			$CoMn_2O_4$			$CoFe_2O_4$		
		a	b	c	a	b	c	a	b	c
400	10^{-5}	8.37	8.37	8.37	9.21	8.10	8.09	8.39	8.31	8.31
400	10^{-7}	8.37	8.37	8.37	9.21	8.10	8.09	8.38	8.31	8.31
500	10^{-7}	8.37	8.37	8.37	9.39	8.17	8.17	8.46	8.40	8.40
550	10^{-7}	8.43	8.43	8.43	9.39	8.17	8.17	8.45	8.41	8.41
600	10^{-7}	8.43	8.43	8.43	9.39	8.17	8.17	8.46	8.39	8.39
550	10^{-8}	8.43	8.43	8.43	9.39	8.17	8.17	8.46	8.40	8.40

the sub-lattice occupancy conforms to that of spinel, the crystal structure is tetragonal with space group $I4_1/amd$ [15]. $CoFe_2O_4$, on the other hand, has no structural distortion, but has the sub-lattice occupancy like "Inverse spinel" [120]. The sub-lattice occupancies in $CoFe_2O_4$ is found to be crucial in determining whether the ground state is insulator or half-metal [39, 46]. Regarding the ground state magnetic structure, Neutron diffraction studies have shown that $CoCr_2O_4$ and $CoMn_2O_4$ have canted spin structures [124, 15] while $CoFe_2O_4$ has a ferrimagnetic collinear structure, with the moments at A and B sites anti-aligning, giving rise to the *Néel* configuration [120]. Mössbauer studies [54] later confirmed this.

The sub-lattice occupancy for $CoCr_2O_4$ and $CoMn_2O_4$ have been taken to be like normal spinels as have been found from experiments. For $CoFe_2O_4$, inverse spinel sub-lattice occupancy with maximum inversion has been considered. In absence of disorder at a particular sub-lattice, this configuration is found to be having the lowest energy[46]. Since modeling of the sub-lattice disorder requires either construction of a supercell in the present approach or consideration of a mean field configuration averaging procedure [40], we have considered the complete inverse spinel type sub-lattice occupancy for $CoFe_2O_4$. Since the motivation behind this work is a systematic understanding of the three systems as the chemical identity of the B atom changes, we have taken the magnetic configurations of the three systems to be collinear. Although $CoCr_2O_4$ and $CoMn_2O_4$ have non-collinear magnetic ground states, the investigations into the collinear magnetic states would provide important qualitative insights. In order to find out the relative alignments of the spins at various sub-lattices, we have taken two formula units of the unit cell and done total energy calculations on different collinear spin configurations. We found the *Néel* configuration to be energetically lowest in case of $CoCr_2O_4$ and $CoFe_2O_4$. In case of $CoMn_2O_4$, we found a magnetic configuration in which the spins at the sites of a given sub-lattice are anti-parallel, giving rise to a zero magnetic moment at each sub-lattice, lowest in energy. However, the energy of the *Néel* configuration is higher by about only 1 meV per atom. This result indicates that the actual magnetic ground state of $CoMn_2O_4$ would be frustrated. In subsequent analysis we have considered only the *Néel* configuration therefore.

3.3.2 Structural parameters

The lattice parameters obtained after full structural relaxations using DFT+U for the three compounds are given in Table 3.2. It provides the details of various bond lengths and bond angles, thus providing a close-up view of the structures around the tetrahedral A and the octahedral B sites. The lattice parameters agree well with the available experimental results. $CoCr_2O_4$ stabilises in the cubic structure with almost no local distortion at the A site as can be seen from the ideal spinel value of 109.47^0 for the $O-Co-O$ angle. There is slight local distortion at the B site; the $O-Cr-O$ bond angle is 84.55^0, deviating from the ideal value of 90^0 and the $Co-O-Cr$ bond angle is 121.53^0 in place of ideal value of 125^0. $CoMn_2O_4$, on the other hand, has a tetragonal crystal structure with $c/a = 1.16$. Subsequently various bond distances and bond angles (Figure 3.1) are significantly dispersed. One can now see substantial distortion associated with the A sites as the $O-Co-O$ bond angles are $108.14^0 \pm 4.13^0$. The octahedra too distorts considerably with elongation(contraction) of $Mn-O$ bonds along $z(xy)$ directions[Figure 3.2]. This leads to significant variations in the $O-Mn-O$ and $Mn-O-Co$ angles. The differences in the distortions in the octahedra around the B sites in $CoMn_2O_4$ in comparison to $CoCr_2O_4$ is pictorially represented in Figure 3.2. In case of $CoFe_2O_4$, our calculations produce a slight departure from the perfect cubic structure, the $c-$axis elongated by about 0.5%. This slight loss of cubic symmetry is due to different distortions of the octahedra around Co and Fe sites. It is observed that while there is slight elongations of $Co-O$ bonds along z-direction, the $Fe-O$ bonds in the same direction contract in comparison to the same bonds in the xy planes. This gives rise to the small tetragonality. The bond angles (Figure 3.1(c)) associated with the B and A sites clearly show that the distortions associated with Co atoms in the B sites. The $O-Co-O$ bond angle deviates to $88.23^0 \pm 2^0$ as opposed to $O-Fe-O$ bond angle of $90.24^0 \pm 0.07^0$ which is quite close to ideal spinel value of 90^0. Similarly, Fe_O-O-Fe_T bond angle is 124.16^0, while that of Co_O-O-Fe_T bond angle is 121.53^0, a larger deviation from ideal spinel value of 125^0.

The energy level diagrams (Figure 3.3) based upon the electronic configurations of the cations occupying the A and B sites can explain the observed trends in the structural aspects of these compounds. Figure 3.3 shows that in case of $CoCr_2O_4$, the higher lying e_g states

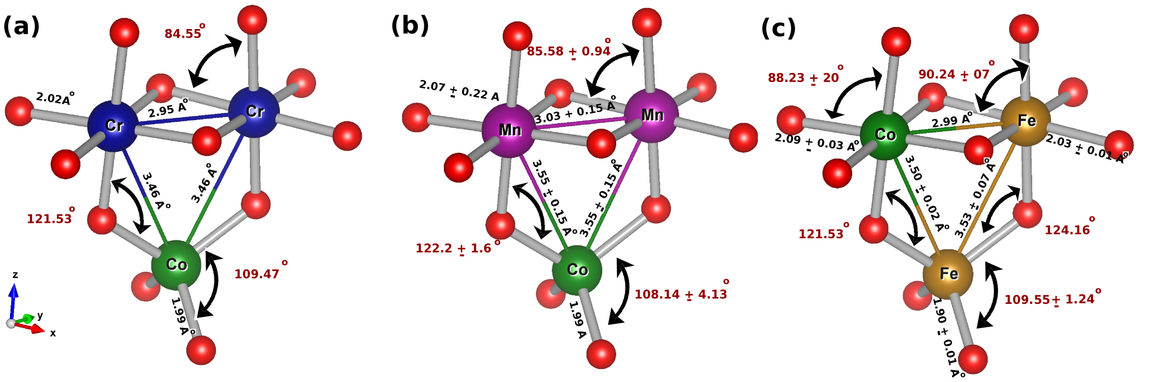

Fig. 3.1 The neighborhood around the tetrahedral A and the octahedral B sites in (a) $CoCr_2O_4$, (b)$CoMn_2O_4$ and (c)$CoFe_2O_4$ along with the bond lengths and bond angles.

Table 3.2 The lattice parameters of CoB_2O_4. a, b, c are the lattice constants. x, y, z are the Oxygen parameters.

Structural parameter	$CoCr_2O_4$	$CoMn_2O_4$	$CoFe_2O_4$
a(Å)	8.43(8.34^a)	8.17(8.1^{b,c})	8.41(8.366^d)
b(Å)	8.43(8.34^a)	8.17(8.1^{b,c})	8.41(8.366^d)
c(Å)	8.43(8.34^a)	9.39(9.13^b,9.3^c)	8.45(8.366^d)
x	0.262(0.264^a)	0.255(0.23^b)	0.255(0.256^d)
y	0.262(0.264^a)	0.255(0.23^b)	0.255(0.256^d)
z	0.262(0.264^a)	0.267(0.256^b)	0.255(0.256^d)

a: Reference [64] *b*: Reference [15] *c*: Reference [134] *d*: Reference [120]

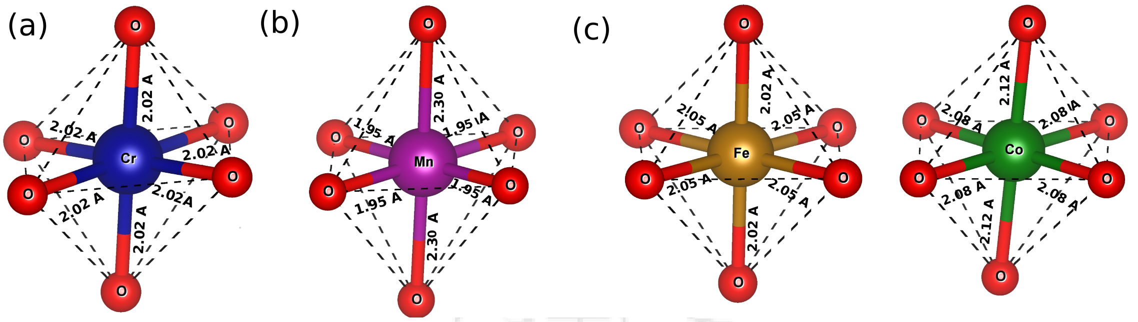

Fig. 3.2 The neighbourhood around the B site of (a)$CoCr_2O_4$,(b) $CoMn_2O_4$ and (c)$CoFe_2O_4$ providing a close up view of the distortions associated with the octahedra.

of octahedral Cr^{3+} are empty while the e_g^1 configuration of Mn^{3+} in $CoMn_2O_4$ implies degeneracy associated with this level. In order to lift the degeneracy, the symmetry of the crystal structure is lowered, giving rise to the tetragonal ground state. The largeness in the tetragonal distortion can be understood from the $\left(t_{2g}\right)^3\left(e_g^1\right)$ configuration of the Mn^{3+} ions as explained by Dunitz and Orgel [32]. In case of $CoFe_2O_4$, the degeneracy associated with the t_{2g} orbitals of the Co^{2+} ions leads to the lowering of the cubic symmetry. The small value of the distortion can once again be understood from the $\left(t_{2g}\right)^5\left(e_g\right)^2$ of the Co atom in the B site [32].

3.3.3 Electronic Structure and Magnetic moments

The configurations of d electrons at different cation sites play the most important role in determining the electronic and magnetic properties of spinel oxides. According to crystal field theory [17], the electronic configuration depends on the relative strengths of the crystal field (CF) and intra-atomic exchange field (EX). In this subsection, we attempt an understanding of the relation between the structural distortions and electronic structures in CoB_2O_4 compounds by investigating the relative strengths of crystal field splitting and exchange splitting through an analysis of the densities of states. Consequently, this would lead to the understanding of the electronic and magnetic properties of these systems.

The schematic representation of electrons in d levels in Fig. 3.3, based upon crystal field theory, shows that in a tetrahedral crystal field, the e_g levels lie lower than the t_{2g} levels due to direct electrostatic repulsion between the t_{2g} orbitals and the surrounding anion orbitals, while in an octahedral crystal field, the order is reversed as the e_g orbitals are repelled in this case. Upon tetragonal distortion, the e_g levels associated with the B sites further split into two levels with $d_{x^2-y^2}$ orbital at a energy higher than d_{z^2}, and the t_{2g} level splits into a

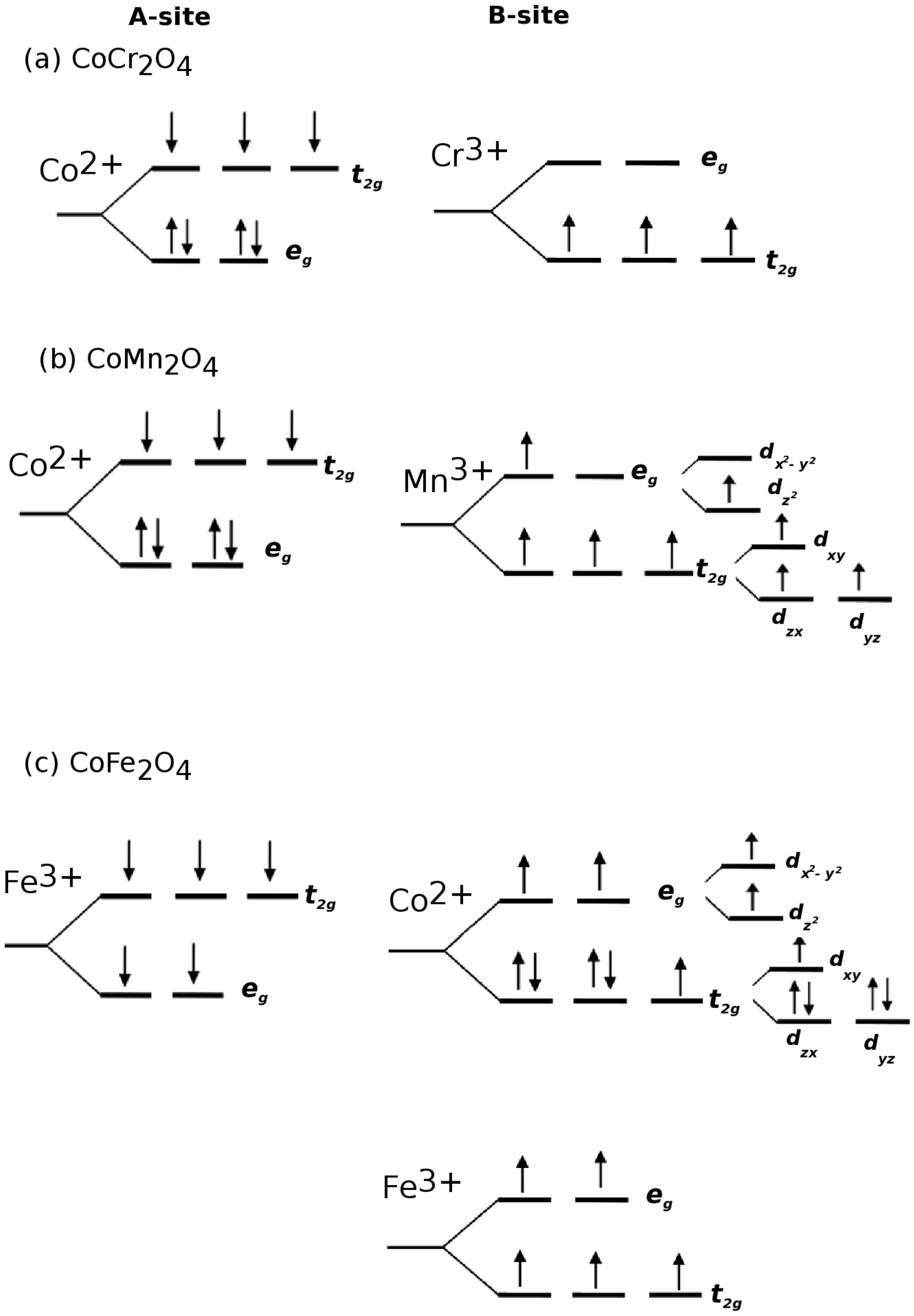

Fig. 3.3 Electronic configurations for cations occupying A and B sites in CoB_2O_4 compounds

Table 3.3 Exchange Splitting (Δ_{EX}) and crystal field splitting (Δ_{CF}) results for the three compounds.

System	ion	A site				ion	B site			
		$\Delta_{EX}^{e_g}$	$\Delta_{EX}^{t_{2g}}$	$\Delta_{CF}^{\downarrow}$	$\Delta_{CF}^{\uparrow}$		$\Delta_{EX}^{e_g}$	$\Delta_{EX}^{t_{2g}}$	$\Delta_{CF}^{\downarrow}$	$\Delta_{CF}^{\uparrow}$
$CoCr_2O_4$	Co^{2+}	1.6	2.9	0.0	1.3	Cr^{3+}	1.3	3.2	1.3	3.3
$CoMn_2O_4$	Co^{2+}	1.6	2.5	0.5	1.3	Mn^{3+}	1.8	3.7	0.3	2.2
$CoFe_2O_4$	Fe^{3+}	3.3	3.1	1.0	0.8	Fe^{3+}	3.5	3.7	1.7	1.9
						Co^{2+}	3.1	2.4	1.9	1.2

higher d_{xy} level and a lower doubly degenerate $d_{zy}(d_{zx})$ level when $c/a > 1$. The spacings of these energy levels depend on the strengths of the crystal fields and the exchange fields.

In Table 3.3 we present results for crystal field splitting (Δ_{CF}) and the exchange splitting (Δ_{EX}) for the three compounds. These results are obtained without incorporation of correlations that is by setting $U_{eff} = 0$. A comparison of results for the three show that the stronger exchange splitting associated with the t_{2g} states, in comparison to crystal field splitting, is a common feature for the compounds. This should lead to high spin states for both magnetic cations. The results suggest that for all three materials, the five-fold $3d$ crystal degeneracy is barely broken for the down spin(↓)channel of A site. Therefore, irrespective of the chemical identity of the species at A site, this spin band is nearly full. For $CoCr_2O_4$ and $CoMn_2O_4$, the other $3d$ electrons mostly occupy the exchange split ($\Delta_{EX}^{e_g} = 1.6$ eV)e_g up spin (↑) channel. In case of $CoFe_2O_4$, the exchange splitting of e_g levels is double that of the other two compounds. This is due to the fact that in $CoFe_2O_4$, the Fe^{3+} occupies the A sites having two electrons less than Co^{2+} which occupies A sites in the other two compounds, making the $e_g^{\uparrow}$ states nearly empty. The $t_{2g}^{\uparrow}$ states in all cases are energetically higher and thus remain mostly unoccupied (Figure 3.4), the exchange splitting associated with t_{2g} states ($\Delta_{EX}^{t_{2g}}$) being nearly constant, therefore.

The large exchange splitting of the t_{2g} states at the B site for $CoCr_2O_4$ and $CoMn_2O_4$ indicate that one of the spin bands is nearly full and the other nearly empty. This indeed is the case with the $t_{2g}^{\uparrow}$ bands nearly full in both cases(Figure 3.4). For $CoFe_2O_4$, there are two different values of $\Delta_{EX}^{t_{2g}}$ corresponding to Fe^{3+} and Co^{2+}. While the exchange splitting for Fe is nearly same as that of Cr and Mn, it is smaller for Co. The reason is that Co^{2+} has two more electrons than Cr(Mn,Fe) and hence part of the down (↓)spin channel is also occupied. The exchange splitting of e_g states at the B site for $CoCr_2O_4$ and $CoMn_2O_4$ are much smaller as the e_g band is nearly empty for both spins. One extra electron in the e_g band of $CoMn_2O_4$ in comparison to $CoCr_2O_4$ increases $\Delta_{EX}^{e_g}$ for the former. In case of $CoFe_2O_4$, $\Delta_{EX}^{e_g}$ are comparable for both Co and Fe at the B site. This is expected as both Co^{2+} and Fe^{3+} have one spin channel completely full and the other completely empty. The extra electron in Mn^{3+} e_g band (as compared to Cr^{3+}) explains the reason behind smaller values of crystal field splitting(for both bands) in $CoMn_2O_4$ than in $CoCr_2O_4$. In $CoFe_2O_4$, $\Delta_{CF}^{\downarrow}$ for both Co^{2+} and Fe^{3+} are the largest while $\Delta_{CF}^{\uparrow}$ are smaller than that for Cr^{3+} and Mn^{3+} in the other two compounds. The smaller values of $\Delta_{CF}^{\uparrow}$ are due to the fact that for both cations, up(↑)bands are nearly full and therefore, the centers of $t_{2g}^{\uparrow}$ and $e_g^{\uparrow}$ bands lie much closer than those of Cr^{3+} and Mn^{3+} in the other two compounds. The largest crystal field splittings for down(↓) bands of Co^{2+} and Fe^{3+} in $CoFe_2O_4$ are due to the facts that unlike Cr^{3+} and Mn^{3+} in other two compounds, the $t_{2g}^{\downarrow}$ are not completely empty. Thus, the separation between $t_{2g}^{\downarrow}$ and $e_g^{\downarrow}$ are larger compared to the other two. The outcome of the competition between the crystal field splitting and the exchange splitting would affect the semiconducting band gap in these materials. In case of $CoCr_2O_4$, equally strong exchange splitting and crystal field splitting at Cr site decides the gap. For the other two compounds, weaker crystal field splitting compared to the exchange splitting at B sites should result in decrease in the band gap as the B occupation changes from Cr to Mn and Fe. However, with the GGA only calculations, ground states of $CoMn_2O_4$ and $CoFe_2O_4$ are metallic. This is because of the presence of finite densities of states at the Fermi level of B site atoms (Figure 3.4). This can be correlated to the fact that without the inclusion of strong correlations, $CoMn_2O_4$ crystallizes in cubic structure, thus unable to obtain the symmetry breaking of the d orbitals and distribution of states on both sides of the Fermi level. In case of $CoFe_2O_4$,the distortion at the Co site is small and thus the local symmetry is barely broken, resulting in the localisation of states at the Fermi level. The inclusion of electron-electron correlation through GGA+U formalism produces the correct semiconducting ground states by introducing appropriate localisation of states, and the correct crystal structures by breaking the degeneracies in the e_g orbitals of Mn cations in $CoMn_2O_4$. The total and atom projected densities of states calculated with GGA+U are presented in Figure 3.5. In $CoCr_2O_4$, Co $t_{2g}^{\downarrow}$ electrons are localised around -6

Table 3.4 The magnetic moments of $A(\mu_A), B(\mu_B)$ cations and the total moment(μ_T) per formula unit in Bohr Magneton

System	A site	μ_A	B site	μ_B	μ_T
$CoCr_2O_4$	Co	-2.66	Cr	2.94	2.95
$MnCr_2O_4$	Co	-2.68	Mn	3.81	4.84
$CoFe_2O_4$	Fe_A	-3.98	Fe_B	4.10	2.98
			Co_B	2.66	

eV and $e_g^{\downarrow}$ states are localised around -2 eV. In the down spin (↓) band, it is the e_g states that primarily hybridise with the oxygen p states. The $t_{2g}^{\uparrow}$ Co states are unoccupied and centered around 2-4 eV, while the 2 e_g electrons are localised between -1 eV and -2 eV in the up(↑) spin channel. This gives rise to a magnetic moment of about 3 μ_B at the Co site (Table 3.4). At the Cr site, the incorporation of strong correlation does not have a very significant effect on the t_{2g} states, the $t_{2g}^{\uparrow}$ states are still fully occupied with the electrons localised near the Fermi level while the fully unoccupied $t_{2g}^{\downarrow}$ states are pushed towards higher energies. The t_{2g} states thus weakly hybridise with the oxygen states. The e_g band is nearly empty as it was when calculations were done without incorporating U_{eff}. This results in a magnetic moment of nearly 3μ_B for Cr atoms as well, with the sign of the moment opposite to that of Co atoms (Table 3.4).

In $CoMn_2O_4$(Figure 3.5(b)), the t_{2g} states of Co are qualitatively similar to those in $CoCr_2O_4$, except that they are shifted as a whole towards lower energy. The e_g states at Co site are more delocalised in comparison to those in $CoCr_2O_4$ leading to more hybridisation between Co $e_g^{\downarrow}$ and oxygen p states. This, however, still gives rise to a magnetic moment of about 3μ_B at Co site, like $CoCr_2O_4$. The densities of states at the Mn site (Figure 3.5(e)) is more interesting as the degeneracy of the d states are lifted due to large tetragonal distortion. According to crystal field theory, the higher energy $e_g^{\uparrow}$ states should split into d_{z^2} and $d_{x^2-y^2}$ states with d_{z^2} being unoccupied and $d_{x^2-y^2}$ participating in covalent bond formation with oxygen [135]. In Figure 3.5(e), we indeed see this happening. The half-filled $d_{z^2}^{\uparrow}$ gives rise to distinct peaks at around -6 eV and at around 1 eV. The $d_{x^2-y^2}$ states are more delocalised, having participated in hybridisations with oxygen p states. The down (↓) spin channel is nearly empty, leading to a Mn moment of nearly 4 μ_B (Table 3.4). The lifting of degeneracy has less effect on the t_{2g} states except that they are more delocalised in comparison to the case when effect of electron electron correlation was absent and the crystal structure was cubic. Overall, the extra electron in the e_g band of Mn (in comparison to Cr) gives rise to states closer to the Fermi level and thus reduces the electronic band gap in $CoMn_2O_4$ in comparison to the band gap in $CoCr_2O_4$ as expected. The calculated band gap in $CoCr_2O_4$ is 2.1 eV while that of $CoMn_2O_4$ is 0.33 eV.

In $CoFe_2O_4$, different sub-lattice occupancy due to the 'Inverted' structure introduces qualitative differences of both A and B sites densities of states (Figure 3.5(c) and (f)). The introduction of strong correlations pushes the unoccupied states in the spin up band towards higher energy (compairing with Figure 3.4(c) and (f)). The completely filled spin down band has electrons extremely localised around -6 eV to -7 eV allowing little hybridisations with the oxygen states.This leads to a moment of 4 μ_B for Fe_A atoms. At the octahedral site, there are two types of atoms, Fe_B and Co_B. We see qualitatively very different features of the states associated with these two atoms. The $e_g^{\downarrow}$ band is completely empty for either atoms. For Fe$_B$, the $t_{2g}^{\uparrow}$ band is completely full and is extremely localised around -6 eV to -7 eV. Thus, irrespective of the crystal environment, Fe states are localised in CoFe$_2$O$_4$. The Co states in the B sites are, however, delocalized, particularly in the spin up band. The distortions associated with the Co site, breaks the t_{2g} degeneracy only slightly. In the down spin band, the d_{zx}, d_{yz} states give rise to states near Fermi level(peaks close to -1 eV). There were no such states associated with the B sites in the other two compounds. The extra electrons in Co, in comparison to Cr and Mn, are responsible for these states. This, in turn, reduces the band gap, in comparison to CoMn$_2$O$_4$; the calculated band gap of CoFe$_2$O$_4$ being 1.14 eV. The $t_{2g}^{\uparrow}$ states of Co are delocalised, hybridising with the oxygen p states.The magnetic moments are, therefore about 3 μ_B and 4 μ_B for Co_B and Fe$_B$ in CoFe$_2$O$_4$ (Table 3.4).

The comparative study of the electronic structure, thus, shows that the Co states are delocalised irrespective of the crystal environment while the Fe states are extremely localised in CoB$_2$O$_4$ compounds considered. This would have important consequences on the magnetic exchange interactions and therefore the spin structures of the pristine compounds as well as in doped systems which have been investigated experimentally only recently [89, 142, 143]. In the next subsection we compute and discuss the magnetic exchange interactions of these compounds.

3.3.4 Magnetic Exchange Interactions

Table 3.5 The magnetic exchange parameters (J_{ij} in meV) and the Ferrimagnetic transition temperatures(T_c in K)of the three compounds

System	Type of AA pair	J_{AA}	Type of BB pair	J_{BB}	Type of AB pair	J_{AB}	T_c
$CoCr_2O_4$	Co-Co	-0.56	Cr-Cr	-3.01	Co-Cr	-3.26	144(97^a)
$CoMn_2O_4$	Co-Co	-0.29	Mn-Mn	-1.05(out of plane) -9.46(in plane)	Co-Mn	-3.53	153(85^b)
$CoFe_2O_4$	$Fe_B - Fe_B$	-2.06	$Co_B - Co_B$ $Fe_B - Fe_B$ $Fe_B - Co_B$	0.08 -4.77 0.84	$Fe_A - Co_B$ $Fe_A - Fe_B$	-10.43 -21.65	1079(860^c)

a: Reference [64] b: Reference [134] c: Reference [120]

To determine the magnetic exchange parameters, we have calculated total energies for four different collinear magnetic configurations: the ferrimagnetic *Néel* configuration, the ferromagnetic configuration, and two configurations with anti-parallel moments within A and B sub-lattices, respectively. The exchange parameters are then obtained by mapping the DFT+U results onto a classical Heisenberg Hamiltonian

$$E = -\sum_{i,j} J_{ij}\hat{e}_i.\hat{e}_j \tag{3.1}$$

where J_{ij} are the magnetic exchange parameters and $\hat{e}_i$ and $\hat{e}_j$ are normalised spin directions. The magnetic transition temperature T_c has been calculated from these exchange parameters employing the mean field approximation. Under this approximation, T_c for a multi-sublattice system can be obtained by solving a system of coupled equations

$$< e^z_\mu > = \frac{2}{3k_B T_c} \sum_\nu J_{\mu\nu} < e^z_\mu > \tag{3.2}$$

This can be rewritten in the form of an eigenvalue matrix problem,

$$(\Theta - T_c I)\, S = 0 \tag{3.3}$$

where $\Theta_{\mu\nu} = (2/3k_B) J_{\mu\nu}$, I is an unit matrix, and S is the vector set of $< e^z_\mu >$. The largest eigenvalue of the matrix is the value of T_c. The results for the nearest neighbour interactions are presented in Table 3.5. The higher neighbour exchange interactions are smaller by an order of magnitude and hence they are not considered for discussions. The results show that the A-A interactions are the weakest and therefore, not expected to play any significant role. This is consistent with the discussion by Kaplan [52]. In $CoCr_2O_4$, the A-B and B-B exchange interactions are comparable. In this case B site t_{2g} orbitals are half-filled. So direct B-B interactions are possible, apart from the super-exchange via oxygen atoms. Moreover, nearly empty e_g orbitals (Figure 3.5 (d)) reduces the anion shielding as partial covalency via e_g orbitals are possible. However, since the A site t_{2g} orbitals are half-filled and the B site e_g orbitals are nearly empty as seen from the densities of states, the A-B interactions ceases to be the strongest. Therefore, the A-B and B-B interactions are comparable for $CoCr_2O_4$. Due to these two interactions being comparable, the spin structure of $CoCr_2O_4$ is not collinear [139] as has been observed in the experiments. The calculation of the so called LKDM parameter [72] which characterises the magnetic structure of cubic spinels also confirmed this picture [28]. In $CoMn_2O_4$, the A site t_{2g} orbitals are half-filled while the B site e_g orbitals are less than half-filled and degenerate. This should lead to a strong antiferromagnetic A-B interaction which indeed is observed in our calculations

($J_{Co-Mn} = -3.53$ meV). As for the B-B interaction, the B site t_{2g} orbitals are half-filled and so direct B-B interactions, apart from super-exchange via oxygen is possible. However, the strength of this interaction would depend on the inter-cation distance [135]. Due to the tetragonal distortion, the in-plane Mn-Mn distances are short (~ 2.88 Å) and thus the direct interactions are extremely strong~ -9.5 meV (Table 3.5). The out-of-plane Mn-Mn distances are, on the other hand are ~ 3.11 Å. This weakens the B-B interactions and are only ~ -1.05 meV. This huge anisotropy in the exchange interactions due to the tetragonal distortion leads to a complicated non-collinear spin structure [15]. This anisotropy in the $CoMn_2O_4$ was discussed earlier [136] but was never calculated from first-principles. Our calculations provided the quantitative credence to the original idea.

In case of $CoFe_2O_4$, the overwhelmingly dominant interactions are the A-B interactions as is seen from our calculations. This explains the reason behind a collinear spin structure of this system. The reason behind this strong antiferromagnetic A-B interaction is that the A site t_{2g} orbitals and B site e_g orbitals (for both Fe and Co at B site) are half-filled. The reason behind a weak Co-Co and Co-Fe interactions at the B site is that the Co t_{2g} orbitals are more than half-filled and degenerate and hence no direct B-B interactions occurs between them. Fe_B-Fe_B interactions are stronger than these two as the t_{2g} orbitals of Fe_B are half-filled and hence direct interactions are possible. However, since the Fe_B e_g orbitals are also half-filled, partial covalency with anions is also not possible(as seen in the extremely localised Fe densities of states), leading to a large anion shielding and a subsequent reduction in the B-B interaction in comparison to the A-B interaction.

Our calculated results of T_c and a comparison with experimental values are presented in Table 3.5. As expected, the critical temperatures calculated by a Mean field approximation overestimates the values. However, the calculated values reproduce the trends seen in the experiments with $CoFe_2O_4$ having a large T_C due to very large values of J_{AB} while the other two have rather small values of T_C due to competing J_{AB} and J_{BB} leading to non-collinear magnetic structures.

3.4 Summary

We have performed a systematic investigation into the structural and magnetic properties of CoB_2O_4 magnetic spinels by changing the B cation using first-principles Density functional theory based methods. The understanding of the properties of these compounds is done by quantifying the relative strengths of the crystal field effect and the exchange effect through an analysis of their electronic structures. We find that the electron-electron interactions of the magnetic cations play a very important role and without the incorporation of this, the correct ground state structures cannot be obtained. The strong electron correlations are responsible for significant local structural distortions at the octahedral B site and global tetragonal distortions for $CoMn_2O_4$. These are responsible for the trends in the electronic properties such as the band gap. The electronic structures of these compounds are significantly different as the B site cation is changed. This, in turn, affects the inter-atomic magnetic exchange interactions considerably and is responsible for very different spin structures of these systems. In this work, for the first time, understanding of the trends in the magnetic properties are attempted through proper quantification of the associated quantities and by providing necessary explanations from the trends in the local structural parameters and the electronic structures. The results hold immense significance with regard to the recent experimental results on $Co(Cr_{1-x}Fe_x)_2O_4$ and $Co(Cr_{1-x}Mn_x)_2O_4$ systems, where the chemical properties of the third magnetic atom in $CoCr_2O_4$, the sub-lattice occupancies and the structural distortions are thought to be giving rise to interesting functional properties. In the next two chapter, these issues will be addressed.

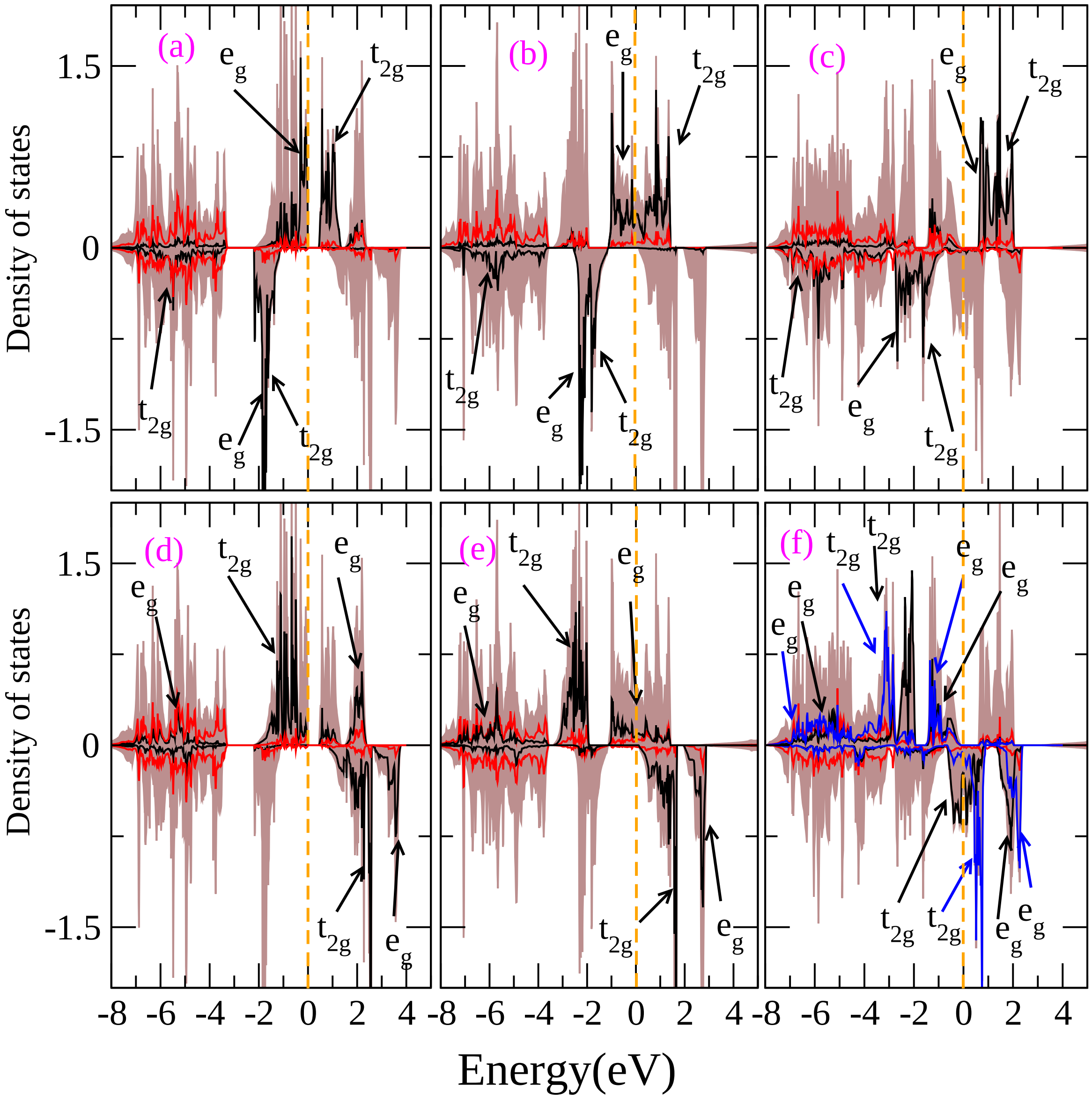

Fig. 3.4 In panel (a), (b) and (c), the site projected d-orbital densities of states of A cations(black curves) for $CoCr_2O_4$, $CoMn_2O_4$ and $CoFe_2O_4$ are shown respectively. In panel (c), (d), (e) the site projected d-orbital densities of states of B cations (black curve) for $CoCr_2O_4$, $CoMn_2O_4$ and $CoFe_2O_4$ are plotted respectively. In panel (f), the black curve stands for Co densities of states and the blue curve stands for Fe densities of states (This is because in $CoFe_2O_4$, B sites are occupied by Co and Fe). The 2p orbital projected density of state of oxygen atom for each case is plotted (red curve) to show its hybridisation with the corresponding cation. All calculations are done with $U = J = 0$, that is DFT only calculations.

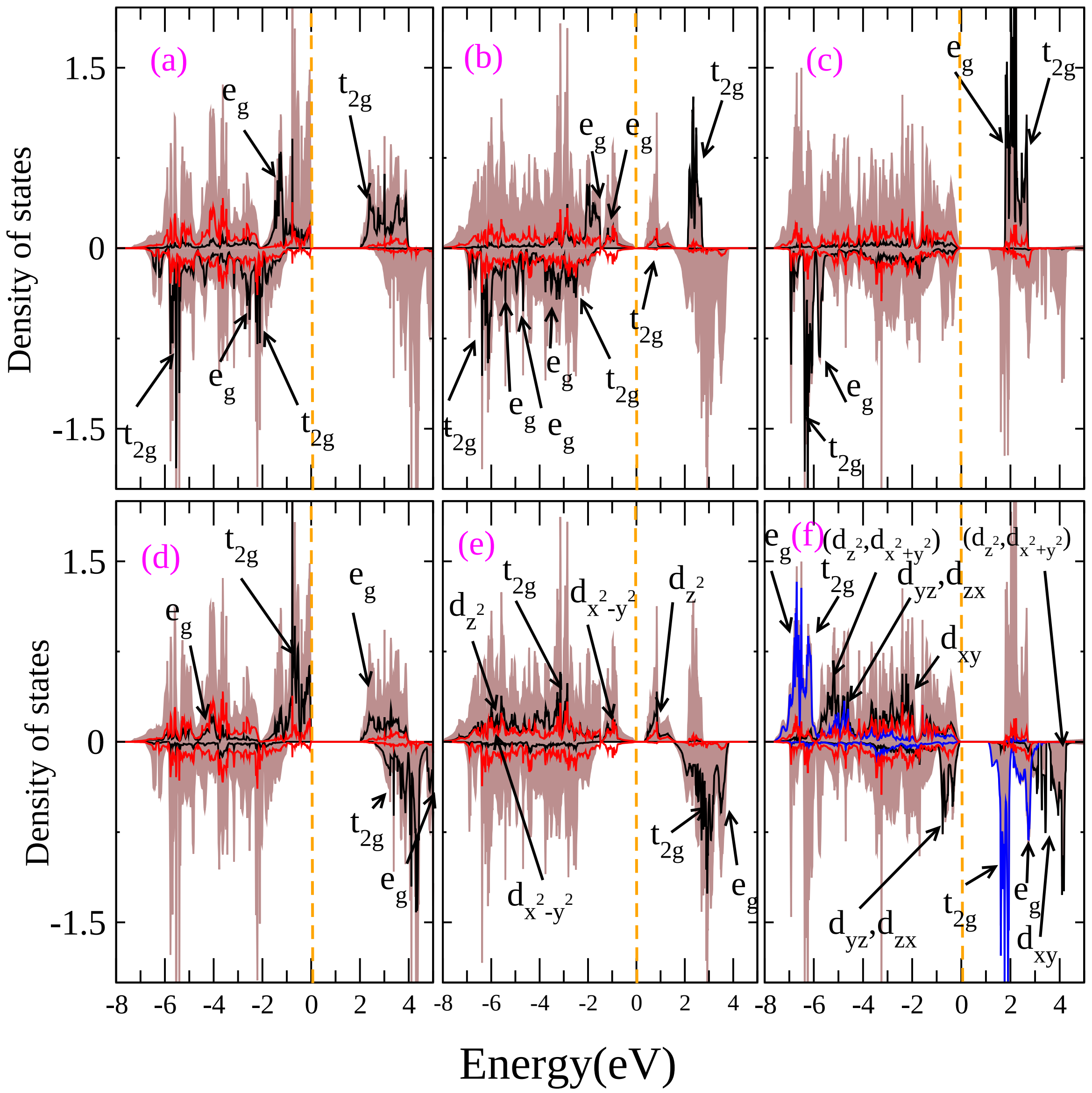

Fig. 3.5 In panel (a), (b) and (c), the site projected d-orbital densities of states of A cations(black curves) for $CoCr_2O_4$, $CoMn_2O_4$ and $CoFe_2O_4$ are shown respectively. In panel (c), (d), (e) the site projected d-orbital densities of states of B cations (black curve) for $CoCr_2O_4$, $CoMn_2O_4$ and $CoFe_2O_4$ are plotted respectively. In panel (f), the black curve stands for Co densities of states and the blue curve stands for Fe densities of states (This is because in $CoFe_2O_4$, B sites are occupied by Co and Fe). The 2p orbital projected density of state of oxygen atom for each case is plotted (red curve) to show its hybridisation with the corresponding cation. These curves correspond to the calculations where $U \neq 0$, $J \neq 0$, that is the DFT+U.

Chapter 4

First-principles electronic structure calculations of $Co(Cr_{1-x}Mn_x)_2O_4$ [†]

4.1 Introduction

In chapter 3, we have observed the differences in the structural properties, the electronic structures, the crystal fields and the exchange fields of $CoCr_2O_4$ and $CoMn_2O_4$. Mn substituted $CoCr_2O_4$ represented by the system $Co\left(Cr_{1-x}Mn_x\right)_2 O_4$ is expected to provide interesting insights into the site preferences of the cations, and it's associations with the changes in various properties as x increases. This is due to the fact that while $CoCr_2O_4$ has a cubic ground state (space group $Fd\bar{3}m$), $CoMn_2O_4$ is tetragonal with a significant elongation along z axis (space group $I4_1/amd$) [15, 26] as is demonstrated in chapter 3; there is no evidence of any cation disorder in the former while non-negligible cation disorder ($y = 0.22 - 0.39$)depending upon the annealing temperature is reported for the later [15, 41]. Investigations into the structural and magnetic properties by X-ray diffraction and SQUID [143] revealed a deviation in the variations of the lattice constant for smaller x values ($x < 0.15$) from the expected linear increase with x, a structural distortion for $x > 0.7$, a magnetic compensation at $x \sim 0.25$, and three different patterns of variations in magnetization depending upon the ranges of x. The authors addressed this non-regular behavior in the lattice constants and the magnetization along with the phenomena of composition dependent magnetic compensation to the varying trends in the site preferences of the Mn atoms substituting the Cr. They explained the trends in the properties by assuming that the substituting Mn atoms first occupy the tetrahedral A sites upto the compensation point, and then they first occupy one of the B sites till a critical value of x and finally occupy the other

---

[†] The contents of this chapter are published in [29]

B site upon further increase in x. However, this investigation neither quantified the cation disorder, nor provided any microscopic picture behind the non-regular behaviors.

With a motivation to understand the observed non-regular phenomena in $Co\,(Cr_{1-x}Mn_x)_2\,O_4$ from microscopic point of view and thus interpret them with a robust framework, in this work, we provide a detailed account of the composition dependence and thermodynamics of the cation disorder in $Co\,(Cr_{1-x}Mn_x)_2\,O_4$ by combining Density Functional Theory (DFT) based first-principles calculations and a thermodynamic model. These first-principles calculation based results substantiate the experimental claim of the site preferences of the Mn atoms by putting it on a solid theoretical ground. Concurrently, a systematic study of the structural, magnetic and electronic properties as a function of composition and degree of cation disorder is carried out. These results are interpreted in terms of the elements in the crystal field theory and the electronic structures, thus presenting the necessary microscopic picture governing the physics of this system.

4.2 Computational details

In an AB_2O_4 spinel, like $CoCr_2O_4$, with no cation disorder between the sub-lattices, the tetrahedral sites (A sites) are occupied by the A atoms in +2 charge state and the octahedral sites (B sites) are occupied by the B atoms in +3 charge state. In case of cation disorder between the sub-lattices where degree of cation disorder is denoted by the parameter y, the tetrahedral sites consist of a binary alloy $A_{1-y}B_y$ and each of the octahedral sites has the composition $A_{y/2}B_{1-y/2}$. The degree of cation disorder y at a finite temperature T can be calculated from the thermodynamic consideration of cation distributions by treating it as a simple chemical equilibrium [83]. Such modeling has been proved to agree reasonably well with the experiments in most of the cases [84, 103, 102, 90, 121, 49, 99]. In this model, the configurational free energy of cation disorder per formula unit ΔF is given as

$$\Delta F = E_c - T\Delta S_c$$

E_c is the cation disorder energy per formula unit, T the temperature and ΔS_c the configurational entropy which is calculated using the general formula $\Delta S_c = -k_B \sum_{i,b} p_i^b \ln p_i^b$; p_i^b is the concentration of the cation b at the i-th sub-lattice. The equilibrium degree of cation disorder parameter y_0 at the given temperature T can, then, be obtained by minimizing ΔF with respect to y.

The $Co\,(Cr_{1-x}Mn_x)_2\,O_4$ system, for a given value of x can be represented as a $A\,(B_{1-x}C_x)_2\,O_4$ system. Since we are dealing with a more complicated cation disorder as our system has substitutional disorder with respect to one type of magnetic atom, one has to first decide on the compositions of each of the sub-lattice at a given value of x and for an arbitrary value of y. Ideally, the cation disorder should take place between all three magnetic atoms. However, in our system, Cr^{3+} has a very strong preference to the octahedral B sites, the octahedral site preference energy(OSPE) of Cr^{3+} has been found to be 46.7 kCal/mol while that of Mn^{3+} is 25.3 kCal/mol and that of Mn^{2+} is 0 [75]. Thus we can assume that the cation disorder will taken place only between the A and the C atoms, that is, Co and Mn respectively. In spite of this simplification, the compositions of the sub-lattices will be dependent upon the concentration x of the C atoms as shown in Table 4.1. For $x = 0.5$, the two different patterns of sub-lattice occupancy shown in Table 4.1 will be identical. The reason behind different compositions for different ranges of x is due to the fact that the total concentration at the A sub-lattice cannot exceed 1; hence when the C content is greater than the B content, the C atoms, in excess of 1 must occupy the octahedral B sub-lattice. This is not satisfied if one uses the compositions for $x < 0.5$ listed in Table 4.1 as the compositions for $x > 0.5$ for $y = 1$.The configurational entropy now assumes the form

$$\begin{aligned}
\Delta S_c &= -k_B[(1-2xy)\ln(1-2yx)+2xy\ln(2xy) \\
&\quad +2(1-x)\ln(1-x)+2xy\ln(xy) \\
&\quad +2(x-xy)\ln(x-xy)], \qquad x<0.5 \\
&= -k_B[(1-y)\ln(1-y)+y\ln y+2(1-x)\ln(1-x) \\
&\quad +y\ln(y/2)+(2x-y)\ln((2x-y)/2)], \quad x>0.5
\end{aligned}$$

The non-configurational contributions towards the entropy, such as the contributions from lattice vibrations, have been ignored in the expression for ΔF as they have found to be typically small compared to the configurational parts [103, 102, 99, 84]. However, for magnetic systems, contributions from the magnetic entropy can be important in cases of severe fluctuations in magnetic moments of a particular constituent [84]. In the present work, we have incorporated it in the expression for ΔF wherever appropriate, and will be discussed later.

Table 4.1 Compositions of A and B sub-lattices in $A\left(B_{1-x}C_x\right)_2O_4$ for different ranges of x.

Conc. x	Composition at A site	Composition at B site
< 0.5	$A_{1-2xy}C_{2xy}$	$B_{1-x}A_{xy}C_{x-xy}$
> 0.5	$A_{1-y}C_y$	$B_{1-x}A_{y/2}C_(x-y/2)$

The cation disorder energy E_c is the energy difference between a state with cation disorder y and the "normal" state ($y = 0$) and should take into account the changes in the electrostatic and short-range interactions, the crystal fields and charge states. Neil and Navrotsky [87] have shown that E_c follows a quadratic dependence on y in the form $E_c = \alpha y + \beta y^2$; α, β are the parameters. The quadratic dependence was also empirically recognized by Kriessman and Harrison [58]. The advantage of this simple dependence of E_c on y is that the total energies need to be calculated only for a few values of y and the energies can be fitted to the quadratic form so that the energy of cation disorder can be interpolated for any value of y between 0 and 1. In the present work, we have calculated the total energies of our systems, at each x, for three different y values 0,0.5 and 1. The energies are then fitted to the above quadratic form, in order to obtain the dependence of E_c on y for the entire range of y.

Modeling of the substitutional disorder in a condensed matter system is a challenging problem. Although disorder of any arbitrary degree is now routinely addressed by the mean field Coherent Potential Approximation (CPA) [113] in conjunction with multiple scattering Green's function methods [131, 33], it has a serious limitation in dealing with systems having significant local distortions. In case of ternary spinels, the local distortion is significant even without cation disorder as is being seen by the deviations of the oxygen parameter u from it's ideal value of 0.25 [99, 40, 28]. With the introduction of a substituting element having very different ionic radius, the distortion gets amplified [26]. Due to this, a recent investigation into the effects of Fe substitution in $CoCr_2O_4$ using the CPA had limited itself to very low concentration of Fe so that the local distortions do not have appreciable effects [40]. Since we are interested to explore the properties for the entire range of x, varying between 0 and 1, we have taken the alternative approach of modeling the substitutional disorder by constructing supercells of the spinel unit cell. In this approach, addressing an arbitrary x often becomes difficult as the supercell size becomes prohibitively large. We have therefore considered $x = 0.0625, 0.125, 0.25, 0.5, 0.75$ and 1 for the present study. Such choices, nevertheless, cover the composition regimes where the experimental observations need to be addressed and interpreted.

For $Co\,(Cr_{1-x}Mn_x)_2\,O_4$ system, a unit cell of 14 atoms is considered. This unit cell is sufficient for simulating the three different degrees of cation disorder given by $y = 0, 0.5, 1$ for $x = 0.25, 0.5, 0.75$ and 1. However, this unit cell is not sufficient for the other two concentrations. Therefore, we have considered a 56 atom supercell for all x except $x = 0.0625$; a 112 atom supercell, the minimum one, was required for this concentration in order to address all three degrees of cation disorder. Comparisons with the 14 atom basic unit cell is done wherever possible. In Table 4.2 we show the configurations at A and B sites for each x and y. The magnetic configuration in all cases have been taken to be *Néel*

Table 4.2 Compositions of A and B sub-lattices in $Co\,(Cr_{1-x}Mn_x)_2\,O_4$ for different values of x, y and different unit cells considered. The entries in the column "Cell size" denote the number of atoms in the cell.

Conc. x	Cell size	y	Composition at A site	Composition at B site
0.0625	112	0	Co_{16}	$Cr_{30}Mn_2$
		0.5	$Co_{15}Mn_1$	$Cr_{30}Mn_1Co_1$
		1.0	$Co_{14}Mn_2$	$Cr_{30}Co_2$
0.125	56	0	Co_8	$Cr_{14}Mn_2$
		0.5	Co_7Mn_1	$Cr_{14}Co_1Mn_1$
		1.0	Co_6Mn_2	$Cr_{14}Co_2$
0.25	56	0	Co_8	$Cr_{12}Mn_4$
		0.5	Co_6Mn_2	$Cr_{12}Co_2Mn_2$
		1.0	Co_4Mn_4	$Cr_{12}Co_4$
0.50	56	0	Co_8	Cr_8Mn_8
		0.5	Co_4Mn_4	$Cr_8Mn_4Co_4$
		1.0	Mn_8	Cr_8Co_8
0.75	56	0	Co_8	Cr_4Mn_{12}
		0.5	Co_4Mn_4	$Cr_4Mn_8Co_4$
		1.0	Mn_8	$Cr_4Mn_4Co_8$
1.0	56	0	Co_8	Mn_{16}
		0.5	Co_4Mn_4	$Mn_{12}Co_4$
		1.0	Mn_8	Co_8Mn_8

[52] configuration, with spins of A and B sub-lattices anti-aligned. Although the magnetic structure of the end compounds of the system under investigation are non-collinear at low temperatures, it is difficult to model, particularly since the progression of it with x is not known. Thus we have considered the collinear Ferrimagnetic structure which would help in qualitative understanding of the magnetisation as the composition x or degree of cation disorder y is changed. Before fixing *Néel* configuration as the magnetic configuration, we have done several calculations with different spin configurations at different sub-lattices. In almost all cases, the *Néel* configuration came out to be energetically lowest. In cases where it was not, the lowest energy spin configurations were lower by less than 0.1 meV per atom. This, thus, further justifies consideration of *Néel* configuration for all x and y. The small values of energy differences between *Néel* and other configurations also indicate that the magnetic structures may be spin disordered.

The total energies, the structural parameters, the magnetic moments and the electronic structures were calculated by the DFT+U [2] method using Projector Augmented Wave (PAW) [11] basis set as implemented in VASP [57] code. The effects of electron localisation were addressed by the approach of Dudarev *et al* [31]. The Hund's coupling parameter J was taken to be 1 eV, while the Coulomb parameter U was taken to be 5 eV for Co and 3 eV for Cr and Mn. A plane wave cut-off of 550 eV and a $5 \times 5 \times 5$ mesh centered at Γ point for Brillouin zone integrations have been used throughout with the only exception for $x = 0.0625$ where a $2 \times 2 \times 2$ mesh was enough to achieve an energy convergence of 10^{-7} eV. Force convergences of 10^{-4} eV/ were ensured during structural relaxations.

4.3 Results and Discussions

4.3.1 Temperature and concentration dependence of degree of cation disorder y

Before discussion of the physical properties of $Co(Cr_{1-x}Mn_x)_2O_4$, it is required to find out the degrees of cation disorder between Co and Mn as a function of Mn concentration x and the temperature T. The temperature dependence is important because earlier works on various spinel compounds have demonstrated that y may be quite sensitive to the annealing temperature [76, 86, 49, 99]. In Fig. 4.1 we show the dependence of the cation disorder energy E_c and the configurational free energy of cation disorder ΔF on y for different Mn concentration x, at a temperature 1500 K which is close to the annealing temperature of 1523 K reported in the experiment [143]. We find that the cation disorder is zero for all values of x if we do not consider the configurational entropy. This implies that all substituting

Mn atoms will be occupying the B sites if the effect of the entropy is not included. Upon inclusion of the entropy term, states with cation disorder that is with non-zero values of parameter y are stabilised. The results suggest that the equilibrium value of y at which ΔF is a minimum goes towards 0 as x increases till 0.5, that is, up to the composition when the Cr and Mn contents in the system are identical. Further increase in the Mn content that is at $x = 0.75$ increases the equilibrium value of y before it is further reduced when the Mn substitution is complete at $x = 1$. The quantitative variations of y_0, the equilibrium value of y with temperature T, shown in Fig. 4.2 shows this qualitative behavior clearly. At 1500 K, $y_0 = 0.4, 0.26, 0.17$ and nearly 0 for $x = 0.0625, 0.125, 0.25$ and 0.5 respectively. At $x = 0.75$, the value of y_0 is 0.28 which decreases to 0.13 when $x = 1$. This result, thus, suggests that in the beginning of Mn substitution in $CoCr_2O_4$, a significant amount of Mn prefers to occupy the tetrahedral positions, instead of the expected octahedral ones. As the Mn content increases, more and more Mn occupies the octahedral positions until one reaches the point where the Mn content is equal to Cr content ($x = 0.5$). Further increase in Mn content initially puts some of it again in the A sites, only to provide more preferences to the octahedral sites as the content increases towards complete substitution of Cr. The importance of this result is that it supports the qualitative picture of site occupancies as conjectured in the experiments [143]. The differences with the picture provided by the experimentalists is that they did not predict the re-emergence of the phenomenon of Mn atoms preference to A sites after a critical composition. In the next sub-sections we will provide an explanation of this.

The other important outcome of the thermodynamics of cation disorder is that the degree of cation disorder in this system is not very robust as can be made out of the substantial variations in y_0 with temperature. For any value of x, y_0 decreases continuously towards 0, and at room temperature the cation disorder for most of the compositions are insignificant. As cation disorder is suggested to be the reason behind non-regular behaviors of magnetisation and phenomenon such as magnetic compensation [143], the importance of our results is that it provides the temperature range over which the degree of cation disorder is substantial and hence the experimental preparation of the samples should be done accordingly. This also suggests that the cation disorder in these systems can be manipulated by controlling the temperatures. Such manipulations of cation disorder can substantially affect functional properties like the electrical conductivity as has been seen elsewhere [84].

4.3.2 Structural parameters and their variations with x and y

The first signature of cation disorder upon Mn substitution in $CoCr_2O_4$ was noted upon non-regular variations in their measured lattice constants with increasing Mn content, in the

Table 4.3 Calculated cation-anion bond distances (in) in $Co\,(Cr_{1-x}Mn_x)_2\,O_4$ for different x and y values.

		A site		B site		
x	y	Co-O	Mn-O	Cr-O	Mn-O	Co-O
0	0	2.00	-	2.01	-	-
0.0625	0	2.00	-	2.01	2.07	-
	0.5	2.00	2.04	2.01	1.98	2.10
	1	2.00	2.04	2.01	-	2.10
0.125	0	2.00	-	2.01	2.06	-
	0.5	2.00	2.04	2.01	1.97	1.97
	1	1.99	2.03	2.01	-	1.97
0.25	0	2.00	-	2.01	2.07	-
	0.5	2.00	2.04	2.01	2.07	1.97
	1	1.99	2.03	2.01	-	1.96
0.5	0	2.00	-	2.01	2.07	-
	0.5	2.00	2.04	2.01	2.07	1.95
	1	-	2.03	2.01	-	1.95
0.75	0	1.99	-	2.01	2.1 ± 0.15	-
	0.5	2.00	2.04	2.01	2.06 ± 0.1	2.09 ± 0.03
	1	-	2.03	2.02	2.1 ± 0.14	2.03 ± 0.04
1.0	0	1.99	-	-	2.13 ± 0.17	-
	0.5	2.02	2.02 ± 0.04	-	2.1 ± 0.13	2.09 ± 0.07
	1	-	2.02 ± 0.04	-	2.12 ± 0.14	2.04 ± 0.12

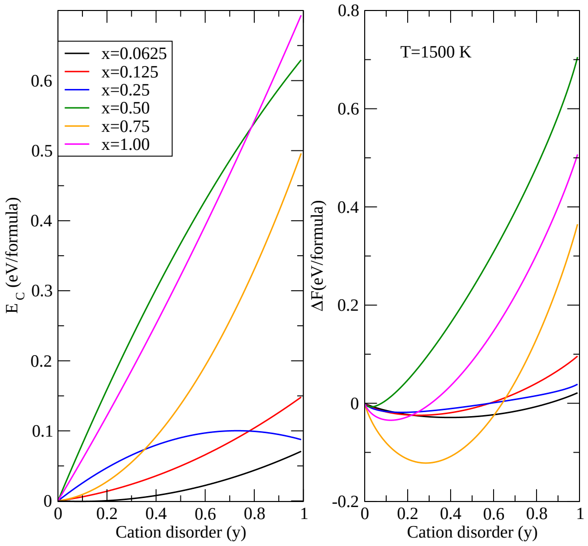

Fig. 4.1 Variations of the cation disorder energy(E_c) (left panel) and the configurational free energy (ΔF)(right panel) with degree of cation disorder y of $Co\,(Cr_{1-x}Mn_x)_2\,O_4$, for different values of x, the Mn concentration, at 1500 K, the annealing temperature of the experiment [143]. The equilibrium inversion parameter (y_0) at a given T and for a given x is obtained from the minima of ΔF.

low Mn content regime [143]. If the Mn, expected to be in +3 charge state, had occupied the B sites from the beginning, the lattice constant should have increased linearly with Mn content x as Mn atoms have larger ionic radii than Cr at B sites [104]. We, therefore, first discuss the variations in the structural parameters with concentration of Mn as well as with variations in the degree of cation disorder. In Table 4.3, we present various cation-anion bond distances at sites of different symmetries and their variations with x and y. In Table 4.4, we present the lattice constants a and c along with the oxygen parameters u_x, u_z for various x and y. The lattice constants and the cation-anion bond distances are obtained from the DFT+U calculations. The oxygen parameters are then obtained as [107]

$$u = \frac{-11 + 6r^2 + \sqrt{33r^2 - 8}}{24\,(r^2 - 1)}$$

where $r = \bar{R}_B/\bar{R}_A$, the ratio of the average cation-anion bond distances at the B and the A sites; $\bar{R}_B, \bar{R}_A$ are obtained by concentration averages of individual cation-anion bond distances. The results show that for x upto 0.5, the systems retain the cubic structure for all degrees of cation disorder, in agreement with the experiments. For $x = 0.75$ and 1, a structural distortion leading to tetragonal phases are obtained, again in agreement with the experimental observations. Quantitatively, the lattice constants calculated by DFT+U are

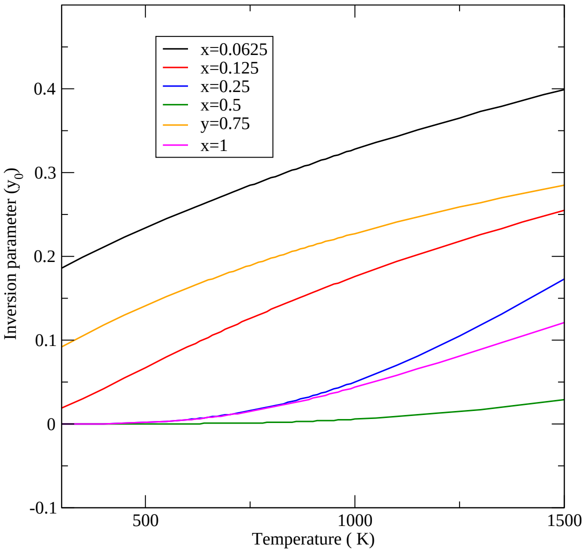

Fig. 4.2 Temperature dependence of the equilibrium inversion parameter (y_0) in $Co\,(Cr_{1-x}Mn_x)_2\,O_4$ for different x for the temperature ranging from room temperature to the annealing temperature of the experiment [143].

about $1-1.5\%$ higher than the experimentally measured ones. This is due to the choice of Generalised Gradient Approximation (GGA) [91] in describing the Exchange-correlation part of the Hamiltonian. However, the qualitative agreement with the experiments are reasonably good, with a small increase in lattice constants with x upto $x = 0.5$. It is to be noted that in the experiments, the deviation of the experimental lattice constant a from the expected linear behavior was observed for very small x ($x < 0.25$) and the maximum change was only about 0.1%. The maximum change in the DFT+U calculated lattice constant for the range $x = 0-0.25$ is about 0.3%, if we compare results of $y = 0$ only. The comparisons of results for cation disorder $y = 0$ is justified as we see that between $x = 0-0.125$, the lattice constant a does not change between $y = 0$ and $y = 0.5$ and that the equilibrium degree of inversion y_0 is well within this range of y moving towards $y = 0$ as x increases. For the concentrations $x = 0.75, 1$, we find that the qualitative nature of variations in the lattice parameters (c increases while a decreases) with x is in agreement with the experiment. For $x = 1$, the c/a ratio (for $y = 0$) obtained in our calculations is 1.12 which agrees very well with the experimental value of 1.09 [143]. We also find that the c/a ratio decreases to 1.1 when $y = 0.5$. Since our calculated equilibrium y is in between 0 and 0.5, the agreement with experiment would have been better had we considered the actual y_0 for the calculations. For $x = 0.75$, the calculated c/a ratio varies from 1.1 to 1.04 as y varies from 0 to 0.5 while the experimental value is 1.07. Thus our results qualitatively agree with the experiments as the calculated y_0 at this concentration is in between $y = 0$ and $y = 0.5$. Comparisons

Table 4.4 Calculated structural parameters of $Co\left(Cr_{1-x}Mn_x\right)_2O_4$ for different x and y values. The lattice constants a and c are in . u_x, u_z are the oxygen parameters.

x	y	c	a	u_z	u_x
0	0	8.43	8.43	0.262	0.262
0.0625	0	8.44	8.44	0.262	0.262
	0.5	8.44	8.44	0.262	0.262
	1	8.45	8.45	0.262	0.262
0.125	0	8.45	8.45	0.262	0.262
	0.5	8.45	8.45	0.262	0.262
	1	8.43	8.43	0.262	0.262
0.25	0	8.46	8.46	0.261	0.261
	0.5	8.43	8.43	0.262	0.262
	1	8.42	8.42	0.263	0.262
0.5	0	8.48	8.48	0.261	0.261
	0.5	8.44	8.44	0.263	0.263
	1	8.40	8.40	0.265	0.265
0.75	0	9.08	8.26	0.254	0.264
	0.5	8.68	8.35	0.259	0.263
	1	8.67	8.42	0.262	0.262
1.0	0	9.20	8.22	0.250	0.264
	0.5	9.06	8.24	0.257	0.264
	1	8.70	8.45	0.256	0.262

of our calculated u parameters with experimental results for an arbitrary x is not possible due to unavailability of reported experimental values. The comparisons can be made only for the end compounds. For $CoCr_2O_4$, the calculated u value of 0.262 agrees well with the experimental value of 0.264 [64]. For $CoMn_2O_4$, the calculated values of 0.255 and 0.267 for u_x and u_z ($y = 0$), respectively, agrees reasonably well with the experimental results of 0.230 and 0.261 [15]. Thus, overall, our calculated structural parameters and their trends with x are consistent with the trends of calculated y_0 with variations in x.

We next turn our attentions to the variations of the lattice parameters with cation degree of disorder y. The general trend seen in Table 4.4 is that with increase in y, the lattice constants decrease, except at $x = 0.0625$. This can be understood from the compositions of the A and B sites for different y and x and the variations in their bond distances (Table 4.3). For $x = 0.0625$, we find that while the cation-anion bond distances at A sites are insensitive to the degree of cation disorder, the $Mn_B - O$ bonds shorten considerably as y changes from 0 to 0.5. On the other hand, with $y = 0.5$, larger $Co_B - O$ bond distances, bring the average octahedral cation-anion bond distances equal to that at $y = 0$. Thus the lattice constants for $y = 0$ and $y = 0.5$ are identical. For $y = 1$, the B sites are completely occupied by the Co atoms making the average cation-anion bond distances associated with B sites larger, making a subsequent increase of the lattice constants with respect to $y = 0, 0.5$. The noticeable changes in the lattice constants with y for $x = 0.125, 0.25$ and 0.5 can be understood from the considerable decrease in the $Co_B - O$ bond distances with cation disorder. The significant reduction in the $Co_B - O$ bond distances from their values at $x = 0.0625$ reduces the average octahedral cation-anion bond lengths and consequently the lattice constants. For $x = 0.75$ and 1, the tetragonal distortions bring in a lot of dispersions in the bond distances as can be seen from Table 4.3. Once again, it is the octahedral bond lengths which decide the trends in the lattice constants. The overall decrease in the lattice parameter c with y is mainly brought about by the contracted $Mn - O$ bonds along the z-direction; the increase in a is due to subsequent expansions of the $Mn - O$ bonds in the xy-plane of the Mn octahedra.

We now try to provide explanations as to why the $Co_B - O$ bond distances reduce dramatically for certain concentrations and degrees of cation disorder. It is expected that Co at both sites will be having a +2 charge state. In that case, the effective ionic radius of Co should be 0.75 Åat B site and 0.58 Åat A sites [104]. The $Co - O$ bond distances at A sites, thus, would be considerably lower than that for Co at B sites. Our calculations are consistent with this for $x = 0.0625$ for all degrees of cation disorder. For $x = 0.125, 0.25$ and 0.5, and for $y \neq 0$, our calculations show the opposite trend. This indicates that the Co at B sites for these cases would either be in a +2 charge state with low spin or in a +3 charge state with either high or low spin(The effective ionic radii of Co^{2+} in low spin state, Co^{3+} in high spin state and Co^{3+} in low spin states are 0.65 Å, 0.61 Åand 0.55 Å[104] respectively). From elementary crystal field theory [17], it is known that the OSPE of a d^7 configuration is more than that of a d^6 configuration in high spin state, while it is exactly opposite for a low spin state. Thus, the Co_B atoms for these x and y parameters are expected to be in a low spin +3 state (d^6 configuration). The results on magnetic moments, and the electronic structures, discussed in next sub-sections confirm this and will be dealt in more detail.

The reason behind the tetragonal deformations at $x = 0.75, 1$ can also be understood from the crystal field theory. In a comprehensive work, Dunitz and Orgel [32] had attributed the electronic configurations at the B and A sites to the degrees of distortion from cubic symmetry in spinels. Counting the average number of t_{2g} and e_g electrons of A and B sites obtained from the charge states of the cations, we find that for $y = 0$, the B sites have $(t_{2g})^3(e_g)$ like configurations, which will give rise to a large distortion in order to lift the degeneracy associated with the e_g states. With increase in the cation disorder, the presence of Co atoms in the B site reduces the degeneracies associated with the e_g orbitals. Thus, the degree of tetragonal distortions decrease as is seen from our calculated results of decreasing c/a with increasing y.

Finally, we try to explain the reason behind re-appearance of non-negligible cation disorder at $x = 0.75$ after it had reduced to zero at $x = 0.5$. The arguments are based upon the bond distance results and elements of crystal field theory. From Table 4.3, we find that up to $x = 0.5$, $Mn_B - O$ bond distances were constant for $y = 0$ state. At $x = 0.75$, these bond lengths increase as a whole. From elementary crystal field theory, we know that the crystal field parameter Δ at octahedral site is inversely proportional to the cation-anion distance R ($\Delta \sim R^{-5}$)[17]. Thus, when the $Mn - O$ bonds increase in lengths at $x = 0.75$, the corresponding octahedral crystal field will become weaker in comparison to that for other concentrations significantly. Thus the octahedral crystal field stabilisation energy for the Mn atoms will reduce as it is decided by the strength of Δ. Thus there will be increased preference of Mn atoms towards A sites at $x = 0.75$ in comparison to $x = 0.5$. This is exactly reflected in the re-emergence of non-zero y_0 at $x = 0.75$. In the next sub-sections we provide more conclusive evidences of the possible charge and spin states of various atoms in different crystal sites which will corroborate the explanations given here.

4.3.3 Magnetic properties and their dependencies on x and y

Table 4.5 The inter-atomic nearest neighbour magnetic exchange interactions (J_{ij} in eV; i, j stand for tetrahedral (A) and octahedral (B) sites. for various specie pair in $Co\,(Cr_{1-x}Mn_x)_2\,O_4$ with variations in x, the concentration of Mn. All calculations are done with $y = 0$, the state with no cation disorder. The results for $y = 0.5$ in case of $x = 0.5$ are given in parentheses.

	J_{AB} (meV)		J_{BB} (meV)			J_{AA} (meV)
x	$Co-Cr$	$Co-Mn$	$Cr-Cr$	$Cr-Mn$	$Mn-Mn$	$Co-Co$
0	-2.83	-	-2.50	-	-	-0.49
0.0625	-2.83	-3.34	-2.15	-0.50	-	-0.50
0.125	-2.83	-3.31	-2.77	-0.40	-	-0.50
0.25	-2.80	-3.28	-2.70	-1.06	-	-0.47
0.50	-2.59 (-2.36)	-3.38 (-3.42)	-1.34(-3.88)	-1.64 (-4.98)	-3.39	-0.42
0.75	-4.26	-2.91	-	-1.32	-1.95 (out of plane) -8.64 (in plane)	-0.31
1	-	-3.47	-	-	-1.054 (out of plane) -9.46 (in plane)	-0.30

The magnetisation measurements [143] on $Co\,(Cr_{1-x}Mn_x)_2\,O_4$ show three distinct compositions ranges where the variations of magnetisations with composition are different, al-

Table 4.6 The total and atomic magnetic moments (in μ_B per formula unit) of $Co\,(Cr_{1-x}Mn_x)_2\,O_4$ for different concentrations x of Mn and for various degrees of cation disorder y .

x	y	A site		B site			
		μ_{Co}	μ_{Mn}	μ_{Cr}	μ_{Mn}	μ_{Co}	μ_T
0	0	-2.68	-	2.95	-	-	2.95
0.0625	0	-2.68	-	2.95	3.86	-	3.07
	0.5	-2.68	-4.50	2.95	3.23	2.71	2.84
	1	-2.68	-4.46	2.95	-	2.56	2.72
0.125	0	-2.68	-	2.95	3.87	-	3.19
	0.5	-2.68	-4.50	2.95	3.41	2.71	2.73
	1	-2.68	-4.50	2.98	-	0.18	1.76
0.25	0	-2.68	-	2.95	3.86	-	3.41
	0.5	-2.67	-4.50	2.93	3.84	0.05	2.00
	1	-2.68	-4.49	2.91	-	0.02	0.58
0.5	0	-2.67	-	2.94	3.83	-	3.89
	0.5	-2.68	-4.48	2.93	3.81	0.00	1.05
	1	-	-4.48	2.89	-	0.10	-1.81
0.75	0	-2.68	-	2.92	3.85	-	4.37
	0.5	-2.69	-4.49	2.88	3.80	2.72	2.53
	1	-	-4.40	2.89	3.80	3.07	2.54
1	0	-2.71	-	-	3.80	-	4.84
	0.5	-2.68	-4.48	-	3.70	2.71	3.01
	1	-	-4.39	-	3.78	3.07	3.02

though in all three regions, the variations are linear. For $x \sim 0-0.25$, the magnetisation decreases and reaches the point of magnetic compensation. Further increase of x shows a linearly increasing magnetisation till another critical point $x \sim 0.65$ after which the magnetisation decreases again with increase in Mn content. The explanation of this behavior was based upon the canted spin structures observed in $CoCr_2O_4$ [124] and $CoMn_2O_4$ [15]. The authors of Ref. [143] considered that like $CoCr_2O_4$, the canted spin structure will have opposing spin alignments at the two octahedral sites with one of them (site B_1) aligning with the tetrahedral site. The magnetic compensation behavior was, thus, attributed to the initial occupation of Mn atoms at both tetrahedral and the other octahedral site B_2 with opposing spin alignments, thus, canceling the net moment as Mn content is increased. The reason behind increase of the magnetisation after compensation was thought of due to Mn atoms occupying B_1 sites, diminishing the effects of Mn atoms at B_2 sites gradually, till the next critical point, after which the extra Mn atoms start occupying the B_2 sites again, bringing a decreasing trend in magnetisation as x increases. The experimentalists, however, did not substantiate their claim with detailed calculations. Their magnetisation measurements also indicated that the canting angles changed upon Mn substitution.

Before interpreting the experimental results and checking the validity of the arguments given in Ref. [143] we first present results on nearest neighbour inter-atomic magnetic exchange interactions J_{ij} for different x. These are calculated by mapping the DFT+U total energies for various collinear spin configurations on a Heisenberg Hamiltonian as discussed in section 3.4.4. The results are presented in Table 4.5 The calculations are done primarily for the "normal" spinel configuration ($y = 0$). Calculations for other y values require prohibitively large resources and often led to trouble in convergences of self-consistent cycles. Hence, results for $y = 0.5$ at $x = 0.5$ is only presented. The main point that can be made out of these results is that J_{AB} and J_{BB} where A stands for an atom at tetrahedral site and B stands for an atom at octahedral site, are comparable , J_{AA} being negligible. The competing exchange interactions make the spin structure non-collinear throughout the entire range of x as was suggested by the experiments. For the compositions where the crystal structure is cubic, J_{AB} do not vary much while the two prominent J_{BB} compete as x changes. As the Cr content reduces, the $Cr-Mn$ exchange interaction starts to strengthen at the expense of reduced $Cr-Cr$ interaction strength, until at $x = 0.5$, the strengths of the two interactions become comparable. At $x = 0.5$, Mn atoms have other Mn in their near neighbourhood due to their increasing content and thus have the strongest exchange interaction. The increased distances between Cr atoms and between Cr and Mn atoms due to reduced Cr content weaken $Cr-Cr$ and $Cr-Mn$ exchange interactions considerably. With further increase in the Mn content, and with tetragonal distortion, Cr has no Cr or Mn as nearest neighbours and the

J_{BB} is dominated by the Mn atoms. A strong anisotropy in the exchange interactions is observed due to the tetragonal distortions as was explained in Ref. [26]. The spin structures at these compositions, are. therefore, expected to be more complicated.

Since it is extremely difficult to model these non-collinear spin structures, particularly since no experimental information is available for Mn substituted samples, we took recourse to the results obtained from calculations on collinear *Néel* structure in order to interpret the experimental results qualitatively. Table 4.6 presents the results on atomic and total magnetic moments for each x and y. We find that the magnetic moments of Mn_A and Co_A are insensitive to the changes in x and y. As expected, the moment of Co_A atom is close to $3\mu_B$ implying that this Co is in a +2 charge state ($(e_g)^4(t_{2g})^3$ configuration). However, the moment of Mn at A site is rather close to $5\mu_B$ which implies that this Mn is primarily in a +2 charge state ($(e_g)^2(t_{2g})^3$ configuration). The reason behind this charge state of Mn_A can be understood from the fact that the OSPE for Mn^{2+} in high spin state is 0 while that of Mn^{3+} is 25.3 kCal/mol [75] and thus the probability of assuming +2 charge state is greater for Mn_A in high spin state. Significant variations in the magnetic moments with changes in Mn composition and in degree of cation disorder is observed for Co atoms at the B sites, while the moments of Cr and Mn at B sites have insignificant variations. The Cr and Mn atoms at B sites are in high spin, +3 charge states for all x and y. The much greater OSPE of Mn^{3+} and Cr^{3+} in high spin state in comparison to Mn^{2+} are responsible for this. The Co atoms at the octahedral positions oscillate between high spin and low spin states depending upon x and y. For $x = 0.0625$, irrespective of the degree of cation disorder, the Co_B are in high spin and +2 charge states as their moment is $\sim 3\mu_B$. For $x = 0.125$, while 50% of cation disorder ($y = 0.5$) still keeps Co spin and charge states same, complete "inversion" ($y = 1$) quenches the Co moment leading to a low spin state with moment ~ 0. This trend continues till $x = 0.5$ and is independent of the degree of cation disorder. The high spin state is regained at $x = 0.75$ and remains intact for $x = 1$ with $\mu_{Co} \sim 3\mu_B$ irrespective of the degree of cation disorder. As was argued in the previous sub-section, the relative OSPE values for Co^{2+} and Co^{3+} [17] clearly demonstrate that in the low spin state, Co^{3+} would have a greater preference towards B sites. One can relate the $Co_B - O$ bond distances (Table 4.3) with the low spin +3 charge state in this case using elementary crystal field theory. The significant decrease in $Co_B - O$ bond distances for a range of x and y, increases the Co_B crystal field. As a result these Co pair up the electrons. As the magnetic moment is close to zero, the configuration must be $(t_{2g})^6(e_g)^0$ which is consistent with the preferred +3 charge state as predicted from results on OSPE. The regaining of the high spin state at $x = 0.75$ can be understood from the increase in $Co_B - O$ bond lengths due to the structural relaxations, and subsequent weakening of the Co_B crystal field. As was mentioned earlier, due to the low spin Co moment at B site while the rest of the atoms at different sites are in high spin state, an additional magnetic entropy of $2k_B xy \ln 2$ is added to ΔF for the select x and y values. A non-zero y_0 value for these concentrations are obtained only if this magnetic entropy term is added. Thus, a cation disordered state at this concentrations is driven by the changes in the magnetic entropy.

Although the results are for collinear spin arrangements, in conjunction with the calculated y_0 values for each x, a qualitative variation in the total magnetic moment quite similar to the experimentally observed can be extracted by careful analysis of the results. Since y_0 for $x = 0.0625$ is ~ 0.4, the expected magnetic moment would be close to $2.84\mu_B$, the calculated value for $y = 0.5$. As the y is in the range of $0.17 - 0.4$ for x upto 0.25, the expected values of magnetic moments may decrease as x increases. An increase in the moment upon further increase of x, that is in the range $0.25 < x < 0.75$, is expected as the y_0 continuously reduces making the cation disorder close to zero, and thus the appropriate moments to look at from Table 4.6 would be the ones with $y = 0$ which shows continuous increase with x. Our results in the range $x = 0.75 - 1$, however, do not quite seem to follow experimental behavior qualitatively. At $x = 0.75$, the magnetic moment when $y = 0.28$, the y_0 value at this concentration should be close to $3.5\mu_B$ if the results between $y = 1$ and $y = 0.5$ are linearly extrapolated. This will indicate a decrease of moment as x changes from 0.5 to 0.75 agreeing with the experimental behavior. But the same extrapolation in case of $x = 1$ puts the magnetic moment at this concentration close to $4.5\mu_B$ which means an increase with respect to result at $x = 0.75$, in contradiction to the experimental trend. In spite of this disagreement, it is interesting that the results from collinear spin arrangement follow the experimental trend for a significant range of composition.

A qualitative model explaining the trends in the experimentally measured magnetisation can now be constructed by using the calculated atomic moments, the site occupancy patterns given in Table 4.1 and the alignments of sub-lattice spins obtained in the experiments. The experimental spin structure makes a distinction between two B sub-lattices which our collinear spin arrangement does not. If instead of considering the occupancies of both B sub-lattices to be identical, we consider that after part of Mn occupying the A sites in accordance with the pattern depicted in Table 4.1, the rest of the Mn for a given x completely occupies the B_2 sub-lattice which is anti-aligning with the B_1 and the A sub-lattice, then the experimental trends of magnetisation for $x = 0 - 0.25$ is qualitatively reproduced. This can be understood the following way: If we consider the DFT calculated atomic magnetic moments as the moments of individual atoms in this picture and consider that the B_2 sub-lattice has Cr and Mn while B_1 has Co and Cr, and the y value for each x is taken to be equal to calculated y_0, then with increase in x, the contribution of B_2 sub-lattice will gradually increase in comparison to the other two which will reduce the net magnetic moment steadily. The increasing dominance of B_2 will be due to the fact that with increase in x, the y steadily decreases and with rather small x, the content of Mn at the A site is always small. Since Cr_B and Co_A have identical moments, their moments from B_2 and the A sites will nearly cancel each other. Mn being the carrier of larger magnetic moments would have the maximum effect. Thus the Mn at B_2 site would control the magnetisation variation in this concentration range. With further increase in x, the y value is supposed to be getting smaller and nearly vanish for $x = 0.5$. Thus, in the concentration range $x = 0.25 - 0.5$, the Mn is going to occupy the B sites mostly. If we now once again let the occupancies of the two B sites be different with most of the extra Mn occupying the B_1 site, then the magnetic moment of the system will increase as x increases. This is because of the fact that since the occupancy of B_2 sub-lattice would not change much from what it was for $x = 0 - 0.25$, more Mn content at B_1 site with their spins anti-aligning to those of Mn in B_2 site would increase the total moment as the spins of B_1 and the A sites align. This occupancy pattern would continue till $x = 0.5$ and possibly a little further up till about the critical point ($x \sim 0.7$) observed experimentally. Since $y = 0$ when $x = 0.5$, the expected occupancies in A sub-lattice will be Co only, while both B sub-lattices will have equal amounts of Cr and Mn. With further increase in x and with expected y value nearly zero, B_2 will be equal amount of Cr and Mn and that of B_1 will be Mn rich $Mn - Cr$ alloy, thus shooting up the magnetic moment further. At $x = 0.75$, the cation disorder returns. Now the cation disorder will be between A and B_1 sites, with Co occupying the B_1 sites but the extra Mn mostly occupying the B_2 sites. As a result, the total moment steadily decreases as x increases. This picture, thus, not only corroborates what was espoused by the experimentalists, but also puts it on a solid theoretical footing by using information from first-principles calculations.

4.3.4 Electronic structures and their variations with x and y

Finally we present results on the electronic structures with variations in x for three degrees of cation disorder represented by $y = 0, 0.5$ and 1 in Figures 4.3, 4.4 and 4.5 respectively. For the "normal spinel" configuration ($y = 0$), the significant changes with Mn content happens in the majority (spin up) band, where Mn states occupy the states near Fermi level moving the Cr states to lower energies. At low concentrations of Mn, sharp peaks corresponding to half-filled e_g states on both sides of Fermi level are observed, which smear with increase in the Mn content. The Mn and Co states dominate the majority band with increasing x as expected. The Mn t_{2g} contributions are around 3-4 eV below Fermi level, the Co e_g states contribute mostly around 2-3 eV below Fermi level. The minority band consists of Co for energies below Fermi level. Thus, across the concentration range, Co is in a +2 state with fully filled e_g and half-filled t_{2g} orbitals, Cr is in a +3 state with half-filled t_{2g} and empty e_g orbitals and Mn is in a +3 state with half filled e_g and t_{2g} orbitals. Each of the three atoms retain their characteristics across the concentration range with the peaks corresponding to each of them occurring in distinctly separate energy regions. Due to the appearance of Mn states in the gap after Fermi level, the band gap decreases with x upto $x =$ 0.5 as reported in Table 4.7. For $x = 0.75$ and 1, the band gap again increases due to changes in the characteristics of the densities of states with the structural distortions. This is due to the shift of the Mn states near Fermi level and in the occupied part towards lower energy, At these concentrations, the majority and minority bands localise more, opening a larger gap. However, in going from $CoCr_2O_4$ to $CoMn_2O_4$, the band gap reduces considerably, due to the more delocalised Mn states as is apparent from the electronic structures presented here.

With 50% cation disorder($y = 0.5$), new and interesting features appear in the electronic structures. Like $y = 0$, we have sharp e_g peaks coming from Mn_B atoms in the unoccupied part of the majority band close to the Fermi energy for $x = 0.0625$ and 0.125. The contributions close to Fermi energy in the occupied part of the majority band now comes from e_g states of Co_B. The Mn_B contribution in the unoccupied part moves towards the Fermi level as x changes from 0.0625 to 0.125, thus reducing the band gap, as happened for $y = 0$ case. For these concentrations, the minority states near the Fermi level are made up of t_{2g} orbitals of Co_B and t_{2g} states of Mn_A atoms. At these concentrations, both Co_A and Co_B densities of states show completely filled e_g and half-filled t_{2g} orbitals. Thus Co at both sub-lattices are in +2 charge state. The densities of states significantly change at $x = 0.25$ and continue to

Table 4.7 The calculated Band gaps (in eV) of $Co\,(Cr_{1-x}Mn_x)_2\,O_4$ for different Mn concentrations x and different degrees of cation disorder y.

x	Cation disorder y 0.0	0.5	1.0
0.000	2.1	-	-
0.0625	0.77	0.66	1.99
0.125	0.70	0.33	1.61
0.250	0.38	0.64	1.53
0.500	0.15	0.58	1.44
0.750	0.23	0.48	0.62
1.000	0.33	0.00	0.56

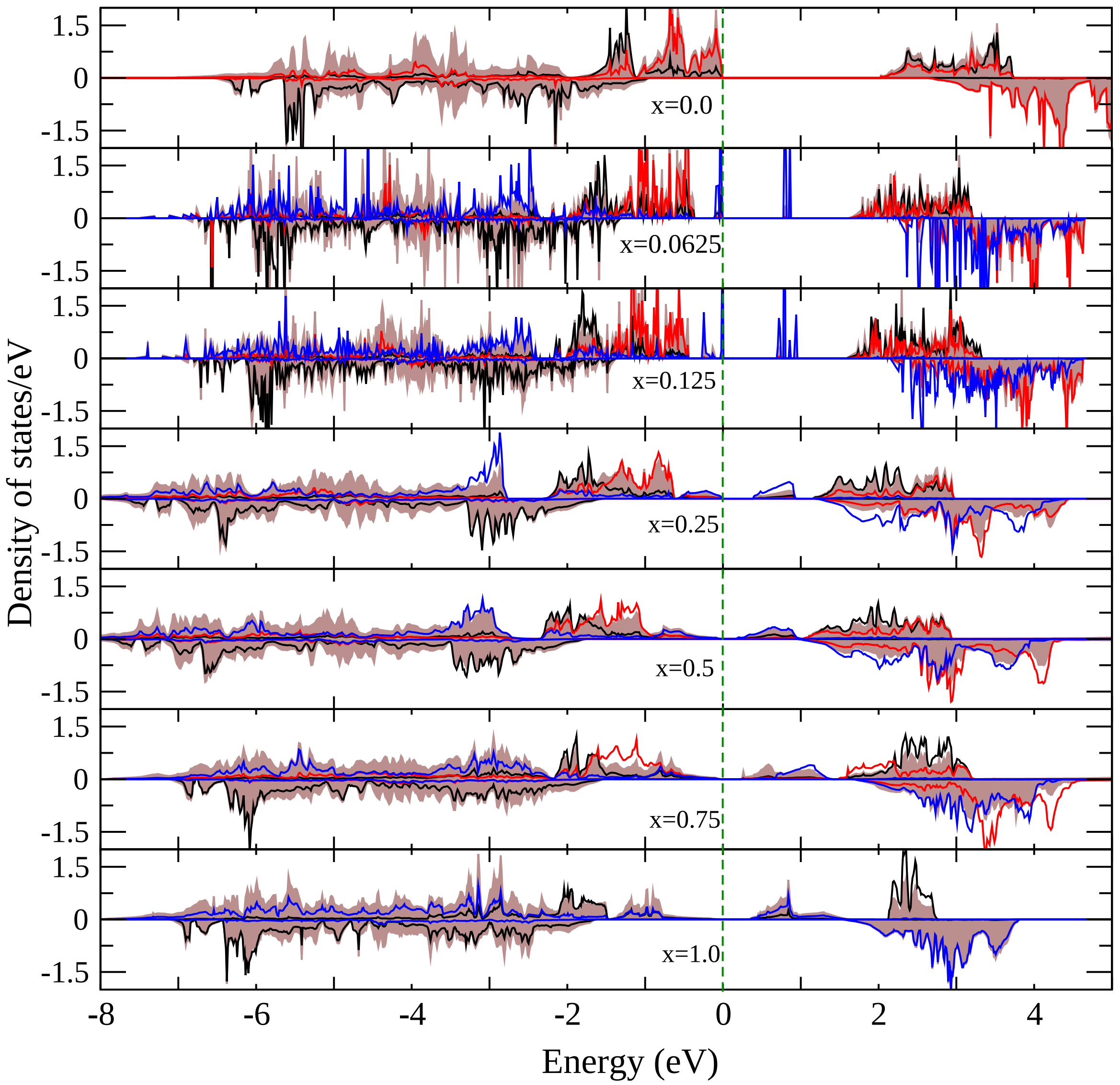

Fig. 4.3 Total and atom-projected densities of states of $Co\,(Cr_{1-x}Mn_x)_2\,O_4$ for different x. The results are for zero cation disorder ($y = 0$). The results for $CoCr_2O_4$ ($x = 0$) are also included. Here the total densities of states is denoted by brown shade. The black, red and blue curves represent atom projected densities of states of Co at A sites, Cr and Mn at B sites, respectively.

be so at $x = 0.5$. Now, the majority states in the occupied and unoccupied parts closest to the Fermi level are again due to the Mn_B atoms which increases the band gap in comparison to that at $x = 0.125$. This happens as Co_B states in the majority band are sharply localised accommodating only the t_{2g} electrons. The e_g states are now in the unoccupied part of the majority band and lie around 1-1.5 eV above Fermi level. The minority Co_B states consist of t_{2g} in the occupied part and e_g in the unoccupied part. Thus, the t_{2g} orbitals of Co_B are

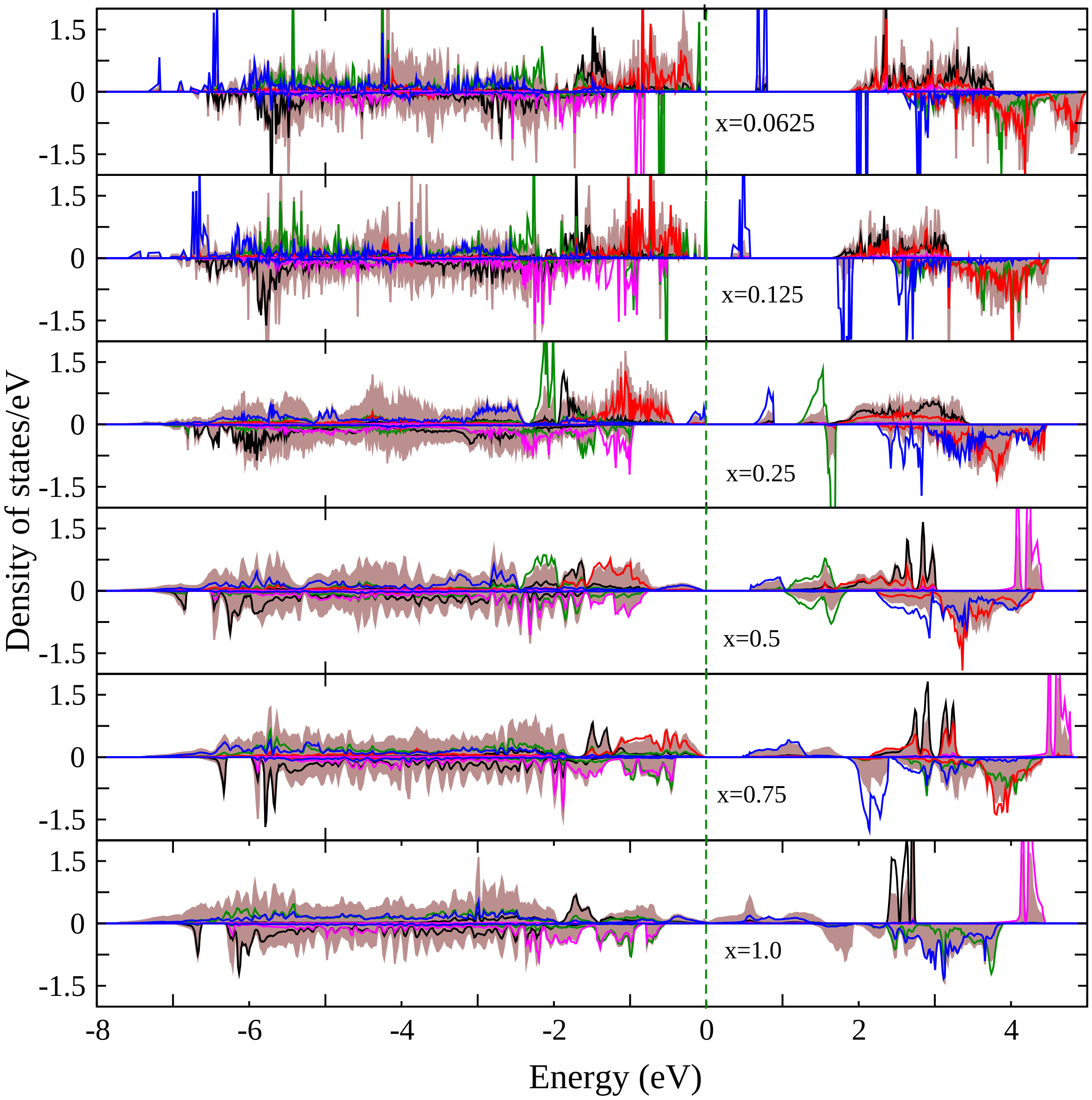

Fig. 4.4 Total and atom-projected densities of states of $Co\,(Cr_{1-x}Mn_x)_2\,O_4$ for different x. The results are for 50% cation disorder ($y = 0.5$).Here the total densities of states is denoted by brown shade. The black and the green curves represent atom projected densities of states for Co at A and at B sites respectively, the red curve represents atom projected densities of states for Cr, the pink and the blue curves represent atom projected densities of states for Mn atoms at A and at B sites respectively.

completely full and the e_g orbitals are completely empty. The Co_B atoms, therefore, are in low spin states and in a +3 charge configuration. This is consistent with our results on magnetic moments and the explanations based upon bond lengths. The strong splitting and localisations of the e_g and t_{2g} states also signify a stronger crystal field. The features in the

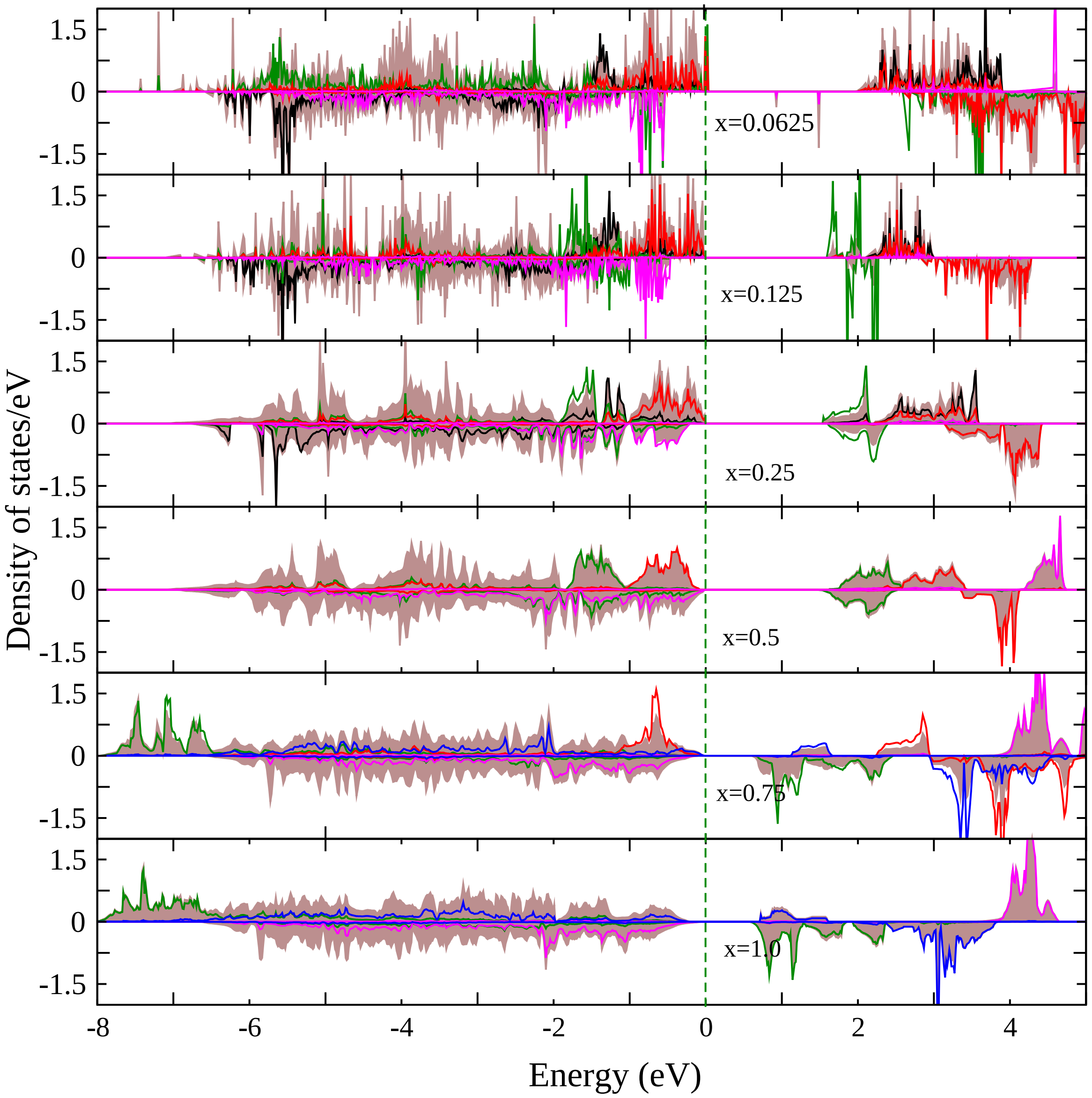

Fig. 4.5 Total and atom-projected densities of states of $Co\,(Cr_{1-x}Mn_x)_2\,O_4$ for different x. The results are for full inverse arrangement ($y = 1$).Here the total densities of states is denoted by brown shade. The black and the green curves represent atom projected densities of states for Co at A and at B sites respectively, the red curve represents atom projected densities of states for Cr, the pink and the blue curves represent atom projected densities of states for Mn atoms at A and at B sites respectively.

electronic structures, thus, support our arguments based upon crystal field theory given in earlier sub-sections. As a consequence, the band gaps increase from it's value at $x = 0.125$. The densities of states again change substantially with $x = 0.75$ onwards. The localised Co_B t_{2g} states for $x = 0.25, 0.5$ now delocalise considerably. The contributions due to e_g states of Co_B appear at lower energies (at about -6 eV) indicating reduction of the crystal field and return of Co_B to a +2 charge state. For these concentrations Mn_B start occupying the majority states near Fermi level and with a larger structural distortion at $x = 1$ in comparison to $x = 0.75$, the Mn_B e_g states get energetically closer, reducing the band gap. Thus the band gap reduces to zero at $x = 1$. The highlights in the densities of states of the other component in the cation disorder, the Mn atoms at the A sites have completely filled t_{2g} and e_g states in the minority spin channel along with completely empty majority spin channel. This implies that the electronic configuration of this Mn would be $\left(e_g^2 t_{2g}^3\right)$, a +2 charge state. Once again the results of the electronic structure confirms our picture on charge states as was discussed in earlier sub-sections.

With "complete inversion" that is for $y = 1$, we now see larger splittings in the majority bands for any given concentration, in comparison to $y = 0, 0.5$. Now the B sites consist of only Cr and Co atoms upto $x = 0.5$. In chapter 3, the octahedral crystal field parameters of Cr and Mn were calculated from first-principles. These were extracted from the pristine $CoCr_2O_4$ and $CoMn_2O_4$. The results showed that the crystal field of Cr is much stronger than that of Mn. In here, we have seen that the states on either side of the Fermi level are occupied by the octahedral atoms. Thus, when the B sites are occupied by primarily Cr, it's strong crystal field makes the band gaps larger in comparison to those for other degrees of cation disorder. With increasing Mn content, the crystal field at the B site starts losing it's strength, a signature of which is in the appearances of Co_B e_g states between 1-2 eV above Fermi level. Consequently, the band gap decreases with increase in Mn concentration. A significant reduction in the band gap is observed when x changes from 0.5 to 0.75. In this case, the Mn atoms have started to occupy the B sites which reduces the crystal field further. However, another interesting feature of the densities of states at this concentration is that the Co_A states in the majority bands are now localised at a significantly lower energy region. Concurrently, there are more states of Co_A in the unoccupied part of the minority band at energies closer to the Fermi level. This is the reason behind drastic reduction in the band gap. This happens due to the alteration in the charge state of Co_B. Upto $x = 0.5$, this Co was in a low spin state due to the strong crystal field which paired all t_{2g} electrons leaving e_g states empty. A inspection of the densities of states reveal that the crystal field is still strong with a significant splitting of e_g and t_{2g} states. Moreover, a comparison of Co_B densities of states for $y = 0.5$ and $y = 1$ for this concentration shows that in case of $y = 0.5$, the minority band had more densities of states in the energy region -0.5 to -2 eV below Fermi level. This implies that for $y = 1$, the Co_B has less electrons, and thus the charge state is probably +3. In the high spin state, octahedral Co^{3+} has a higher OSPE than Co^{2+} [17]. Thus when all Co are made to occupy the B sites as is done in case of $y = 1$, the expected charge state is +3. Thus the inferences from the features of the densities of states and the crystal field results are consistent. The Mn_A densities of states are by and large similar to that for $y = 0.5$ signifying that it's charge state is insensitive to the degree of cation disorder.

One outcome of the systematic explorations of the densities of states is the variations in the nature of the band gap. Since the band gap depends both on the concentration and degree of cation disorder quite substantially, manipulation of the composition and the cation disorder can be a route to engineering band gap in this material which can be subsequently used for applications like solar cells. This widens the functional scope of this material.

4.4 Summary and Conclusions

In this chapter, we have investigated the thermodynamics of cation disorder, the structural, the magnetic and the electronic properties of $Co\,(Cr_{1-x}Mn_x)_2\,O_4$ compounds and analysed the results from their electronic structures and the elements of the crystal field theory. Our results support the model of cation disorder between Co and Mn atoms as proposed by the experimentalists. The experimental non-regular behavior of magnetisation as a function of Mn concentration is explained on the basis of that. By generalising a thermodynamic model of cation disorder for AB_2O_4 compounds in this case, in conjunction with first-principles total energy calculations, we have quantified the cation disorder parameter for each concentration. Our results have explored the intimate relationships between the degree of cation disorder, the crystal fields associated with different atoms and their charge states, the structural and the magnetic properties. We have demonstrated that the non-regular behavior of the magnetic moments and the structural properties can be traced back to the features in their electronic structures. Our results show that the occupancies at the B sites and the associated crystal fields can explain the variations in the properties with varying composition and degree of cation disorder. By calculating the variations in the electronic band gap with variations in composition and degree of cation disorder, we have shown that the functionalities of this material can be enhanced by engineering the band gap by careful manipulation of the composition and the degree of disorder.

Overall, the contents of this chapter has paved a way to compute the thermodynamics of cation disorder in a $A\,(B_{1-x}C_x)_2\,O_4$ magnetic spinel and perform subsequent analysis to understand the microscopic details of such systems. In the context of the specific system considered in this work, our results have provided a robust theoretical background for interpretation of the experimental results.

Chapter 5

First-principles electronic structure calculations of $Co\left(Cr_{1-x}Fe_{x}\right)_{2}O_{4}$ [†]

5.1 Introduction

In $CoCr_2O_4$, the origin of the non-collinear spin structure is in the delicate balance of magnetic exchange interactions between various magnetic cations (Co and Cr in this case) occupying different crystallographic sites. It is only natural to investigate the influences of the variations in the occupancies at the tetrahderal and octahedral sub-lattices on the ferroelectric polarisation and on the physical properties, in general. To this effect, few studies on substitution of Cr with Fe in $CoCr_2O_4$ [142, 89, 88, 96, 62] have been done recently. The substitution of Fe at the Cr site is expected to provide more interesting aspects of the interrelations between the site occupancies and the magnetic interactions than observed in Mn substituted $CoCr_2O_4$. The end compounds $CoCr_2O_4$ and $CoFe_2O_4$ have very different site occupancy patterns as well as magnetic structures, as shown in chapter 3. In contrast to “normal” spinel $CoCr_2O_4$, $CoFe_2O_4$ is considered as "inverse" spinel. For $CoFe_2O_4$, the degree of cation disorder is found to be the decisive factor for it’s electronic ground state. While one work [34] reported the ground state of this system to be insulating, another group [117] reported it to be a half-metal. The calculations by Ganguly *et al*[40] conclusively showed that the cation disorder at tetrahedral and octahedral sites, irrespective of the degree decided by y, drives the system towards half-metallicity due to the significant changes in the electronic structure. Also, the magnetic transition temperature of $CoFe_2O_4$ is quite high (860 K) in comparison to $CoCr_2O_4$. The *ab initio* calculation of exchange interactions in complete "inverse" $CoFe_2O_4$ presented in chapter 3 shows that the large value of the magnetic tran-

---

[†] Part of the contents of this chapter are published in [27]

sition temperature is due to a collinear spin structure which is driven by overwhelmingly dominating exchange interaction between A and B sites. Thus, when Cr is gradually substituted by Fe, to make a systematic transition towards $\mathrm{CoFe_2O_4}$ from $\mathrm{CoCr_2O_4}$, two different factors, the degree of cation disorder and the magnetic exchange interactions, would play pivotal roles.

Recent experimental attempts of Fe substitution in $\mathrm{CoCr_2O_4}$ has been remarkable. Magnetic measurements on 10% and 15% Fe substituted $\mathrm{CoCr_2O_4}$ reported a magnetisation reversal and a sizeable exchange bias around a critical temperature, accompanied by non-monotonic changes in the local moments [89, 88, 96, 62]. They attributed these phenomena to the magneto-structural changes arising out of the cation disorder and subsequent spin re-orientations at the cationic sub-lattices, due to the presence of Fe substituting Cr. Magnetic and specific heat measurements [142] for $\mathrm{Co}(Cr_{1-x}Fe_x)_2\mathrm{O_4}$, $0 \leq x \leq 0.5$ scanned a larger composition regime and concluded that the magnetisation reversal can be understood in terms of role reversals of the magnetic contributors at different sub-lattices, the origin of which lies in the changes in the sub-lattice occupancies of the Fe atoms. Their specific heat versus temperature results indicated that the occupancies of the Fe atoms at different sub-lattices was the reason behind the suppression of the conical spin structure and the emergence of a collinear magnetic structure as Fe concentration in the system increases. The calculations of the magnetic exchange parameters for $0 \leq x \leq 0.1$ [40] for the "completely inverse" and "normal" structures showed that the A-B exchange interactions gain significance over the B-B ones as x increases, thus predicting that the system will be driven towards collinearity by the exchange interactions between Fe atoms at tetrahedral sites and Co atoms at octahedral sites.

Two things were hitherto unavailable in these investigations: (i) the computations of the "degree of cation disorder" y at different values of x in $\mathrm{Co}(Cr_{1-x}Fe_x)_2\mathrm{O_4}$ so that the ideas about the site-occupancies at the operational temperatures of the experiments can be obtained and (ii) a systematic investigation into the effects of site preferences of the cations on the physical properties of this system for the complete composition range ($0 \leq x \leq 1$) within the same approximation and a single methodological framework so that a consistent trend and thus, the understanding of the physics associated with the system, can be achieved. In this chapter we attempt to address these shortcomings by computations of the site occupancy patterns of the cations as the composition changes and then uttilyising it to further investigate the dependencies of the structural parameters, the magnetic exchange parameters and the electronic structures on the composition and the degree of cation disorder. Our major focus in this work is to obtain a microscopic picture about the emergence of a collinear magnetic structure from a non-collinear one. To do this systematically, we first try to gain insights about the effects of Fe substitution at different crystallographic sites of $CoCr_2O_4$ by performing an impurity calculation. Afterwards, we carry out investigations into the site occupancies and their impacts on the structural properties, electronic structures and magnetic interactions for the range 0.0625≤x≤0.75.

5.2 Details of calculations

As done in chapter 4, we consider a 112 atom supercell comprising of 16 Co atoms, 32 Cr atoms and 64 oxygen atoms to describe $CoCr_2O_4$. For the impurity calculation, we replace one Cr atom with one Fe atom. The resulting composition of the system is $Co(Cr_{0.96875}Fe_{0.03125})_2O_4$. For the $Co(Cr_{1-x}Fe_x)_2O_4$ with 0.0625≤x≤0.75, systems, we have followed the modeling scheme described in section 4.2. The total energies, the structural parameters and the electronic structures are calculated with the DFT+U method using PAW basis set as implemented in VASP code. The U and J parameters for describing the electron-electron correlations are kept at same values mentioned in chapter 3. The plane wave cut-off , the size of the k-mesh , the convergence criteria on energies and forces are kept the same as chapters 3 and 4.

5.3 Fundamental aspects of Fe substitution in $CoCr_2O_4$

Before embarking on investigating the $Co(Cr_{1-x}Fe_x)_2O_4$ system for different x, we try to gain some knowledge about the impacts of Fe substitution on properties of $CoCr_2O_4$ by replacing one Cr with one Fe in a 112 atom supercell. We first look at thee effects on the structural aspects of the system as the previous two chapters have demonstrated that the structural aspects are related with other electronic structure related effects. we first try to quantitatively assess the structural distortions in this compounds. The quantification of structural distortion can be done by the angles θ_{T_d} and θ_{O_h}. Which denote the distortions from perfect tetrahedral and octahedral symmetries, and are defined as,

$$\begin{cases} \theta_{T_d} = \Sigma_{i=1}^{4} \frac{|109.5-\theta_i^{T_d}|}{4} \\ \theta_{O_h} = \Sigma_{i=1}^{8} \frac{|90-\theta_i^{O_h}|}{8} \end{cases} \tag{5.1}$$

$\theta_i^{T_d}, \theta_i^{O_h}$ are the anion-cation-anion bond angles corresponding to the i^{th} bond for the tetrahedral and octahedral symmetries respectively.

Before discussing the single Fe substituting Cr in $CoCr_2O_4$, we look at the structural properties of pristine $CoCr_2O_4$. Since we are interested in the comparative effects on structural properties for pristine and substituted $CoCr_2O_4$, we keep the lattice constant of $CoCr_2O_4$ at the experimental value of 8.335 Å[64] and optimize only the oxygen parameter u. The value of u comes out to be 0.261 in good agreement with available results [64, 34]. For the Fe substituted $CoCr_2O_4$, we keep the same lattice parameters as a amount as low as 3.125 % per B site would not change the lattice parameters appreciably [142]. In Figure 5.1 we show a part of the neighbourhood of Cr and Co atoms in $CoCr_2O_4$. All the relevant angles and bond lengths are shown in the figure. The estimated value of $\theta_{T_d} \sim 0.03^0$[the angles vary between 102.56^0 and 109.48^0] is much smaller than θ_{Oh} which is about 5.34^0[the angles vary between 84.67^0 and 95.34^0]. The results suggest that the distortions associated with the tetrahedral sites are negligible.

Upon substitution of a single Fe at the A site (and thus replacing a Cr atom at the B site by a Co atom), we find that the oxygen atoms in the Co octahedra move outwards while those in the Fe tetrahedra moves inwards resulting in slight contractions in the substituted tetrahedra and slight expansions in the substituted octahedra. This can be understood from the fact that Co^{2+} has a larger ionic radius (0.885 Å) than Cr^{3+} (0.755 Å) in the octahedral environment while Fe^{3+} has a smaller ionic radius (0.63 Å) than Co^{2+} (0.72 Å) in the tetrahedral environment.

In Figure 5.2, we show the neighbourhood of the substituted transition metal cations along with the relevant structural parameters. Upon Fe substitution at A sites, the $Fe_A - O - Cr$ and the $Fe_A - O - Co_B$ angles (Fe_A stands for Fe atom at A sites and Co_B stands for Co atom at B site) increase and decrease respectively in comparison to the $Co - O - Cr$ angles in $CoCr_2O_4$. The values of θ_{T_d} and θ_{O_h} are $\sim 0.71^0$[the angles vary between $108.36^0 - 112.32^0$] and 5.95^0 [the angles vary between $83.80^0 - 96.95^0$] respectively. This implies that the distortion in the tetrahedral environment is more due to Fe substitution at tetrahedral sites. These results indicate that the degeneracies in the d-orbitals of the transition metal atoms are going to be affected and one can expect a significant impact on the electronic structure.

In what follows, we provide an understanding of the effects of the structural distortion and electron-electron correlation on the electronic structure of the constituents by a study of crystal field (CF) splitting and exchange splitting (EX) through an analysis of the corresponding densities of states. In first two rows of Table 5.1 we show the crystal field splittings and the exchange splittings associated with different spin channels and different orbitals of pristine $CoCr_2O_4$ respectively. The values shown here are slightly smaller than those listed in Table 3.3. This is because of using a smaller lattice constant in this calculation. However, the relative strengths of different Δ_{EX} and Δ_{CF} remain same, inspite of changes in the lattice constant signifying no changes in the physical picture.

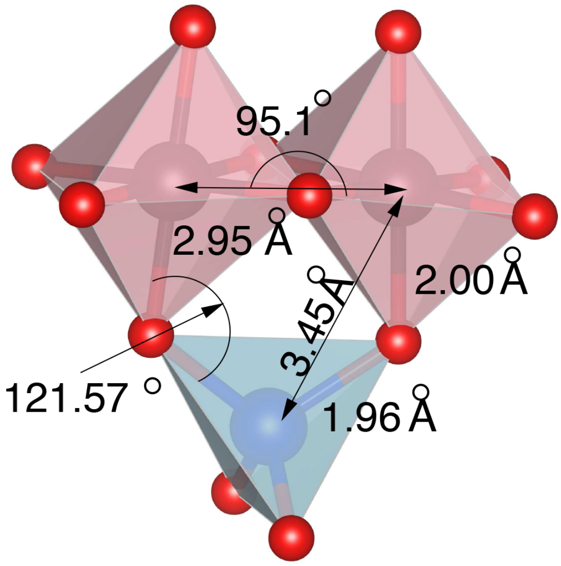

Fig. 5.1 A part of near neighbourhood of the tetrahedrally coordinated Co atom and octahedrally coordinated Cr atom in pristine $CoCr_2O_4$ is shown. Various bond angles and bond lengths are shown. The Co atoms are shaded blue, the Cr atoms pink and the O atoms red.

Upon substitution by Fe at tetrahedral site, the exchange and crystal field splitting of the parent atoms(Co_A and Cr_B) located in the far neighbourhood of the sites of substitutions remain much like the ones of the pristine compound. In the near neighbourhood of the substituted sites, the densities of states show traces of broken degeneracy. This must be the effect of structural distortion. Of particular interest in this context is the densities of states for the displaced Co atom (Co_B). The $d_{z^2} \uparrow$ level for this atom overlaps with the corresponding d_{z^2} level of the Fe atom at tetrahedral site . As a result the levels show splitting about the Fermi level. This indicates that the Fe_A-Co_B d_{z^2} orbitals hybridise to form molecular orbitals. It is interesting to note that the degeneracy in the e_g states present in the down (↓) spin channel of the pristine compound (due to T_d symmetry) is broken due to Fe substitution. This was already indicated by the increase in θ_{T_d}. The non-degenerate states, formed, overlap with the corresponding oxygen p states as expected. The exchange splitting at the tetrahedral sites for both e_g and t_{2g} levels increases due to Fe substitution as is seen from Table 5.1. This ensures that not more than one electronic state of the substituted atom is occupied in the minority spin channel. However the Co atom displaced to the octahedral site has a much lower exchange splitting resulting the Co_B to be in a low spin state. Inclusion of the electron-electron correlation through the Coulomb parameter U brings in drastic changes

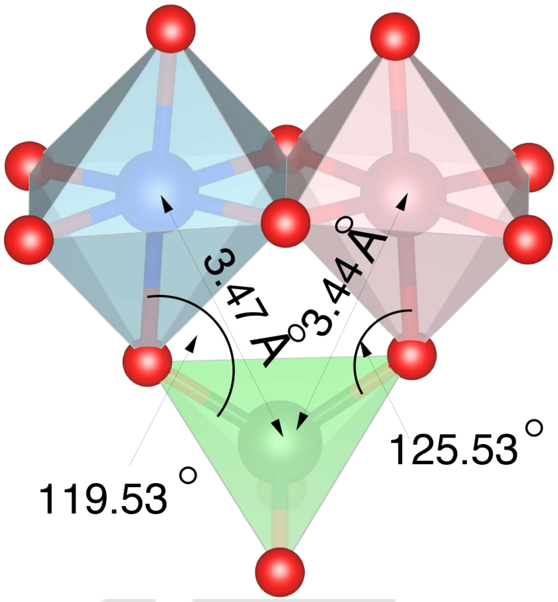

Fig. 5.2 A part of near neighbourhood of the tetrahedrally coordinated Fe atom and octahedrally coordinated Co atom are shown along with various bond angles and bond lengths for single Fe substituted at A site in $CoCr_2O_4$. The Co atoms are shaded blue, the Fe atoms green, the Cr atoms pink and the O atoms red

in the densities of states and subsequently in the exchange splitting. A high spin state of the displaced Co at Octahedral site emerges with a magnetic moment about 3 μ_B similar to the value at the original tetrahedral site. In Figure 5.3, we compare the densities of states of the pristine and the Fe substituted (at tetrahderal site) $CoCr_2O_4$ along with the atom projected densities of states. Upon Fe substitution, one can see significant changes in the densities of states (Figure 5.3 (top)). New peaks at 1 eV above Fermi level in the up (↑) band, at 0.45 eV, 0.65 eV, 6.8 eV and 7.4 eV below Fermi level in the down (↓) band appear. The inclusion of electron-electron correlation pushes the Co_B and Fe_A d_{z^2} states, which had formed molecular orbitals for $U = 0$ case to higher energies. These are the new states appearing in the up band at around 1 eV above Fermi level. This leads to the correct charge states of +2 and +3 for Co_B and Fe_A atoms respectively.

Single Fe substitution at the octahedral site reduces the total energy by an amount of about 400 meV per Fe atom in comparison to the total energy for Fe substitution at the tetrahedral site. Thus, for this low concentration of Fe substitution, the octahedral site substitution is preferred and the system is a normal spinel. This is in agreement with the experimental observation[142] that the inversion starts occurring for $x > 0.05$ (In our case x=0.03125). In this case too, all the magnetic components are in high spin states and the individual moments do not change from those in the case of substitution at tetrahedral site.

Table 5.1 Substituted site (A and B), Exchange Splitting of e_g and t_{2g} levels ($\Delta_{EX}^{e_g}$ and $\Delta_{EX}^{t_{2g}}$ respectively) and crystal Field splitting of up and down spin channels ($\Delta_{CF}^{\uparrow}$ and $\Delta_{CF}^{\downarrow}$ respectively) for different Species (first two rows are for pristine $CoCr_2O_4$, the next rows are for the substituted Fe_A and the Co_B atoms; the last row is for substituted Fe_B).

Site	Species	$\Delta_{EX}^{e_g}$ (eV)	$\Delta_{EX}^{t_{2g}}$ (eV)	$\Delta_{CF}^{\uparrow}$ (eV)	$\Delta_{CF}^{\downarrow}$ (eV)
A	Co	1.50	2.70	1.20	0.0
B	Cr	1.30	3.20	3.20	1.3
A	Fe	2.93	3.15	0.9	0.68
B	Co	0.57	0.3	1.33	1.6
B	Fe	2.85	3.55	2.5	1.8

In Figure 5.4, we show the structural distortions around the Fe sites and the relevant structural parameters along with the overall deviations from the octahedral symmetry due to single Fe substitution at an octahedral site. We find that the octahedron around Fe expands, the reason being the larger size of Fe^{3+} ions (ionic radius 0.785Å) than Cr^{3+} ions in the octahedral environment. The deviation from the octahedral symmetry is almost same as that in case of the pristine compound as is seen by comparing θ_{O_h} ($\sim 5.34^0$ for the pristine compound, while $\sim 5.27^0$ for Fe impurity site in the doped compound) in both cases. The Co_A-O-Fe_B and Fe_B-O-Cr_B angles remain almost at the values of the Co_A-O-Cr_B and Cr_B-O-Cr_B angles in pristine compound. Even the bond lengths change only slightly from those in the $CoCr_2O_4$. Thus we do not expect to see changes in the electronic structure as substantial (in comparison with $CoCr_2O_4$) as was observed in case of substitution at tetrahedral site.

The last row of Table 5.1 lists the crystal field splitting and exchange splitting for the substitution at octahedral site. Unlike Co substitution at octahedral site, substitution by Fe enhances the exchange splitting of e_g and t_{2g} levels. This ensures that not more than one electronic state of the substitute is occupied in the minority spin channel. Thus, it appears that the Fe spin state is unaffected by the symmetry of the site where it is substituted into. In the distant neighbourhood of Fe sites, the situations for Co atoms at tetrahedral site and Cr atoms at octahedral sites remain quite similar to that of the pristine $CoCr_2O_4$. In the nearest neighbourhood of Fe site, there are 6 octahedrally and 6 tetrahedrally coordinated sites. Both these sites show reduced symmetry due to Fe substitution and as a result there is a slight loss of degeneracy in the t_{2g} states.

Figure 5.5 shows the densities of states for a single Fe atom substituted at a octahedral site. It is observed that the inclusion of the electron-electron correlation affects the densities of states of Fe, with prominent effects on the t_{2g} states. The split $t_{2g}^{\downarrow}$ states near the

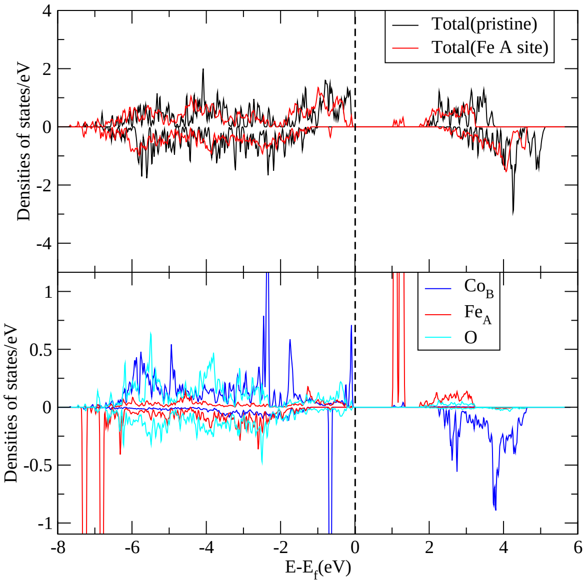

Fig. 5.3 (top) Total densities of states for pristine $CoCr_2O_4$ and for a single Fe substituted at tetrahedral site in $CoCr_2O_4$. (bottom) The atom projected densities of states for Fe_A, Co_B and oxygen atoms for single Fe substituted at tetrahedral site in $CoCr_2O_4$.

Fermi level are now pushed deeper into the conduction band while the $e_g^{\downarrow}$ states are unaffected. Similarly the $e_g^{\uparrow}$ states at -1.85 eV remain nearly unaffected. The electron electron correlation pushes the split $t_{2g}^{\uparrow}$ bands deeper into the valence band at -7.25 eV.

Thus, we see that the effects of Fe substitution at octahedral site is less dramatic than that at tetrahedral site. The impact of local structural distortion is more severe on the electronic structure of Fe substituted $CoCr_2O_4$ when Fe substitution takes place at tetrahedral sites. For the case of Fe substitution at tetrahedral site, the two Co atoms, having different symmetry associated with their sites, bring in additional dimensions to the impact of substitutions. It is, therefore, expected that the exchange interactions associated with the tetrahedral site and octahedral sites would be quite different depending upon the site of Fe substitution. This, in turn would affect the magnetic ground state of the system. In the next sections, we explore this aspect.

5.4 Patterns of site occupancies and their effects on the physical properties of $Co(Cr_{1-x}Fe_x)_2O_4$; 0.0625≤x≤0.75

The impurity calculations and subsequent analysis in the previous section clearly show that the substitution of Fe at the tetrahedral A sites would provide more substantial and possible interesting effects than a substitution at the octahedral B sites. In the following sub-sections

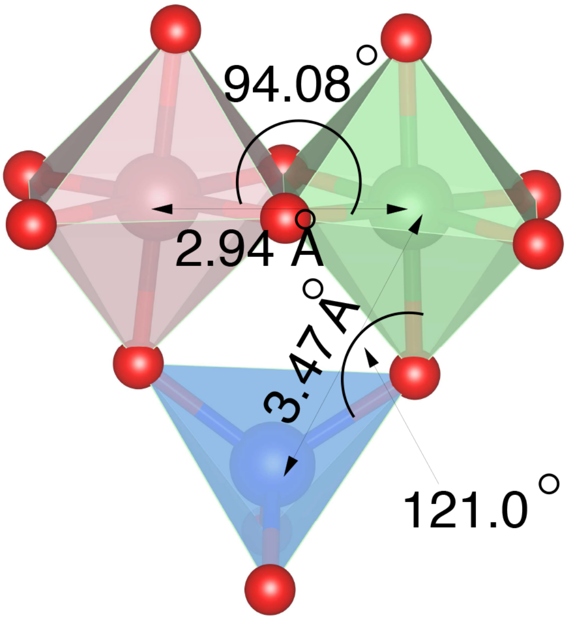

Fig. 5.4 A part of near neighbourhood of the octahedrally coordinated Fe atom is shown along with various bond angles and bond lengths for single Fe substituted at B site in $CoCr_2O_4$. The Co atoms are shaded blue, the Fe atoms green, the Cr atoms pink and the O atoms red.

we systematically study the site occupancy patterns of the magnetic cations and their effects on structural properties, electronic structures and magnetic interaction and provide a picture of the dependencies of the magnetic structure on compositions in $Co(Cr_{1-x}Fe_x)_2O_4$ in the composition range x=0.0625-0.75.

5.4.1 Temperature and concentration dependencies of degree of cation disorder y

In Fig. 5.6 we show the dependencies of the cation disorder energy E_c and the configurational free energy of cation disorder ΔF on y for different Fe concentration x, at a temperature 1500 K which is close to the annealing temperature of $1473-1573$ K reported in the experiment [142, 88]. Unlike Mn-substituted $CoCr_2O_4$, in this case, we find that the cation disorder is zero for smaller values of x only, if we do not consider the configurational entropy. When Fe substitution is 50%, the configurational energy is nearly identical for the "normal" and the complete "inverse" structures. For higher x values, the lowest energy state is the complete "inverse" one. Inclusion of the entropy term stabilises states with large values of y for all compositions. The results at 1500 K suggest that upto $x = 0.5$, y_0, the equilibrium value of y is nearly 0.5 for all x values, which means that nearly 50% of the substituted Fe

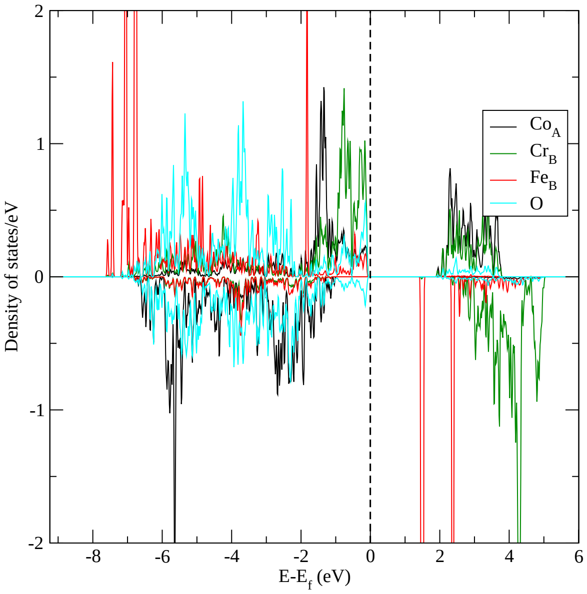

Fig. 5.5 Atom projected densities of states for a single Fe substituted at octahedral sublattice in $CoCr_2O_4$.

prefer to occupy the tetrahedral sites even when it's concentration in $CoCr_2O_4$ is small, thus making these systems close to a "half-inverse" configuration. For $x = 0.75$ and 1, the results suggest that at 1500K, the high Fe concentration compounds prefer to be nearly "complete inverse" as y_0 is close to 0.9 for these two compositions. The quantitative variations of y_0 with temperature T, shown in Fig. 5.7 shows this qualitative behaviour clearly. The results suggest that the cation disorder becomes more and more robust as the Fe concentration increases. For example, at $x = 0.5$, the degree of cation disorder, denoted by y_0 stays at 0.5 almost up to room temperature, while for lower values of x, y_0 varies substantially with temperature. For higher values of x, that is, when Fe concentration in the system is more than 50%, the system is nearly "complete inverse" for the entire temperature range. This result is in good agreement with the site occupancy patterns in this system, suggested by the experimentalists. The XRD and EXAFS experiments by Zhang. *et al* [142] suggested that except for $x = 0 - 0.05$, the substituted Fe atoms dominantly distribute themselves on the tetrahedral sites. They explained the phenomenon of magnetic compensation for $x = 0.05$ and the absence of it for higher x values based upon this site occupancy pattern of Fe.

5.4.2 Structural parameters and their variations with x and y

The anomalous change of slope in the variation of the lattice constant(a) with x obtained from the XRD pattern [142] of this system first led to the belief that there can be a significant

Table 5.2 Calculated cation-anion bond distances (in Å) in $Co\,(Cr_{1-x}Fe_x)_2\,O_4$ for different x and y values.

		A site		B site		
x	y	Co-O	Fe-O	Cr-O	Fe-O	Co-O
0	0	1.99	-	2.02	-	-
0.0625	0	1.99	-	2.02	2.04	-
	0.5	1.99	1.94	2.02	2.03	2.08
	1	1.99	1.92	2.02	-	2.08
0.125	0	1.98	-	2.02	2.03	-
	0.5	1.98	1.92	2.02	2.02	2.08
	1	1.99	1.93	2.01	-	2.09
0.25	0	1.98	-	2.02	2.03	-
	0.5	1.99	1.92	2.02	2.03	2.08
	1	1.98	1.93	2.01	-	2.08
0.5	0	1.98	-	2.02	2.04	-
	0.5	1.97	1.93	2.02	2.03	2.09
	1	-	1.92	2.01	-	2.08
0.75	0	1.98	-	2.03	2.04	-
	0.5	1.97	1.92	2.02	2.04	2.08
	1	-	1.90	2.01	2.03	2.08
1.0	0	1.98	-	-	2.05	-
	0.5	1.97	1.91	-	2.04	2.10
	1	-	1.91	-	2.04	2.08

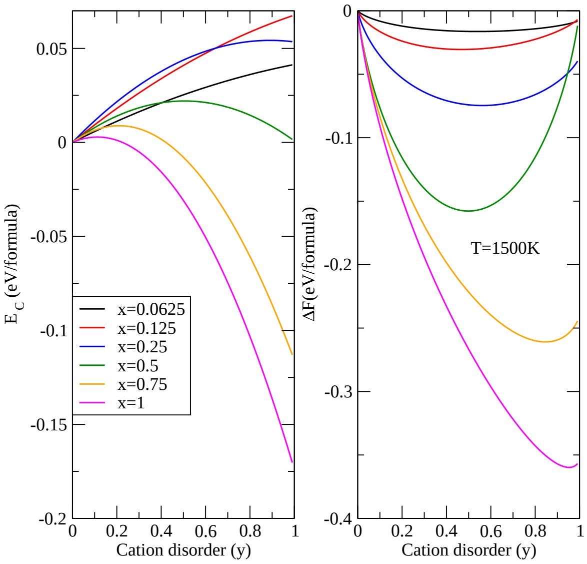

Fig. 5.6 Variations of the cation disorder energy(E_c) (left panel) and the configurational free energy (ΔF)(right panel) with degree of cation disorder y of $Co\,(Cr_{1-x}Fe_x)_2\,O_4$, for different values of x, the Mn concentration, at 1500 K, the annealing temperature of the experiment [143]. The equilibrium inversion parameter (y_0) at a given T and for a given x is obtained from the minima of ΔF.

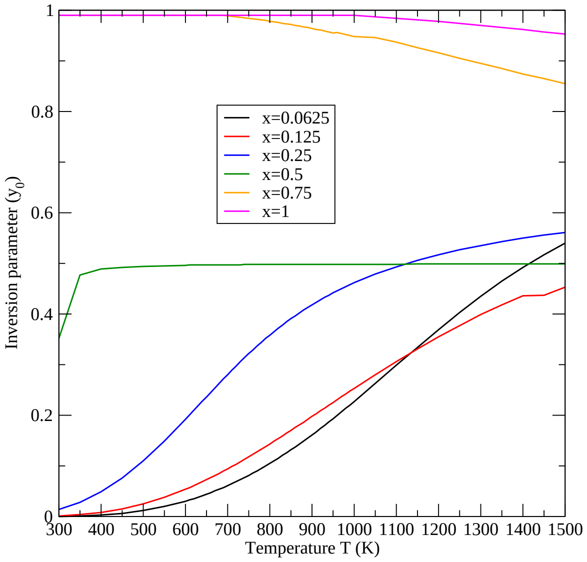

Fig. 5.7 Temperature dependence of the equilibrium inversion parameter (y_0) in $Co\,(Cr_{1-x}Fe_x)_2\,O_4$ for different x for the temperature ranging from room temperature to the annealing temperature of the experiment [143].

cation disorder in this system. The variations in the lattice constants for x upto 0.05, obtained from their XRD measurements, showed a very slow increase while for the range $x = 0.05 -$

Table 5.3 Calculated structural parameters of $Co\,(Cr_{1-x}Fe_x)_2\,O_4$ for different x and y values. The lattice constant a is in . u is the oxygen parameter.

x	y	a	u
0	0	8.430	0.262
0.0625	0	8.434	0.262
	0.5	8.432	0.262
	1	8.430	0.261
0.125	0	8.438	0.261
	0.5	8.433	0.260
	1	8.428	0.260
0.25	0	8.454	0.260
	0.5	8.437	0.260
	1	8.427	0.260
0.5	0	8.467	0.260
	0.5	8.452	0.258
	1	8.416	0.257
0.75	0	8.482	0.260
	0.5	8.453	0.258
	1	8.433	0.256
1	0	8.498	0.259
	0.5	8.468	0.257
	1	8.437	0.255

0.5, the increase in the lattice constant with x was rather rapid. The overall increase in the lattice constant is understandable for this system from the relative size of the cations in octahedral and tetrahedral crystal fields as discussed in section 5.2. Thus, if Fe ions mostly occupy the tetrahedral sites and the Co atoms the octahedral sites, the increase in the overall lattice constant would be rapid than if Fe had occupied the octahedral sites, replacing the Cr atoms. The lattice constants obtained from the other XRD study [88] by and large agreed with this explanation. However, they found that the rate of increase in the lattice constant slowed down for $x \geq 0.5$. They attributed this to the preferential occupation of octahedral B sites by the Fe atoms for higher Fe concentrations. Given these information from the experiments, we first discuss the variations in the structural parameters with concentration of Fe as well as with variations in the degree of cation disorder in order to understand the effects of Fe substitution on the structural parameters. In Table 5.2, we present various cation-anion bond distances at sites of different symmetries and their variations with x and y. In Table 5.3, we present the lattice constants a along with the oxygen parameter u for various x and y. The lattice constants and the cation-anion bond distances are obtained from the

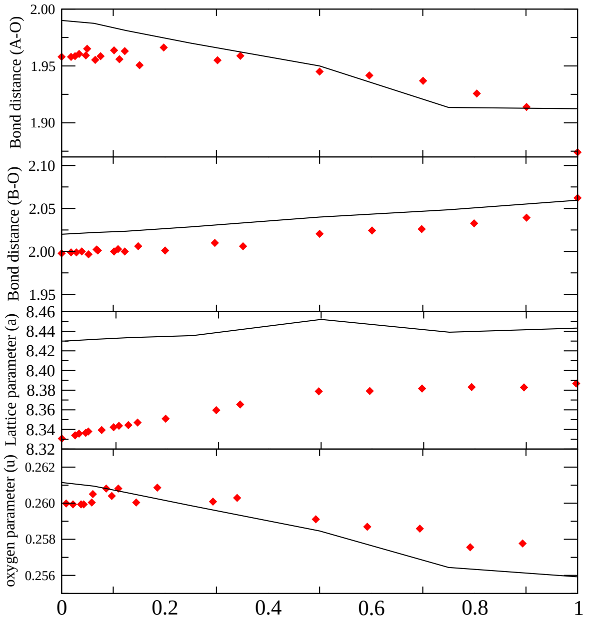

Fig. 5.8 The calculated cation-anion bond distances ($A-O$ and $B-O$ in), and the lattice parameters (a in and the oxygen parameter u) as a function of Fe concentration x for Co$(Cr_{1-x}Fe_x)_2$O$_4$. The Red diamonds are the experimental results [88] plotted for comparison.

DFT+U calculations. For these calculations, we have relaxed all the structural parameters and internal coordinates at each values of x and y. In Figure 5.8, we make a comparison between the experimental results [88] and the results obtained from our calculations for the average cation-anion bond distances at different sites, and the lattice parameters. The average cation-anion bond distances, for a given x, presented in figure 5.8, are obtained the following way: at a given value of y, the average cation-anion bond distance for a given site is obtained from the concentration averages of individual cation-anion bond distances. The value of y_0 for a particular x is already known from Figure 5.7. The average cation-anion bond distance for the given x is then obtained by interpolations of the average cation-anion bond distances for different y values. The oxygen parameter u, is then obtained using these average values. The lattice constant for a given x is also calculated in a similar way by interpolating the results for various y values presented in Table 5.3. From Figure 5.8, we see that the qualitative agreement between the experimental results and our calculated results are quite good for the cation-anion bond distances and the oxygen parameter u. The disagreements are mostly in the range of $0 < x < 0.0625$ where we do not have any results from our calculations. The significant disagreement between the experimental results and the calculated values, however, is observed for the lattice constant a. While the experimental results suggest an increase of about 0.05% as x varies from 0 to 1, our calculations are unable to capture this small change. In order to capture such small changes, one probably need to perform calculations for more values of y in order for the interpolation scheme used here to succeed. The changes in the average cation-anion bond distances with increasing Fe concentration can be explained from the results of Table 5.2. Results of Table 5.2 suggest that the average bond distance at the tetrahedral sites decrease in presence of cation disorder due to the presence of Fe^{3+} with the smallest ionic radii. Subsequent presence of Co^{2+} at the octahedral sites increase the average bond distances. These lead to a decrease(increase) of the $A-O(B-O)$ bond distances with x. It can be noted that the various cation-anion bond distances at various sites are quite insensitive to the degree of cation disorder so that the qualitative variations of the $A-O$ and $B-O$ with x can be explained purely as a composition effect. The variations in the lattice parameters with y, can be understood from the results of Table 5.2. The general trend seen in Table 5.3 is that with increase in y, the lattice constants decrease, particularly for $x \geq 0.5$. This can be understood from the compositions of the tetrahedral and octahedral sites for different y and x and the variations in their bond distances (Table 5.2). For smaller x values, the equilibrium value of y is around 0.5. As a result, the percentages of Fe at tetrahedral site and Co at octahedral site are not too significant and the lattice parameter a, in particular is not affected by the changes in the degree of cation disorder. For $x \geq 0.5$, $y_0 \geq 0.5$, and thus the $A-O$ bonds shorten considerably on an average effecting an overall decrease in the lattice parameters.

5.4.3 Magnetic exchange interactions and their dependencies on x and y

We now proceed to discuss how the Fe substitution in $CoCr_2O_4$ leads to a collinear magnetic structure. We are particularly interested in the evolution of the exchange interactions between different sites and different atoms as the composition of the system changes along with the degree of cation disorder. As discussed in the previous chapters, we are interested in the results of the nearest neighbour exchange interactions only, and these are calculated by mapping the DFT+U total energies on a Heisenberg Hamiltonian. Due to the requirement of prohibitively large resources for calculations of all exchange interactions, particularly for $y = 0.5$ and $y = 1$, we could compute certain exchange parameters only for a limited number of compositions. In spite of these limitations, the required trends to understand the evolution of the magnetic structure can be understood from the computed results as discussed in the following. In Reference [40], evolution of the exchange interactions were computed by the Lichtenstein formulation [68] within the framework of KKR-CPA Green's function method [33] which is free of the above mentioned limitations. However, the shortcoming of the

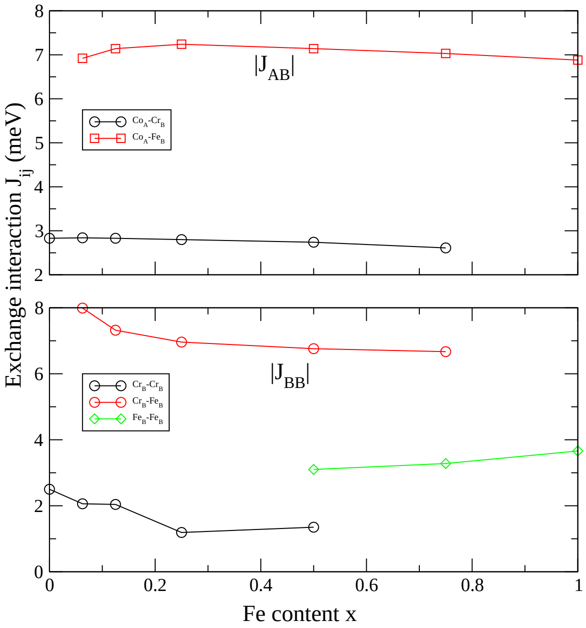

Fig. 5.9 The absolute values of different magnetic exchange parameters calculated in the present work as a function of Fe concentration x in Co$(Cr_{1-x}Fe_x)_2$O$_4$. The B-B exchange interactions(in meV) are indicated by $|J_{BB}|$, while the A-B exchange interactions(in meV) are indicated by $|J_{AB}|$. The results are for the "normal" spinel structure, that is, for $y = 0$.

KKR-CPA method is in their inability to treat the relaxations around atomic sites leading to local distortions and dispersions in bond distances. As a result, in Reference [40], calculations could be done only for low values of $x (0 \leq x \leq 0.1)$. The calculations with "normal" and "complete inverse" configurations showed that although there is a competition between the exchange interactions between the tetrahedral and the octahedral sites (J_{AB}) and the ones between octahedral and octahedral sites (J_{BB}). With increase in Fe content, the J_{AB}s increase rapidly while the J_{BB}s either decrease or increase slowly, indicating that J_{AB}s may superseed J_{BB}s with higher Fe content. In Figures 5.9, 5.10 and 5.11, we present our calculated values of different J_{ij} as a function of Fe content x for three different degrees of cation disorder. The results suggest that in case of Fe substitution at octahedral sites, the "normal spinel" configuration ($y = 0$), there is a competition between the exchange parameters associated with Co$_A$-Fe$_B$ and Cr$_B$-Fe$_B$ pairs. Across the composition range, these two are the dominant interactions. At low values of x, the Cr$_B$-Fe$_B$ interaction is slightly dominant but the Co$_A$-Fe$_B$ interactions catch up as Fe concentration in the system increases. The Cr$_B$-Cr$_B$ and Co$_A$-Cr$_B$ interactions are relatively weak and slowly change with composition. Since the Fe atoms would like to distribute themselves homogeneously in the system [40], Fe does not have another Fe as it's nearest neighbour until the concentration of Fe in the system is

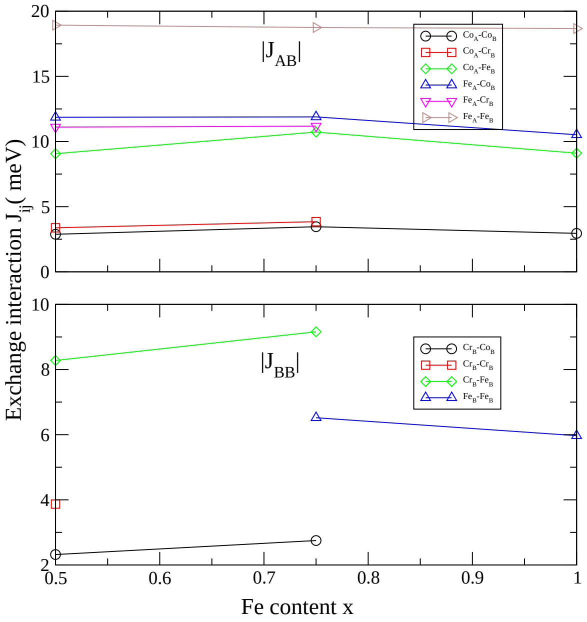

Fig. 5.10 The absolute values of different magnetic exchange parameters calculated in the present work as a function of Fe concentration x in Co$(Cr_{1-x}Fe_x)_2$O$_4$. The B-B exchange interactions(in meV) are indicated by $|J_{BB}|$, while the A-B exchange interactions(in meV) are indicated by $|J_{AB}|$. The results are for the "half-inverse" spinel structure, that is, for $y = 0.5$.

significant. This is demonstrated by the emergence of the Fe-Fe exchange parameter only at $x = 0.5$. The strength of this interaction lies in between that of the dominant Cr$_B$-Fe$_B$ and weaker Cr$_B$-Cr$_B$ interactions, and would add to the strength of the total J$_{BB}$, thus competing closely with total J$_{AB}$ interactions. Therefore, with the "normal" configuration, one would not achieve a collinear magnetic structure in this system. In Figs. 5.7 and 5.8 we observe the effects of the cation disorder on the relative strengths of the exchange interactions. In the "half-inverse" configuration ($y = 0.5$), the A-B interactions overwhelmingly dominate over the B-B interactions for $0.5 \leq x \leq 1$. It may be noted that modeling of a "half-inverse" structure for $x < 0.5$ would have required larger unit cells and hence we refrained from modeling the "inverse" structures for smaller x values. This would not pose any serious problem as we are interested only to find the trends in different exchange interactions when the state of cation disorder changes, in order to understand the origin of the emergence of the collinear structure at one end. Analysing Fig. 5.10, we further see that the dominant A-B interaction for $y = 0.5$ comes from the Fe atoms at crystallographic sites of different symmetry. The three other dominant A-B exchange interactions Co$_A$-Fe$_B$, Fe$_A$-Co$_B$ and Fe$_A$-Cr$_B$ compete with each other. On the other hand, the dominant B-B interaction is between Fe and Cr

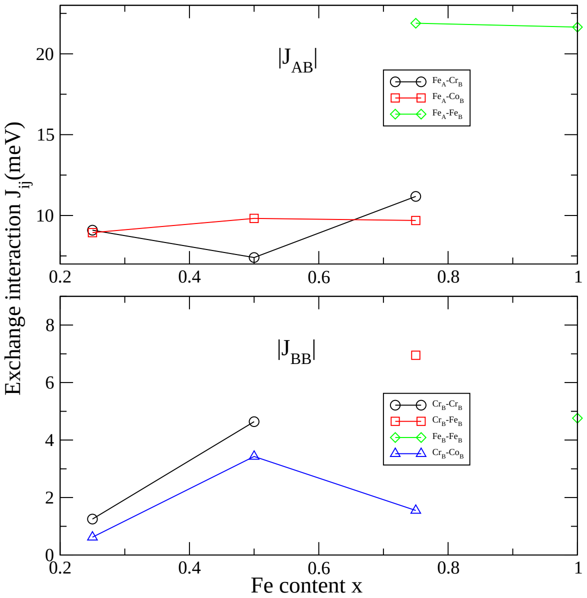

Fig. 5.11 The absolute values of different magnetic exchange parameters calculated in the present work as a function of Fe concentration x in Co$(Cr_{1-x}Fe_x)_2$O$_4$. The B-B exchange interactions(in meV) are indicated by $|J_{BB}|$, while the A-B exchange interactions(in meV) are indicated by $|J_{AB}|$. The results are for the "complete inverse" spinel structure, that is, for $y = 1$

atoms at octahedral sites as was the case for $y = 0$. The picture remains same for $y = 1$, that is, for "complete inverse" configuration. Thus, it can be concluded that in Co$(Cr_{1-x}Fe_x)_2$O$_4$, a collinear magnetic structure would emerge due to the cation disorder among tetrahedral and octahedral sites, and would certainly be achieved when Fe composition would reach 50%.

The question now remains as to why a particular magnetic exchange parameter dominates over the others and how that changes with changes in the degree of cationic disorder. In the next subsection, we address this question by analysing the electronic structures as a function of composition and degree of cation disorder.

5.4.4 Electronic structures and their variations with x and y

We present results on the electronic structures with variations in x for three degrees of cation disorder represented by $y = 0$, 0.5 and 1 in Figures 5.12, 5.13 and 5.14 respectively. Quite interestingly, the qualitative features in the atom-projected densities of states remain absolutely same irrespective of x and y. A careful look at the figures suggest the following:

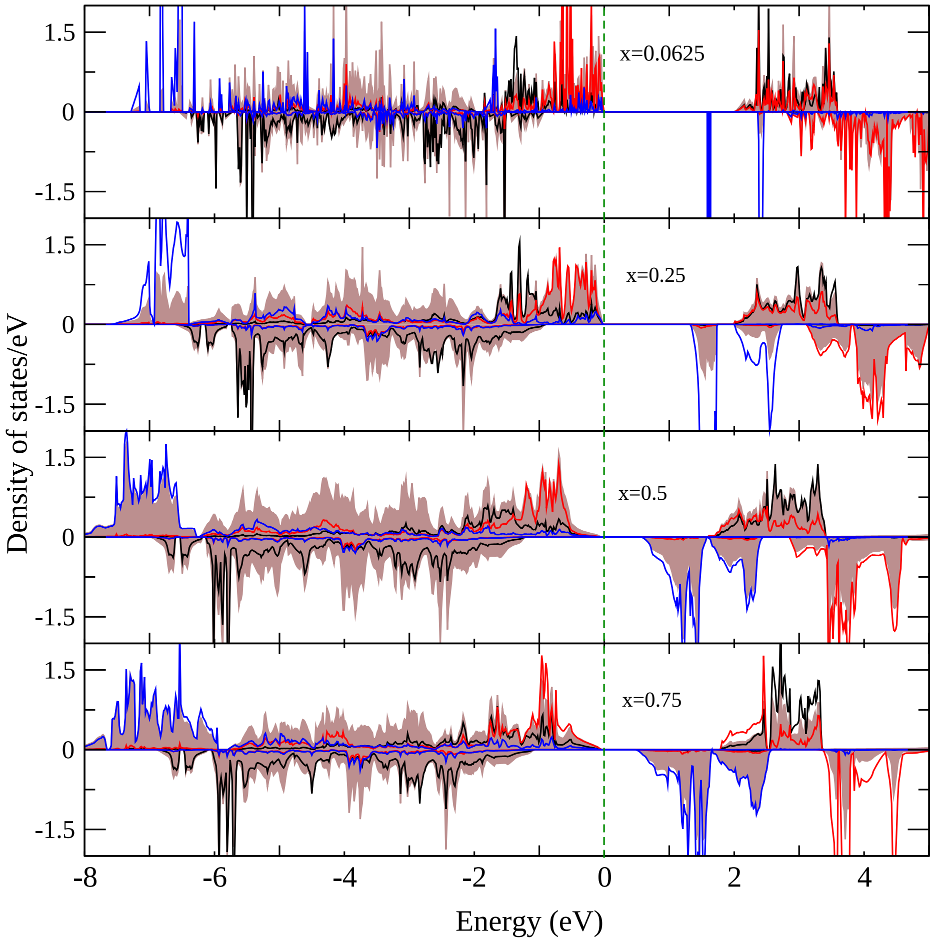

Fig. 5.12 Total and atom-projected densities of states of $Co\,(Cr_{1-x}Fe_x)_2\,O_4$ for different x. The results are for zero cation disorder ($y = 0$). The results for $CoCr_2O_4$ ($x = 0$) are also included. Here the total densities of states is denoted by brown shade. The black, red and blue curves represent atom projected densities of states of Co at tetrahderal sites, Cr and Fe at octahedral sites, respectively.

for any x and y, Co_A t_{2g} states are half-filled and the e_g states are completely filled, Cr t_{2g} states are half-filled while e_g states are completely empty, Fe states at both tetrahedral and octahedral sites have both t_{2g} and e_g states half-filled while Co_B t_{2g} states are more than half-filled and the e_g states are half-filled. Thus, the band filling associated with the atoms resemble that of pure $CoCr_2O_4$ and $CoFe_2O_4$ [26]. Such robustness of the electronic structures originates from strong and comparable crystal fields associated with the magnetic cations as was seen in cases of pure $CoCr_2O_4$ and $CoFe_2O_4$ [26]. The positions of the major peaks associated with each individual atoms also do not change considerably with changes

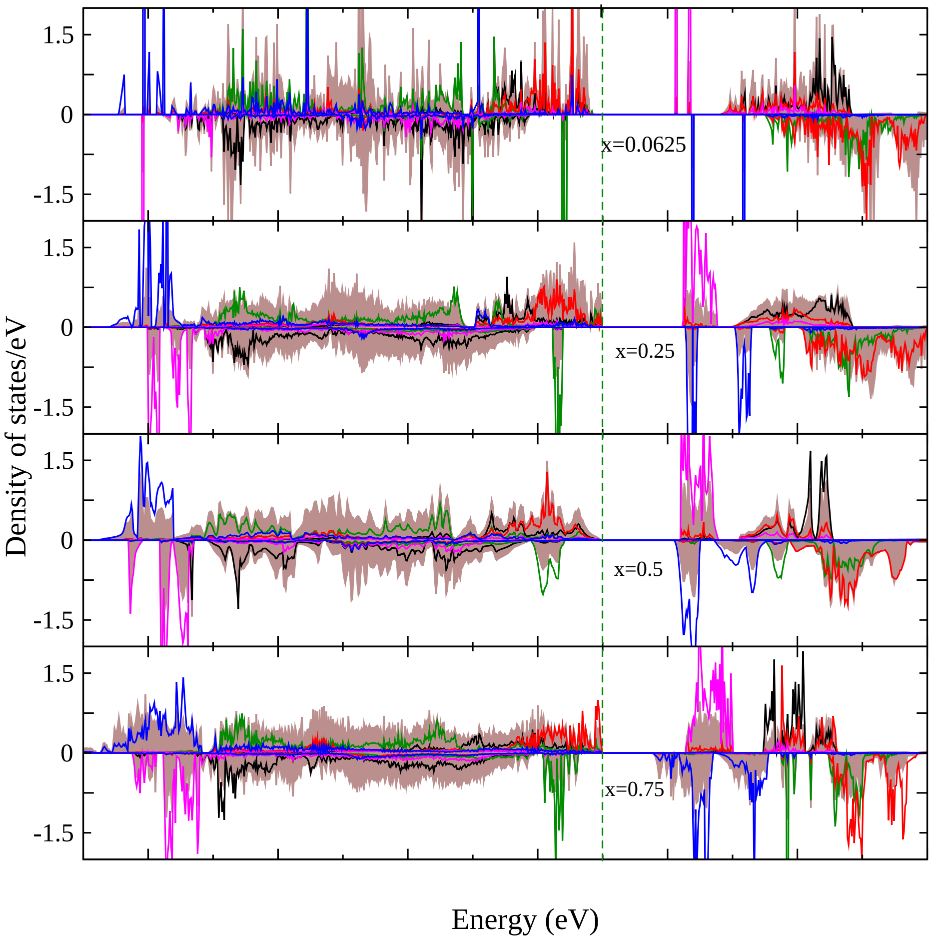

Fig. 5.13 Total and atom-projected densities of states of $Co\left(Cr_{1-x}Fe_x\right)_2O_4$ for different x. The results are for 50% cation disorder ($y = 0.5$).Here the total densities of states is denoted by brown shade. The black and the green curves represent atom projected densities of states for Co at tetrahedral and at octahedral sites respectively, the red curve represents atom projected densities of states for Cr, the pink and the blue curves represent atom projected densities of states for Fe atoms at tetrahedral and at octahedral sites respectively.

in x and y. The only change that one can see is the re-distributions of the weights associated with a particular atom type when x changes, keeping y fixed.

The features in the densities of states can now be conveniently used to explain the trends in the magnetic exchange interactions. For $y = 0$, the results presented in Fig. 5.9 show that Co$_A$-Fe$_B$ exchange interaction closely compete with Cr$_B$-Fe$_B$ one. Since Co$_A$ and Fe$_B$ have half-filled t$_{2g}$ and e$_g$ states respectively, this interaction is strongly antiferromagnetic [135]. On the other hand, both Cr$_B$ and Fe$_B$ t$_{2g}$ orbitals are half-filled. Direct interaction between them is possible which strengthens the overall B-B interaction [135]. As a result,

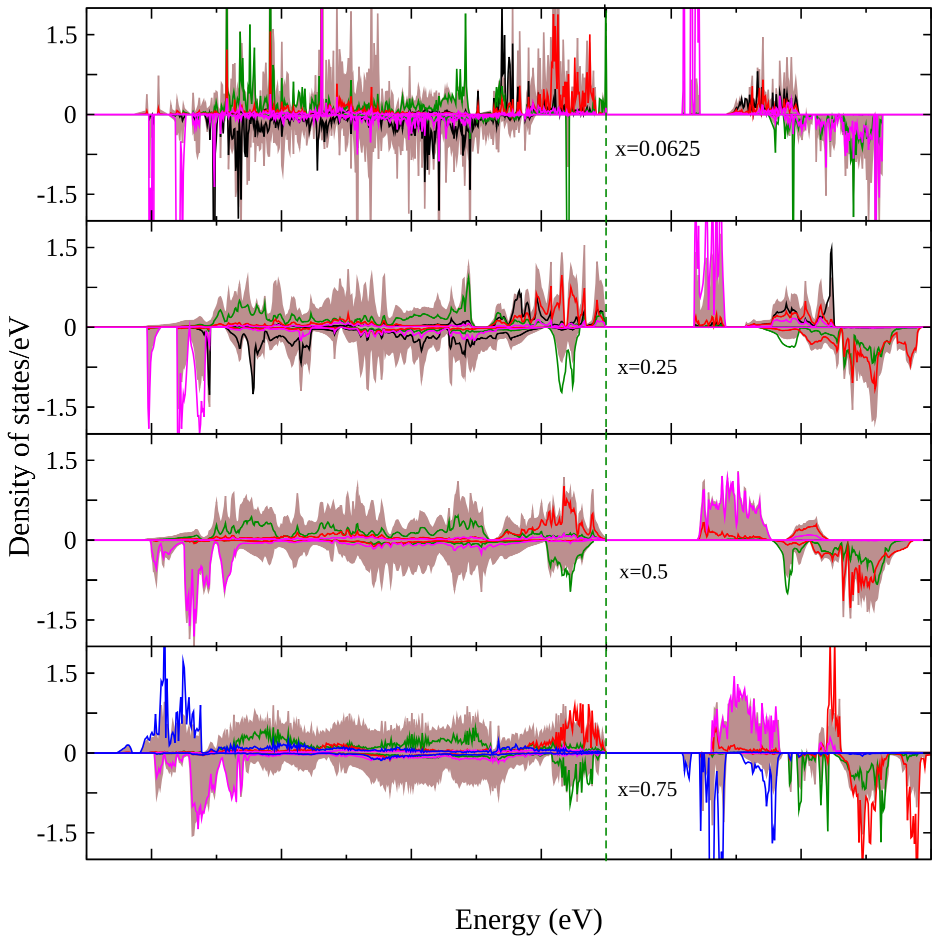

Fig. 5.14 Total and atom-projected densities of states of $Co\,(Cr_{1-x}Fe_x)_2\,O_4$ for different x. The results are for full inverse arrangement ($y = 1$).Here the total densities of states is denoted by brown shade. The black and the green curves represent atom projected densities of states for Co at tetrahedral and at octahedral sites respectively, the red curve represents atom projected densities of states for Cr, the pink and the blue curves represent atom projected densities of states for Fe atoms at tetrahedral and at octahedral sites respectively.

there is close competition between J_{AB} and J_{BB} exchange interactions for $y = 0$. The strength of the dominant J_{BB} however is weaker in comparison to the dominant J_{AB} due to the fact that the inter-cation distance at the octahedral site is larger than that at the tetrahedral site as can be understood from the bond distances presented in Table 5.2. For $y = 0.5, 1$, the overwhelmingly dominant A-B interaction is due to the Fe atoms at the tetrahedral and the octahedral sites. In this case, both tetrahedral site t_{2g} and octahedral site e_g orbitals are half-filled making the interaction strongly antiferromagnetic. The relatively much weaker B-B interaction, mostly coming from Cr-Fe pairs are due to the fact that due to inversion, the

Fe content at octahedral site decreases in comparison to the $y = 0$ case, thus, increasing the cation-cation distances at the octahedral site. The other prominent A-B interactions for $y = 0.5, 1$ are due to Fe$_A$-Co$_B$ and Fe$_A$-Cr$_B$ pairs. In case of the former, although the tetrahedral site t$_{2g}$ and octahedral site e$_g$ are half-filled, and thus the exchange interaction should be strongly antiferromagnetic, they are weaker in comparison to the Fe-Fe interactions. This is due to the fact that Fe$_A$-Co$_B$ distances are larger than the Fe$_A$-Fe$_B$ distances (Table 5.2). In case of Fe$_A$-Cr$_B$ pair, the empty e$_g$ orbitals at the Cr sites make the interactions relatively weak [135].

5.5 Summary and Conclusions

Using density functional theory based calculations, our results show that the substitution of Fe at the tetrahedral sites gives rise to Co at both tetrahedral and octahedral sites, which behave very differently and produce significant effects on the structural parameters. The substantial deviation from the tetrahedral symmetry results in loss of degeneracy of the *d* orbitals of Fe and Co atoms occupying octahedral sites resulting in a lowering of the magnetic exchange splitting of Co atoms at octahedral positions. The inclusion of the electron electron correlation enhances the magnetic exchange splitting, thus affecting the spin states of the transition metal cations. Substitution of Fe at the octahedral site, on the other hand, does not produce such interesting effects, and the loss of symmetry of the *d* orbitals as a result of local structural distortion is minimal. Although at very low values of x, the substitution of Fe at octahedral sites are energetically preferable, a tendency towards "inversion" is clearly observed with increasing x, in confirmation with experiments. We have explored the effects of cation disorder on the structural and magnetic properties of Co$(Cr_{1-x}Fe_x)_2$O$_4$ by computing the "inversion parameter" at each value of x from a combination of DFT based total energy calculations and a thermodynamic model. In agreement with the inferences from the experimental results on structural, magnetic and thermal properties of this system, we find that for all compositions, Fe has a strong preference for the tetrahedral (A) sites in the spinel structure. We have explicitly calculated the structural parameters as a function of the degree of inversion and the composition. The qualitative trends in our results agree very well with the experimentally observed ones. The major highlight of this work is that we have provided an explanation to the emergence of a collinear spin structure from a non-collinear one as the Fe substitution in the system increases gradually. We have conclusively shown that the degree of cation disorder is the deciding factor for the emergence of a collinear magnetic order in this system. The trends in the magnetic exchange interactions have been explained from the features in the electronic structures. In comparison to Mn substituted CoCr$_2$O$_4$, the features in the electronic structures of Fe substituted $CoCr_2O_4$ are far more robust against changes in the composition and the degree of cation disorder. This can be understood from the relatively strong and comparable crystal fields associated with the cations at different sites of the end compounds. This work, therefore, stands out as the first comprehensive investigations into the fundamentals of the Fe substituted $CoCr_2O_4$ for a larger composition regime than what has been available so far.

Chapter 6

Vibrational properties of pristine and substituted $CoCr_2O_4$

6.1 Introduction

The chromite spinel AB_2O_4, A being a cation with charge state +2, have shown intimate coupling between their structural and magnetic properties. For example, in some of these compounds, significant magnetoelastic coupling is found to take place near the magnetic phase transitions, accompanied with structural transition [141, 13, 97]. An efficient way to unravel the magneto-structural effects is the study of the lattice vibrations. Optical probe of lattice vibrations has come out to be an useful tool to understand the extent of coupling between spin and lattice degrees of freedom for a broad class of chromites[66, 116, 97, 55]

The complex magnetic phase diagram of $CoCr_2O_4$ had drown attention to the researchers to explore its lattice dynamical properties after the multiferrocity was discovered in this material. In past five years, there have been few attempts to explore the extent of interactions between magnetic and structural degrees of freedom in this material [126, 55, 94, 35]. Using submillimeter Infra-red (IR) fourier spectroscopy, Torgashev etal [126] suggested that the magnetic transition to the multiferroic state (T<26K) is accompanied by a loss of symmetry of the lattice. From an analysis of the optical conductivity spectra, Kocsis et al [55] observed an anomalous broadening of some of the IR active modes near paramagnetic-ferrimagnetic transition. Ptak et al [94] observed anomalous frequency shifts of the IR modes near ferrimagnetic transition. Their analysis pointed that spin-lattice coupling, abbeit weak, is the reason behind such anomalous behavior of the IR modes to spin-lattice coupling, albeit weak. Efthimiopoulos et al [35] in a very recent Raman spectroscopy study of $CoCr_2O4$ under pressure observed significant frequency shifts of the Raman modes associated with a structural transition. They attributed this to the renormalisations of the magnetic exchange interactions under the influence of the external pressure. IR and Raman spectra of $CoCr_{1.5}Fe_{0.5}O_4$[95] shows anomalous shifts in frequencies near the ferrimagnetic transition which was again attributed to the spin-lattice coupling. The above observations show that the lattice dynamics of pristine and substituted $CoCr_2O_4$ can be quite interesting and thus warrant a detailed investigation with ab-initio calculations. In this chapter, we therefore, have computed the phonon dispersion relations and the vibrational densities of states of $CoCr_2O_4$ and Fe, Mn substituted $CoCr_2O_4$ for select compositions. we have focused on two different aspects of lattice dynamics.

(i) Understanding of the effects of cation disorder on the lattice dynamics: the motivation is to understand the differences in the correlated vibrations of various specie pairs due to the changes in the site occupancies.

(ii) Understanding of the spin-phonon couplings: the motivation is to be able to quantify the strengths of spin-phonon coupling associated with each vibrational mode and each specie pair. The formulation to quantify the spin-phonon coupling has been done only for AB_2O_4 spinels where only B is magnetic cation[61] . We have generalized the formulation for cases where both A ans B are magnetic ions. The generalization to more than two magnetic cations and with substitutional disorder is straight forward in principle, but difficult from the point of view of implementation. Thus we have quantified the spin-phonon couplings strengths for $CoCr_2O_4$ only. This work, the first ever *ab initio* computations of lattice dynamics, in these systems provide enough information about the vibrational properties, for further in-depth investigations, both experimentally and computationally.

6.2 Computational details

We have used the small displacement method as implemented in the PHON [1] code for computing the dynamical matrices, diagonalisation of which would provide the normal modes of lattice vibrations. A small displacement of 0.04 Åon the atoms in a 2×2×2 supercell of the 14 atom unit cell is used for computations of forces by the DFT+U method. The various parameters used in DFT+U method have been kept the same as those mentioned in previous chapters.

6.3 Results and Details

6.3.1 Symmetry of the lattice and the vibrational modes

Before presenting the results on our calculations, we discuss the changes in the symmetries of the spinel lattice due to different degrees of cation disorder and the resulting optical modes in standard group theory notations. The space groups corresponding to AB_2O_4 and $A(B_{0.5}C_{0.5})_2O_4$ for different y (degree of cation disorder) values are presented in Table 6.1. The optical modes associated with each symmetry and their characteristics (whether Infra-red active, Raman active or inactive) are presented in Table 6.2

Table 6.1 The space group associated with the compound $A(B_{1-x}C_x)_2O_4$ under different degrees of cation disorder y

system	y	space group symbol	space group no.
AB_2O_4	0.0	$Fd\bar{3}m$	227
	0.5	$R3m$	160
	1.0	$Imma$	74
$A(B_{0.5}C_{0.5})_2O_4$	0.0	$Imma$	74
	0.5	Cm	8
	1.0	$Imma$	74

Table 6.2 Crystal structures of different symmetries and the group theory representation of the corresponding optical modes for $A(B_{1-x}C_x)_2O_4$ compounds. Whether a mode is IR active, Raman active or inactive are mentioned in parantheses next to its group theory representation. IR stands for Infra-red active, R stands for Raman active and I stands for inactive modes.

space group	$Fd\bar{3}m$(227)(m-3m)	$R3m$ (160)(3m)	$Imma$(74)(mm.m)	Cm (8) (m)
Vibrational modes	$T_{1u}(IR)$	$A_1(R,IR)+E(R,IR)$	$B_{1u}(IR)+B_{2u}(IR)+B_{3u}(IR)$	$2A'(R,IR)+A''(R,IR)$
	$T_{2u}(I)$	$A_2(I)+E(R,IR)$	$A_u(I)+B_{2u}(IR)+B_{3u}(IR)$	$2A'(R,IR)+A''(R,IR)$
	$T_{1g}(I)$	$A_2(I)+E(R,IR)$	$B_{1g}(R)+B_{2g}(R)+B_{3g}(R)$	$A'+2A''$
	$T_{2g}(R)$	$A_1(R,IR)+E(R,IR)$	$A_g(R)+B_{2g}(R)+B_{3g}(R)$	$A'(R,IR)+2A''(R,IR)$
	$E_u(I)$	$E(R,IR)$	$A_u(I)+B_{1u}(IR)$	$2A''$
	$E_g(R)$	$E(R,IR)$	$A_g(R)+B_{1g}(R)$	$2A'(R,IR)$
	$A_{2u}(I)$	$A_1(R,IR)$	$B_{1u}(IR)$	$A''(R,IR)$
	$A_{1g}(R)$	$A_1(R,IR)$	$A_g(IR)$	$A'(R,IR)$

For AB_2O_4 compounds in $Fd\bar{3}m$ space group, there are 16 optical modes at the center of the Brillouin zone that is at Γ point: $4T_{1u}(IR) \oplus 2T_{2u}(I) \oplus 3T_{2g}(R) \oplus T_{1g}(I) \oplus 2A_{2u}(I) \oplus$

$A_{1g}(R) \oplus 2E_u(I) \oplus E_g(R)$; each T_{1u}, T_{2u}, T_{1g} modes is triply degenerate, each E_u and E_g modes is doubly degenerate while A_{1g}, A_{2u} are non-degenerate. Upon half-inversion", the symmetry of the lattice is reduced (space group R3m) to a trigonal one leading to splitting of T_{2u} and T_{1g} modes into a E doublet and a A_2 singlet. “Full-inversion” further reduces the symmetry to orthorhmbic which lifts the degeneracies completely . With substitution in the B sublattice, the symmetry of the original cubic lattice is reduced. For $A(B_{0.5}C_{0.5})_2O_4$ compounds, “normal spinel” configuration itself gives rise to the orthogonal *Imma* symmetry, and thus the degeneracies are completely lifted. With “half-inversion”, the symmetry is monoclinic while the orthogonal *Imma* symmetry is retained with “full-inversion”. However, the characteristics of the modes change with the changes in the crystal symmetry.

6.3.2 Dispersion relations and vibrational densities of states for $CoCr_2O_4$, $Co(Cr_{1-x}Mn_x)_2O_4$ and $Co(Cr_{1-x}Fe_x)_2O_4$ as a function of y, the degree of cation disorder

In Table 6.3, we show a comparison between optical modes for $CoCr_2O_4$ obtained in present calculations and those obtained in experiments. Our results agree very well with the experiments for the Infra-red and Raman active modes in the low and mid-frequency regions. For higher frequencies, our results are systematically underestimated. Nevertheless, the overall agreement between the first-principles calculations and the experiments are decent. The dispersion relations for (0 q q) and (q q q) directions in Brillouin zone and the vibrational densities of states (total and atom projected) are shown in Figure 6.1(a-(i)) and Figure 6.1(d-(i)) respectively. The lattice dynamics of “normal spinel” $CoCr_2O_4$ is governed by Co_A modes at low frequencies, oxygen modes at high frequencies and Cr_B modes at the intermediate frequencies. This is consistent with the fact that Co_A is having the highest mass while oxygen is having the lowest mass. An analysis of the inter-atomic force constants show that the Cr_B-O bonds are much stronger than the Co_A-O bonds. Thus, inspite of the inter-atomic distances being comparable(Figure 5.1), the vibrations of Cr octahedra are mostly in the higher frequency part of the spectrum while vibrations of Co tetrahedra are confined in the lower frequency part of the spectrum.

In Figs 6.1(a-(ii)) and 6.1(d-(ii)), we show the dispersion curves of $CoCr_2O_4$ with y=0.5, that is, in the “half-inverted” structure. The lowering of symmetry due to the “inversion” now lifts the degeneracy partially and gives rise to new modes as was discussed in the previous sub-section. The inspection of the atom-projected vibrational densities of states reveals quite complex admixture of contributions from atoms at various symmetry positions. Due to reduction of symmetry, the largest Co_A peak for y=0 now splits into two neighboring

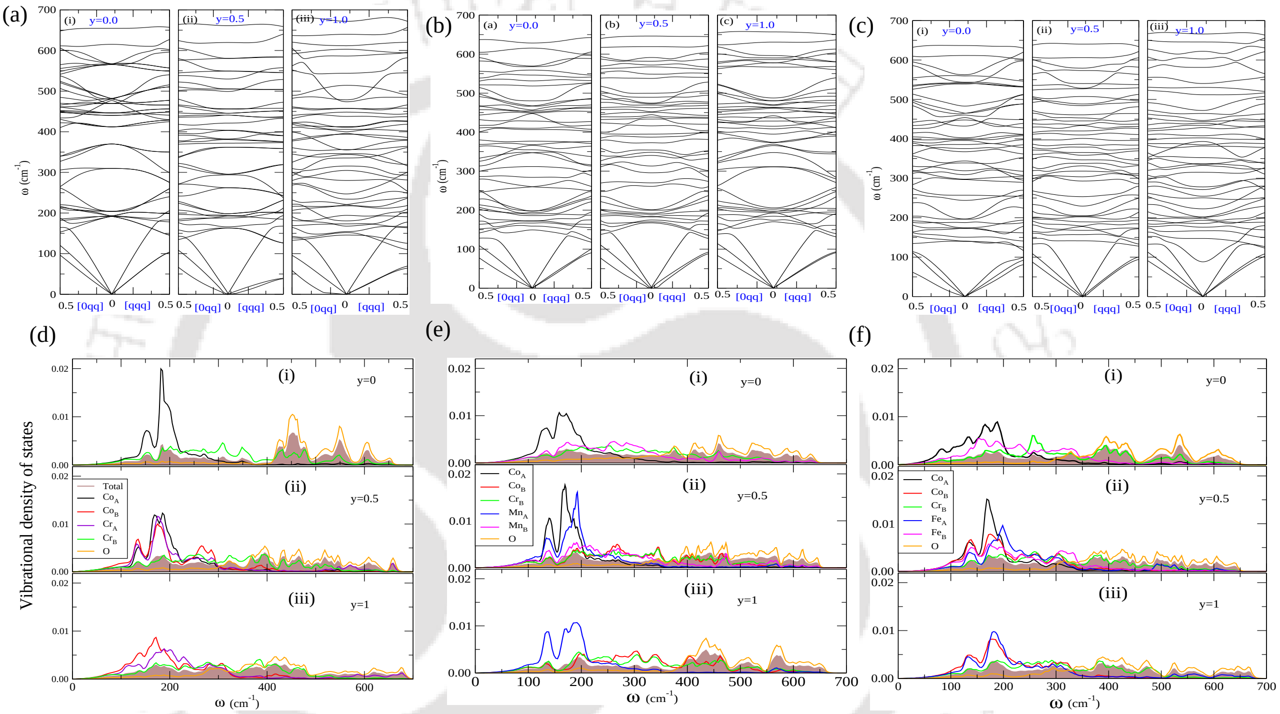

Fig. 6.1 (a)-(c) show the phonon dispersion relations for $CoCr_2O_4$, $CoCrMnO_4$ and $CoCrFeO_4$ respectively. In each of (a)-(c), (i), (ii) and (iii) stand for degree of cation disorder y=0, 0.5 and 1 respectively. (d)-(f) shows the total and atom projected vibrational densities of states for $CoCr_2O_4$, $CoCrMnO_4$ and $CoCrFeO_4$ respectively. In each of (d)-(f), (i), (ii), (iii) stand for degree of cation disorder y=0, 0.5, 1 respectively.

Table 6.3 Optical modes of $CoCr_2O_4$ at Γ point obtained in present calculation are listed along with the corresponding experimental frequencies. Here R, IR and I are Raman, Infrared and Inactive modes respectively.

Mode	Type	Freq.(cm^{-1}) Cal. (present calculation)	Freq. (cm^{-1}) (Experiment)
$T_{2u}^{(1)}$	I	191	
$T_{2g}^{(1)}$	R	195	196[71], 196[94],195[35]
$T_{1u}^{(1)}$	IR	204	196[71],200[55], 204[81]
$E_{u}^{(1)}$	I	310	
$T_{1u}^{(2)}$	IR	371	374[71],382[55], 384[81]
T_{1g}	I	406	
E_{g}	R	433	450[94],452[35]
$T_{2u}^{(2)}$	I	447	
$T_{1u}^{(3)}$	IR	466	484[71],487[55],532[81]
$A_{2u}^{(1)}$	I	470	
$T_{2g}^{(2)}$	R	471	516[71],515[94],516[35]
$E_{u}^{(2)}$	I	480	
$T_{1u}^{(4)}$	IR	562	619[71], 610[55],635[81]
$T_{2g}^{(3)}$	R	565	603[94],605[35]
$A_{2u}^{(2)}$	I	615	
A_{1g}	R	650	687[71],685[94],687[35]

peaks. There is now significant contributions from Co_B and Cr_A atoms towards the low frequency modes. In fact, their contributions extend upto the middle part of the spectrum. An oxygen peak now appears at around 400cm^{-1}. Analysis of the force constants shows that while presence of Cr_A atoms make Cr_A-O bonds stronger, thus, increasing the overall strengths of the A-O bonds, the presence of Co_B atoms weaken the overall strengths of the B-O bonds. Thus there is a competition between the bond strengths associated with the tetrahedra and octahedra and as a result the low to medium frequency parts of the spectrum have contributions from almost all the atoms. In Figs 6.1 (a-(iii)) and Figs 6.1 (d-(iii)), we shows the dispersion curves and vibrational densities of states of $CoCr_2O_4$ with y=1, that is, in "full inverted" structure. The dispersion relation shows the effects of further lowering of the symmetry of the crystal as the middle part of the spectrum (300-400cm^{-1}) is more populated. The lower to middle part of the spectrum has substantial contributions from Co_B and Cr_A atoms. In the middle part of the spectrum (250-350 cm^{-1}), the symmetry lowering and thus lifting of degeneracies bring in contributions from all atoms signifying that the new modes created have contributions from all atoms. Once again we find that there is a competing vibrations of the contributions from all atoms from the lower part of the spectrum to the middle part of the spectrum.

In Figs 6.1(b(i)-(iii)) and Figs 6.1(e(i)-(iii)), we shows the dispersion curves and vibrational density of states $CoCrMnO_4$ for y=0, 0.5 and 1 respectively. We have chosen this composition as lesser Mn compositions would require larger unit cell to represent the "half-inverse" structure and thus increase the computation time enormously. Due to Mn substitution, the symmetry of the system is lowered even for y=0, in comparison to pristine $CoCr_2O_4$. The phonon spectrum,thus, have more bands throughout the spectrum, in comparison to $CoCr_2O_4$ for the same degree of inversion. The densities of states imply that the lower part of the spectrum is dominated by the Co_A atoms while the Cr_B and Mn_B atoms dominate the middle part of the spectrum. The B-O bond strength are once again found to be larger than the A-O bond strengths. This, coupled with smaller average mass at the B sites in comparison to that at the A sites explain the distribution of atom contributions throughout the spectrum. The "half-inverted" structure (y=0.5) now have contributions from both Co_A and Mn_A in the lower frequency part while Cr_B, Co_B and Mn_B dominate the middle and higher frequency parts of the spectrum. A significant difference with $CoCr_2O_4$ in the same state of cation disorder is that the contributions of Co_B in the present case is miniscale in the lower frequency regions. One may recall that in chapter 4, we had shown that for y=0.5, the Co_B-O bond distances reduce drastically in comparison to Mn_B-O and Cr_B-O bond distances. This is linked with the modifications in the crystal fields and the low spin state of Co_B. Thus, the shorter Co_B-O bond strengths in this configuration are as strong as the $Mn_B - O$ bonds. This, thus, explains the distribution of Co vibrations throughout the spectrum in this configuration. The same argument explains the features in the vibrational densities of states in the "full inverted" (y=1) structure. Thus, for $CoCrMnO_4$, the magnetism associated with Co atoms in different symmetry sites influences the lattice dynamics. In case of $CoFeCrO_4$, with y=0 (Fig 6.1(c(i),f(i)), we find that the contribution of Fe_B atoms are more towards the lower part of the spectrum, in comparison with $CoCrMnO_4$. Inspection of force constants reveal that Fe_B-O bonds are much weaker in strength than the Mn_B-O bonds in $CoCrMnO_4$ (y=0). The mass of Fe is larger than Mn as well. These two factors thus explain the shifts of Fe_B modes towards lower frequencies. In comparison to pristine $CoCr_2O_4$, the B-O bonds are substantially weaker due to two factors: (i) the Fe_B-O bonds are longer, thus making the average B-O bonds in $CoCrFeO4$ larger than those in $CoCr_2O_4$ and (ii) the Fe_B-O bonds being significantly weaker in strength in comparison to Cr_B-O bonds in $CoCr_2O4$ reduces the overall strength of the B-O bonds. This shifts the low frequency part of the spectrum in particular, towards lower frequencies, in comparison to $CoCr_2O_4$ with y=0. The "half-inverted" structure, like the case of other two systems studied, have contributions from all atoms throughout the low and medium frequency parts of the spectrum. A noticeable difference with $CoMnCrO_4$ is that, the Co_A and Co_B atoms have contributions mostly in the lower frequency part of the spectrum, with Co_B atoms contributing slightly more towards higher frequencies. This is due to slightly stronger Co_B-O bonds. In case of Fe atoms, Fe_B atoms have more contributions at higher frequencies than the Fe_A atoms. This is again due to the slightly higher stretchibility of the Fe_B-O bonds in comparison to the Fe_A-O bonds. For the "full-inverted" structure (y=1), the salient feature is that the Fe_A and Co_B atoms have substantial contributions at the lower frequencies with Cr_B contributing throughout. This resembles the case of $CoCr_2O_4$ in the same state of cation disorder. This is due to almost same bond strengths of Co_B-O and Fe_A-O along with little differences in their masses.

The relative shifts in the frequencies of the optical modes due to chemical substitution and cation disorder can be quantified the following way:

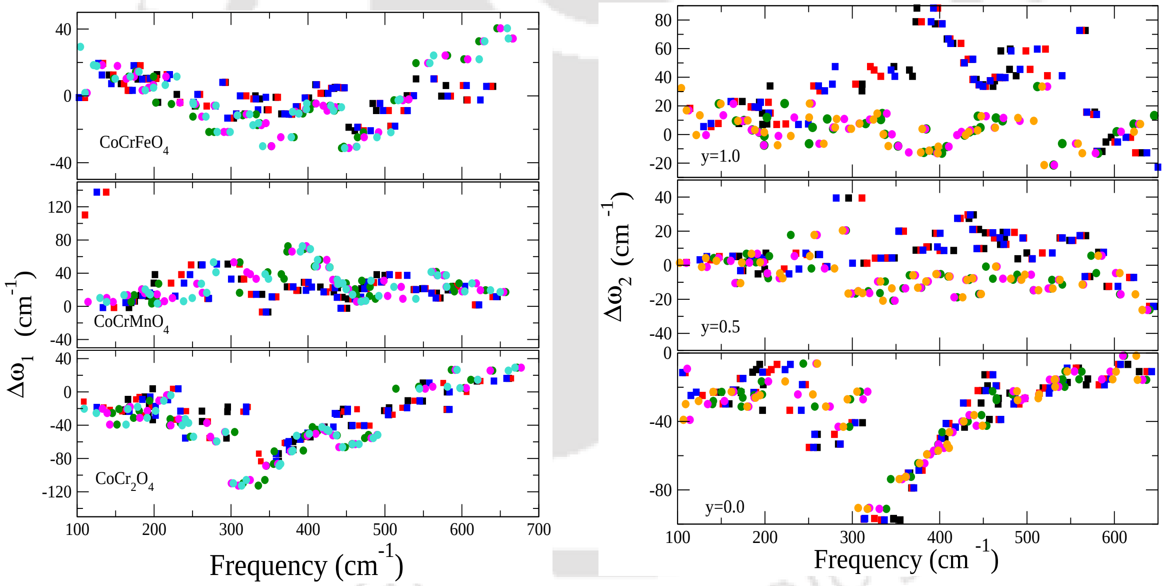

Fig. 6.2 Variations of $\Delta\omega_1(\vec{q})$ (a) and $\Delta\omega_2(\vec{q})$ (b) with frequencies for the three systems. In (a) that is in figures for $\Delta\omega_1(\vec{q})$, squares stand for y=0.5 and circles stands for y=1. Black, red and blue squares are for $\vec{q}$=(0 0 0), (0 0.5 0.5), (0.5 0.5 0.5) respectively. Green, purple and cyan circles are for $\vec{q}$=(0 0 0), (0 0.5 0.5), (0.5 0.5 0.5) respectively. In (b), that is in figures for $\Delta\omega_2(\vec{q})$, squares stand for $CoCrMnO_4$ while circles stand for $CoCrFeO4$. Black, red and blue squares are for $\vec{q}$=(0 0 0), (0 0.5 0.5), (0.5 0.5 0.5) respectively and Green, purple and orange circles are for $\vec{q}$=(0 0 0), (0 0.5 0.5), (0.5 0.5 0.5) respectively.

$$\Delta\omega_1(\vec{q}) = \omega(\vec{q}, y = y') - \omega(\vec{q}, y = 0)$$

$$\Delta\omega_2(\vec{q}) = \omega(\vec{q},y)^{Co(Cr_{1-x}C_x)_2O_4} - \omega(\vec{q},y)^{CoCr_2O_4}$$

where $\vec{q}$ is the wave vector and y'=0.5, 1. These two quantities would be able to quantify the overall frequency shifts and can establish the impacts of effects of substitution and cation disorder separately. In Fig 6.2, we show the results. For $CoCr_2O_4$, we find that the cation disorder produces a “red shift” of the frequencies overall. Except for the higher frequency modes, and mostly in the “completely inverted” configuration, the modes suffer a decrease in the frequencies. The maximum effects are in the range of 300-400 cm^{-1}. As is evident from the densities of states, the middle part of the spectrum gets crowded with new modes originating due to symmetry reduction. The overall decrease in the frequencies for the most part of the spectra, upon inversion, can be understood from the relative strength of the A-O and B-O bonds. The introduction of Co in the octahedral sites reduce the overall bond strengths of the B-O bonds while the opposite happens for the A-O bonds. As a result, the frequencies reduce for the most part of the spectra (with respect to y=0 case). The high frequency modes are dominated by the Cr_B-O pairs whose bond strength increases with y and thus there is a positive shift of the frequencies for these modes. For $CoCrFeO_4$, we do see a rather even distribution, that is, the lowest frequency and the highest frequency modes are “blue shifted”, while the modes in the central part of the spectrum are mostly “red shifted”. The reason can be easily understood from the detailed discussions of the vibrational densities of states. The “blue shifting” of the lowest frequency modes, with inversion, can be explained by the gradual strengthening of the A-O bonds due to introduction of Fe at the tetrahedral sites and by the fact that the high frequency modes have contribution from Fe_A-O and Cr_B-O pairs which have stronger bonds in comparison to y=0 case. The situation with $CoCrMnO_4$ is in complete contrast to the other two systems. Here almost all modes have a positive shifts in their frequencies. This can be understood from the overall bond hardening due to the cation disorder which is related to the low spin state of Co_B, as explained during discussions on the vibrational densities of states. The analysis of $\Delta\omega_2(\vec{q})$ shows that the impacts of chemical substitution maximally affects the “normal” spinel state by significantly reducing the frequencies of all modes. This happens due to the weaker bond strengths of C_B-O bonds (C=Fe, Mn) in comparison to Cr_B-O bonds. For the cation-disordered states, the effects of substitutions are nearly uniformly spread over the entire spectrum with Mn substitutions elevating the frequencies mostly while Fe-substitutions suppressing the frequencies mostly. This, once again, is related to the relative bond strengths associated with the tetrahedra and octahedra. The overall positive shifts in the frequencies due to Mn substitution for the cation-disordered states is related to the low-spin states of Co_B and corresponding increase in the B-O bond strengths. Overall, we find that both chemical substitution and cation disorder affect $CoCr_2O_4$ quite substantially. The frequencies of the modes, by and large, suffer significant reductions, due to lowering of symmetries either by chemical substitution or by cation disorder. The effects of cation disorder on $CoCrFeO_4$ and $CoCrMnO_4$ are found to be in opposite directions qualitatively. This has its origin in the strength of different inter-atomic interactions which arise from differences in masses at different sites and difference in the magnetic state of Co_B atoms.

6.3.3 spin-phonon coupling : formalism and application to $CoCr_2O_4$

The Infra-red spectroscopy study in $CoCr_2O_4$[94] observed anomalous deviations in the frequencies of the IR active modes near the paramagnetic-ferrimagnetic transition. They attributed this to the existence of spin-phonon coupling in $CoCr_2O_4$. The largest deviations were obtained for the modes with frequencies 199 cm^{-1} and 379 cm^{-1} which shifted maximum about 2-2.5 cm^{-1} in a temperature range of 95-25 K. Thus the couplings did not seem quite significant like other spinel compounds, for example $CdCr_2O_4$[61]. Unlike $CdCr_2O_4$, there are two magnetic atoms in $CoCr_2O_4$, and since there are at least two competing magnetic exchange interactions, it is still interesting to investigate the extent of the spin-phonon coupling in this system.

The spin-phonon coupling strength can be obtained the following way. The coupling strength is related to the phonon frequencies of the magnetically ordered phase and the paramagnetic phase through the relation

$$\omega^2 = \omega_{PM}^2 - \sum_{i,j} \lambda_{ij} \langle \vec{S}_i . \vec{S}_j \rangle \tag{6.1}$$

where ω_{PM} is the frequency of the Paramagnetic phase, ω is the frequency of the magnetically ordered phase and λ_{ij} are related with the variations of magnetic exchange interaction J_{ij} with the displacements of the atoms at i^{th} and j^{th} positions.

$$\lambda_{ij} = \langle u_{PM} | J''_{ij} | u_{PM} \rangle \tag{6.2}$$

J''_{ij} is the double derivative of J_{ij} with respect to the displacements of i^{th} and j^{th} atoms, $|u_{PM}\rangle$ is the phonon eigenvector in the paramagnetic phase.

In $CoCr_2O_4$, there are altogether eight different λ_{ij}: λ_{Co-Co} signifying the couplings between two Co atoms , λ_{Co-Cr_i} (i=1-4) signifying the coupling between a Co and four Cr atoms in the unit cell, λ^{xy}_{Cr-Cr}, λ^{yz}_{Cr-Cr}, λ^{zx}_{Cr-Cr} signifying couplings between Cr atoms who are in xy, yz and zx planes respectively. In order to evaluate them, one need to solve at least eight simultaneous equations of the form (6.1). Accordingly, nine different phonon calculations are required. From these calculations, ω in equation 6.1 can be obtained and thus using them in nine different equations, simultaneous evaluations of ω_{PM} and eight different λ_{ij} can be done.

In what follows, we have chosen these nine configurations (Table 6.4) to compute the coupling strengths. The expanded simultaneous equations whose solutions are ω_{PM} and the eight λ_{ij}'s are

$$\begin{cases} \omega_{C_1}^2 = \omega_{PM}^2 - S^2.(8\lambda_{Co-Co} + 8\lambda_{Cr-Cr}^{xy} + 8\lambda_{Cr-Cr}^{yz} + 8\lambda_{Cr-Cr}^{zx} + 12\lambda_{Co-Cr_1} + 12\lambda_{Co-Cr_2} + 12\lambda_{Co-Cr_3} + 12\lambda_{Co-Cr_4}) \\ \omega_{C_2}^2 = \omega_{PM}^2 - S^2.(8\lambda_{Co-Co} + 8\lambda_{Cr-Cr}^{xy} + 8\lambda_{Cr-Cr}^{yz} + 8\lambda_{Cr-Cr}^{zx} - 12\lambda_{Co-Cr_1} - 12\lambda_{Co-Cr_2} - 12\lambda_{Co-Cr_3} - 12\lambda_{Co-Cr_4}) \\ \omega_{C_3}^2 = \omega_{PM}^2 - S^2.(8\lambda_{Co-Co} + 8\lambda_{Cr-Cr}^{xy} - 8\lambda_{Cr-Cr}^{yz} - 8\lambda_{Cr-Cr}^{zx} + 12\lambda_{Co-Cr_1} + 12\lambda_{Co-Cr_2} - 12\lambda_{Co-Cr_3} - 12\lambda_{Co-Cr_4}) \\ \omega_{C_4}^2 = \omega_{PM}^2 - S^2.(8\lambda_{Co-Co} - 8\lambda_{Cr-Cr}^{xy} + 8\lambda_{Cr-Cr}^{yz} - 8\lambda_{Cr-Cr}^{zx} + 12\lambda_{Co-Cr_1} - 12\lambda_{Co-Cr_2} - 12\lambda_{Co-Cr_3} + 12\lambda_{Co-Cr_4}) \\ \omega_{C_5}^2 = \omega_{PM}^2 - S^2.(8\lambda_{Co-Co} - 8\lambda_{Cr-Cr}^{xy} - 8\lambda_{Cr-Cr}^{yz} + 8\lambda_{Cr-Cr}^{zx} + 12\lambda_{Co-Cr_1} - 12\lambda_{Co-Cr_2} + 12\lambda_{Co-Cr_3} - 12\lambda_{Co-Cr_4}) \\ \omega_{C_6}^2 = \omega_{PM}^2 - S^2.(-8\lambda_{Co-Co} + 8\lambda_{Cr-Cr}^{xy} - 8\lambda_{Cr-Cr}^{yz} - 8\lambda_{Cr-Cr}^{zx}) \\ \omega_{C_7}^2 = \omega_{PM}^2 - S^2.(-8\lambda_{Co-Co} - 8\lambda_{Cr-Cr}^{xy} + 8\lambda_{Cr-Cr}^{yz} - 8\lambda_{Cr-Cr}^{zx}) \\ \omega_{C_8}^2 = \omega_{PM}^2 - S^2.(-8\lambda_{Co-Co} - 8\lambda_{Cr-Cr}^{xy} - 8\lambda_{Cr-Cr}^{yz} + 8\lambda_{Cr-Cr}^{zx}) \\ \omega_{C_9}^2 = \omega_{PM}^2 - S^2.(-8\lambda_{Co-Co} + 8\lambda_{Cr-Cr}^{xy} + 8\lambda_{Cr-Cr}^{yz} + 8\lambda_{Cr-Cr}^{zx}) \end{cases} \tag{6.3}$$

Table 6.4 To calculate the spin-phonon coupling strength in $CoCr_2O_4$, we have used these nine different spin configurations. Here we have done calculations in a 14 atom unit cell of $CoCr_2O_4$, where there are two Co atoms and four Cr atoms. The Co_1 and Co_2 atoms are at (0.875,0.875,0.875) and (0.125,0.125,0.125) wyckoff positions of $Fd\bar{3}m$ space group respectively. The four Cr atom are in chosen to be in positions (0.5,0.5,0.5), (0,0.5,0.5), (0.5,0,0.5) and (0.5,0.5,0) respectively. The Ferrimagnetic *Néel* configuration is represented by the configuration C_2.

configuration	Co_1	Co_2	Cr_1	Cr_2	Cr_3	Cr_4
C_1	↑	↑	↑	↑	↑	↑
C_2	↓	↓	↑	↑	↑	↑
C_3	↑	↑	↑	↑	↓	↓
C_4	↑	↑	↑	↓	↓	↑
C_5	↑	↑	↑	↓	↑	↓
C_6	↑	↓	↑	↑	↓	↓
C_7	↑	↓	↑	↓	↓	↑
C_8	↑	↓	↑	↓	↑	↓
C_9	↑	↓	↑	↑	↑	↑

In Table 6.5 we show the various spin phonon coupling strengths and the frequency shifts $\Delta\omega$ associated with each mode (Table 6.3)in "normal spinel" $CoCr_2O_4$. Since we are interested in the changes near the Ferrimagnetic transition, we use the equation corresponding to the C_2 configuration from the sets of equations 6.3. We first focus on the four IR active T_{1u}

modes as experimental results on the frequency shifts of these modes near the magnetic transition are available [94]. Our results, to begin with, shows that the degeneracies associated with these modes are broken. This was to be expected as the spin-phonon interaction near the magnetic transition should break the degeneracies of the vibration modes. Surprisingly, we did not find such a thing in the experimental results. Out of the four IR active modes, the experimentalists observed a frequencies shifts of 1.97 and 2.32 cm^{-1} for the two lower frequency one, For the two higher frequency modes, the shifts were very weak (less than 1 cm^{-1}). In our calculations, we however found larger shifts corresponding to the transverse oscillations for the two lower frequency modes (204cm^{-1} and 371cm^{-1}) while the longitudinal modes had much smaller shifts (2.8 cm^{-1} for the mode at 204 cm^{-1} and -4.2 cm^{-1} for the mode at 371 cm^{-1}, in comparison to 4-5 cm^{-1} for transverse modes corresponding to the modes at 204 cm^{-1} and 23.4 cm^{-1} for transverse modes corresponding to the mode at 371 cm^{-1}). The shifts are small yet appreciable for the modes at frequencies of 466 cm^{-1} and 562 cm^{-1}. From the computed values of different λ_{ij} for the IR active modes we find appreciable contributions of the Co-Co pairs, although the Co-Cr pairs dominated as a whole. The overall values of λ_{tot} for these modes were not substantial for the modes with frequencies 204cm^{-1}, 466 cm^{-1} and 562 cm^{-1} in comparison to the typical case of $CdCr_2O_4$ [61]. This is because of the competing λ_{ij}s associated with different pairs and different directions of changes in the J_{ij}. This is an artifact of the competing exchange interactions associated with three pairs of magnetic cations in this system as presented in Table 3.5. For the Raman active modes we find quite strong spin-phonon couplings in E_g (frequency 433cm^{-1}) and the two T_{2g} modes (frequencies 470 cm^{-1} and 565 cm^{-1}). The frequency shifts are as large as 13.1 cm^{-1} and 12.5 cm^{-1}. Once again, these large shifts are primarily due to the $Co-Cr$ and $Cr-Cr$ pairs, the two pairs with competing magnetic exchange interactions. The results are thus consistent with the picture of competing exchange interactions in this system. However, we find that the Co-Co couplings are also substantial in general and is homogenous while the loss of degeneracy is due to spin-spin coupling affects the Cr-Cr and Co-Cr pairs. Thus, oveall our generalised scheme for computing the spin-phonon couplings in oxide spinel with more than one magnetic cations applied to $CoCr_2O_4$ provided a quantitative picture of the said coupling which is consistent with the information on various magnetic exchange interactions and the results obtained from experiments.

6.4 Summary

In this chapter, we have investigated the vibrational properties of $CoCr_2O_4$ and Fe and Mn substituted $CoCr_2O_4$. Our focus primarily has been on understanding of the effects of sub-

Table 6.5 Spin-phonon coupling strengths associated with different pairs of atoms are tabulated for each phonon modes of $CoCr_2O_4$ in the $Fd\bar{3}m$ space group. All the λ are in cm^{-2} and frequencies (ω, $\Delta\omega$) are in cm^{-1}. The total strength of spin-phonon coupling λ_{tot} is the sum of all λ_{ij}s, where i,j represent the chemical specie.

	ω	λ_{Co-Co}	λ^{xy}_{Cr-Cr}	λ^{yz}_{Cr-Cr}	λ^{zx}_{Cr-Cr}	λ_{Co-Cr_1}	λ_{Co-Cr_2}	λ_{Co-Cr_3}	λ_{Co-Cr_4}	$\sum_i \lambda_{Co-Cr_i}$	λ_{tot}	$\Delta\omega$
$T^{(1)}_{2u}$	191	-153	-172	-36	-37	150	-68	-60	-58	-37	2737	7.4
		-153	-172	-36	-37	12	43	-47	-45	-37	2737	7.4
		-153	-17	-12	-13	120	-54	-52	-52	-37	1117	2.4
$T^{(1)}_{2g}$(R)	195	46	-34	-13	-29	51	-88	25	15	3	302	0.8
		46	-34	-13	-29	-84	36	29	22	3	302	0.8
		46	27	10	21	-5	-7	4	12	3	-796	-2.0
$T^{(1)}_{1u}$(IR)	204	-94	-37	-48	-29	115	-34	-40	-20	19	1913	4.8
		-94	-2	-13	-64	108	-34	-12	-42	19	1632	4.1
		-94	-2	-3	-11	113	-34	-27	-32	19	1125	2.8
$E^{(1)}_{u}$	310	18	-525	-559	-549	-78	6	-9	-2	-82	11934	20.6
		18	-268	-250	-250	-30	-16	-17	-17	-82	5008	8.3
$T^{(2)}_{1u}$(IR)	371	137	-757	-706	-707	179	-112	-35	-36	-4	16216	23.4
		137	-757	-706	-707	-451	176	135	134	-4	16216	23.4
		137	89	81	81	-155	44	53	52	-4	-3174	-4.2
T_{1g}	406	-502	-27	181	-37	707	-204	-235	-333	-65	2298	2.8
		-502	72	82	62	527	-415	-90	-86	-65	1501	1.8
		-502	-101	294	235	288	-49	-126	-177	-65	-198	-0.2
E_g(R)	433	-921	-533	226	99	365	246	-180	-251	179	11182	13.1
		-921	424	240	242	915	-282	-227	-226	179	2256	2.6
$T^{(2)}_{2u}$	447	-645	46	-100	-76	641	-254	-231	-211	-56	5527	6.3
		-645	149	100	165	895	-236	-419	-296	-56	1158	1.3
		-645	149	100	165	495	-336	-148	-66	-56	1158	1.3
$T^{(3)}_{1u}$(IR)	466	-525	29	225	221	612	-92	-246	-247	26	712	0.8
		-525	61	221	226	295	-5	-136	-127	26	456	0.5
		-525	188	66	62	769	-358	-189	-194	26	1987	2.1
$T^{(2)}_{2g}$(R)	470	-109	-596	-398	-845	732	-400	88	-218	202	18024	19.5
		-109	-335	-82	-95	108	75	11	6	202	7408	7.8
		-109	5	-47	-39	-81	61	108	113	202	3955	4.1
$A^{(1)}_{2u}$	471	42	230	257	251	310	-113	-84	-89	22	-5991	-6.2
$E^{(2)}_{u}$	480	-505	365	504	495	927	-332	-270	-274	50	-6279	-6.4
		-505	365	504	495	259	-31	-85	-92	50	-6279	-6.4
$T^{(4)}_{1u}$(IR)	562	-260	101	278	272	653	-122	-25	-26	478	2603	2.3
		-260	101	278	272	138	139	103	96	478	2603	2.3
		-260	432	607	609	504	20	-24	-21	478	-5371	-4.7
$T^{(3)}_{2g}$(R)	565	-264	247	481	482	319	-8	-51	-46	212	-5036	-4.4
		-264	468	481	482	315	-60	-21	-21	212	-6798	-5.9
		-264	754	822	825	397	-55	-66	-64	212	-14563	-12.5
$A^{(2)}_{2u}$	615	-156	213	367	366	282	11	10	11	315	-2540	-2.0
A_{1g}(R)	650	-955	68	278	281	1032	-252	-252	-247	281	5993	4.6

stitution and cation disorder in $CoCr_2O_4$. We have performed a detailed analysis of these effects on $CoCr_2O_4$, $CoCrFeO_4$, and $CoCrMnO_4$ using results of first-principles calculations. We find that the changes in co-ordinations of the same atom due to cation disorder affects the bond strengths influencing the vibrational modes. The effects are found to be quite significant for $CoCrMnO_4$ where the changes in the magnetic state of Co atoms in octahedral Co-ordinations is found to be responsible. In general, we found that both substitution and the degree of cation disorder have important effects on the optical phonon modes. We have also investigated into the spin-phonon coupling in $CoCr_2O_4$. We have constructed a generalized scheme for quantifications of the spin-phonon coupling strengths associated with different phonon modes for AB_2O_4 spinels where both A and B are magnetic cations. Our computations for $CoCr_2O_4$ shows that the scenario with the spin-phonon coupling is quite complex and is dependent upon the competitions between different magnetic exchange interactions. We found larger effects on the IR-active modes than that found in the experiments. The results are quite comprehensive in quantifying the spin-phonon coupling associated with each mode and could motivate the experimentalists for further study. We could not extend the formalism to substituted systems $A(B_{1-x}C_x)_2O_4$ where C is a magnetic ion replacing B. This is because of the fact that the number of magnetic exchange interactions required would increase proportionally and a significantly larger number of phonon calculations with larger system sizes would be required which is prohibitively large from the point of view of computational resources.

Chapter 7

Conclusions and Scopes for future work

7.1 Conclusions

In this thesis, we have performed *ab initio* calculations to investigate Fe and Mn substituted $CoCr_2O_4$ spinel oxides. Our investigations involved computations of properties of the end compounds $CoCr_2O_4$, $CoMn_2O_4$ and $CoFe_2O_4$ as well as the substitutional system $Co(Cr_{1-x}Mn_x)_2O_4$ and $Co(Cr_{1-x}Fe_x)_2O_4$, 0<x<1. The focus of the thesis is a qualitative understanding of the effects of substituting another magnetic cation at the B site of an AB_2O_4 spinel compound on the site occupancies, structural properties, magnetic interactions and electronic properties, wherever required. These enable one to understand the fundamentals of the pristine and substituted spinel oxides based upon analysis of their electronic structures, crystal field, electron-electron correction effect etc.

In this first chapter, a brief introduction on magnetic materials, oxides materials and magnetic spinel oxides is followed by a description of various concepts, knowledge of which is necessary to study spinel oxides, such as the magnetic geometrical frustration, the crystal field effects, Jahn-Teller distortion and the cation disorder. The new and novel phenomena, observed experimentally in $CoCr_2O_4$ and Fe, Mn substituted $CoCr_2O_4$, their importances are discussed thereafter which justifies the work carried out in this thesis.

In the second chapter, we discuss the methodologies used in this work. After a brief introduction of Density Functional Theory (DFT), the backbone for modern-first principles electronic structure methods, we introduces the DFT+U method, a formalism that goes beyond DFT and treats the many body electron-electron correlation in a parametrized way. Going beyond DFT was necessary in this thesis as the materials investigate are transition-metal oxides where electron-electron correlation is very strong. The chapter ends with brief description of the implementation of the DFT that is being used throughout the thesis.

In the following chapter, we perform systematic in-depth computations of the properties of the three oxides $CoCr_2O_4$, $CoMn_2O_4$ and $CoFe_2O_4$. The motivation was to understand the microscopic physics associated with each of them which would be a prelude to the next chapters where results for Fe and Mn substituted $CoCr_2O_4$ are presented. We perform detailed analysis of the structural parameters, magnetic moments and magnetic exchange parameters in terms of their electronic structures and the competitions between the crystal field and the magnetic exchange fields which are obtained from the electronic structures. Our calculations reveal that the electron-electron correction is absolutely important to obtain the correct ground states in these systems. The strong electron-electron correlations are found to be responsible for local and global structural distortions in $CoMn_2O_4$. The magnetic interactions of the three compounds are found to be substantially different which is connected with the differences in their electronic structures. Thus, the results obtained in this chapter provide an explanation of the differences in their ground state magnetic structures. The analysis of the differences in their electronic structures by quantifying their crystal field and exchange field provided a clear picture of the microscopic physics associated with these three compounds.

In the next chapter, we investigate the Mn substituted $CoCr_2O_4$ system, $Co(Cr_{1-x}Mn_x)_2O_4$ and interpret the available experimental results. In this chapter, we make a very important contribution which goes beyond the systems investigated. We extend an existing thermodynamics model for computing the “degree of cation disorder” for arbitrary temperature in AB_2O_4 spinels, to $A(B_{1-x}C_x)_2O_4$ spinels for an arbitrary temperature and composition. Combining this thermodynamic model with total energy calculations with DFT+U, we make an accurate estimation of the “degree of cation disorder” and its dependencies on composition and temperature. For $Co(Cr_{1-x}Mn_x)_2O_4$, this procedure yielded very interesting results on the site occupancy patterns of Co and Mn as the composition changes. We demonstrated that the non-regular site occupancy pattern in this material is intricately related with the charge states of the cations affected by the disorder which in turn affects the crystal fields associated with the crystallographic sites of different symmetry and the magnetism in the system. The experimentally observed anomalous behavior in the structural and magnetic properties could be explained through this approach, in spite of considering a collinear magnetic structure throughout, while the actual magnetic structure of the system is non-collinear. The significance of this particular chapter is that the *ab initio* based approach adopted here can be used to understand the complexities associated with chemical substitution and cation disorder for magnetic oxides in spinel structures, in general.

In the following chapter, we investigate the Fe substituted $CoCr_2O_4$, $Co(Cr_{1-x}Fe_x)_2O_4$ using the approach adopted in the previous chapter. Our calculations demonstrated how the magnetic structure evolves from a non-collinear one to a collinear one as Fe content in the system increases. Although it was known that $CoFe_2O_4$ has a collinear ground state as opposed to a non-collinear one in $CoCr_2O_4$, the effects of cation disorder, and its relation with the magnetic order was never explored to have a qualitative picture of the emergence of the collinear magnetic order when Cr is gradually substituted with Fe. Our calculations and analysis clearly showed that the degree of cation order and the composition, both, are responsible for the emergence of the collinear magnetic order in $Co(Cr_{1-x}Fe_x)_2O_4$. We also provided a microscopic picture of competing magnetic exchange interactions to explain the above. The contents of this chapter, thus, provides fundamental insight into the effects of Fe substitution in $CoCr_2O_4$.

In chapter 6, we discuss the vibrational properties of pristine and Fe and Mn substituted $CoCr_2O_4$. Apart from calculating the effects of cation disorder on phonon dispersion relations and vibrational densities of states in these systems, we look at possible spin-phonon coupling in these systems, observed in recent experiments. One major contribution of this work is that we provide a generalization of an existing method to quantify spin-phonon coupling in AB_2O_4 with either A or B being magnetic ions, to the cases where both A and B are magnetic ions. Due to limitations on the resources, we could apply this generalized approach to $CoCr_2O_4$ only.

Summarizing, this thesis is probably the first complete first-principles electronic structure based investigations into the Fe and Mn substituted $CoCr_2O_4$, a very recently discovered multifunctional material, a lot about which is yet to be discovered. This thesis, in a systematic and coherent way, tries to shed some light on the fundamental physics of this system. Generalizations of the existing models in two different occasions, done in this thesis, pave the ways to treat similar systems in future.

7.2 Scope for future work

The extensions of the work presented in this thesis can be in various directions. In this work we have not considered the non-collinear spin structure of $CoCr_2O_4$ and Mn-substituted $CoCr_2O_4$ as calculations with them are computationally expensive and information on the actual non-collinear structure is not known except for $CoCr_2O_4$ and $CoMn_2O_4$. Also the focus of the present thesis was on understanding the impacts of cation substitutions and cation disorder on physical properties in a qualitative way. Thus, one immediate extension is towards computations of the actual magnetic structures in all the compounds studied, in an *ab initio* way.

The Fe-substituted $CoCr_2O_4$, in particular, has drown attention due to the discovery of exchange bias and magnetic compensation for small concentrations of Fe in $CoCr_2O_4$. One extension of the present work could be towards computations and analysis of these phenomena in a first-principles way. Of particular importance would be an understanding of how these phenomena emerge for a limited concentration range of Fe and how they disappear upon further increase of Fe content in $CoCr_2O_4$.

Another possible extension of the work contained in this thesis would be towards increasing the accuracy in determining the “inversion parameter” for a given composition and temperature. This can be done in two ways: (i) by considering more structures with different “degrees of inversion” so that the fitting to a quadratic analytic function become more accurate. For an arbitrary composition, this is a challenging task as it would require constructions of larger supercells than those used in the present thesis and would require significantly larger computational resources and (ii) by considering the effects of lattice vibrations in the expression for entropy. This too would be quite challenging as modeling an arbitrary composition and computations of the phonon dispersions would require huge computational power.

The evaluation of spin-phonon coupling strengths for substituted $CoCr_2O_4$ is another direction where further work can be done. As we have mentioned in chapter 6, this also is a cumbersome task as the number of magnetic configurations required for such evaluation would increase significantly in presence of a third magnetic cation. However, this could be a significant contribution towards investigations of couplings of two different degrees of freedom.

References

[1] Alfè, D. (2009). Phon: A program to calculate phonons using the small displacement method. *Computer Physics Communications*, 180(12):2622–2633.

[2] Anisimov, V. I., Aryasetiawan, F., and Lichtenstein, A. I. (1997). First-principles calculations of the electronic structure and spectra of strongly correlated systems: the LDA + U method. *Journal of Physics: Condensed Matter*, 9(4):767.

[3] Antonio Facchetti, T. J. M. (2010). *Transparent Electronics: From Synthesis to Applications*. Wiley.

[4] Armiento, R. and Mattsson, A. E. (2005). Functional designed to include surface effects in self-consistent density functional theory. *Phys. Rev. B*, 72:085108.

[5] Bacon, G. E. and Roberts, F. F. (1953). Neutron-diffraction studies of magnesium ferrite–aluminate powders. *Acta Crystallographica*, 6(1):57–62.

[6] Balents, L. (2010). Spin liquids in frustrated magnets. *Nature*, 464(7286):199–208.

[7] Baroni, S., de Gironcoli, S., Dal Corso, A., and Giannozzi, P. (2001). Phonons and related crystal properties from density-functional perturbation theory. *Rev. Mod. Phys.*, 73:515–562.

[8] Barth, T. and Posnjak, E. (1932). Spinel structures: with and without variate atom equipoints. *Crystalline Materials*, 82:325–341.

[9] Baudin, C., Martinez, R., and Pena, P. (1995). High-temperature mechanical behavior of stoichiometric magnesium spinel. *Journal of the American Ceramic Society*, 78(7):1857–1862.

[10] Berger, L. (1996). Emission of spin waves by a magnetic multilayer traversed by a current. *Phys. Rev. B*, 54:9353–9358.

[11] Blöchl, P. E. (1994). Projector augmented-wave method. *Phys. Rev. B*, 50:17953–17979.

[12] Blundell, S. (2001). *Magnetism in Condensed Matter*. Oxford University.

[13] Bordács, S., Varjas, D., Kézsmárki, I., Mihály, G., Baldassarre, L., Abouelsayed, A., Kuntscher, C. A., Ohgushi, K., and Tokura, Y. (2009). Magnetic-order-induced crystal symmetry lowering in ACr_2O_4 ferrimagnetic spinels. *Phys. Rev. Lett.*, 103:077205.

[14] Born, M. and Oppenheimer, R. (1927). Zur quantentheorie der molekeln. *Annalen der Physik*, 389(20):457–484.

[15] Boucher, B., Buhl, R., and Perrin, M. (1968). Magnetic structure of cobalt manganite by neutron diffraction. *Journal of Applied Physics*, 39(2):632–634.

[16] Boucher, B., Buhl, R., and Perrin, M. (1969). Magnetic structure of iron manganite by neutron diffraction. *Journal of Applied Physics*, 40(3):1126–1127.

[17] Brian N. Figgis, M. A. H. (1999). *Ligand Field Theory and Its Applications*. Wiley VCH.

[18] Brittman, S., Yoo, Y., Dasgupta, N. P., Kim, S.-i., Kim, B., and Yang, P. (2014). Epitaxially aligned cuprous oxide nanowires for all-oxide, single-wire solar cells. *Nano Letters*, 14(8):4665–4670. PMID: 25014113.

[19] Buhl, R. (1969). Manganites spinelles purs d'elements de transition preparations et structures cristallographiques. *Journal of Physics and Chemistry of Solids*, 30(4):805–812.

[20] CFSE (2015). *https://chem.libretexts.org*. Chemistry libretext.

[21] Cheetham, A. K. and Hope, D. A. O. (1983). Magnetic ordering and exchange effects in the antiferromagnetic solid solutions $\mathrm{Mn_xNi_{1-x}O_4}$. *Phys. Rev. B*, 27:6964–6967.

[22] Chiu, T.-W., Tonooka, K., and Kikuchi, N. (2008). Fabrication of ZnO and $\mathrm{CuCrO_2}$: Mg thin films by pulsed laser deposition with in situ laser annealing and its application to oxide diodes. *Thin Solid Films*, 516(18):5941–5947.

[23] Chung, J.-H., Matsuda, M., Lee, S.-H., Kakurai, K., Ueda, H., Sato, T. J., Takagi, H., Hong, K.-P., and Park, S. (2005). Statics and dynamics of incommensurate spin order in a geometrically frustrated antiferromagnet $\mathrm{CdCr_2O_4}$. *Phys. Rev. Lett.*, 95:247204.

[24] Cococcioni, M. and de Gironcoli, S. (2005). Linear response approach to the calculation of the effective interaction parameters in the $\mathrm{LDA}+\mathrm{U}$ method. *Phys. Rev. B*, 71:035105.

[25] Corliss, L. M., Hastings, J. M., and Brockman, F. G. (1953). A neutron diffraction study of magnesium ferrite. *Phys. Rev.*, 90:1013–1018.

[26] Das, D., Biswas, R., and Ghosh, S. (2016a). Systematic analysis of structural and magnetic properties of spinel $\mathrm{Co}Cr_2O_4$,($\mathrm{B} = \mathrm{Cr}$,Mn and Fe) compounds from their electronic structures. *Journal of Physics: Condensed Matter*, 28(44):446001.

[27] Das, D., Ganguly, S., Sanyal, B., and Ghosh, S. (2016b). Effect of fe doping in the structural, electronic and magnetic properties of $\mathrm{CoCr_2O_4}$: insights from ab initio calculations. *Materials Research Express*, 3(10):106106.

[28] Das, D. and Ghosh, S. (2015). Density functional theory based comparative study of electronic structures and magnetic properties of spinel $\mathrm{ACr_2O_4}$(A=Mn,Fe,Co,Ni) compounds. *Journal of Physics D: Applied Physics*, 48(42):425001.

[29] Das, D. and Ghosh, S. (2017). First-principles investigations into the thermodynamics of cation disorder and its impact on electronic structure and magnetic properties of spinel $Co(Cr_{1-x}Mn_x)_2O_4$. *Journal of Physics: Condensed Matter*, 29(5):055805.

[30] Diep, H. T. and Giacomini, H. (2005). *Frustrated Spin System*. World Scientific.

[31] Dudarev, S. L., Botton, G. A., Savrasov, S. Y., Humphreys, C. J., and Sutton, A. P. (1998). Electron-energy-loss spectra and the structural stability of nickel oxide: An LSDA + U study. *Phys. Rev. B*, 57:1505–1509.

[32] Dunitz, J. and Orgel, L. (1957). Electronic properties of transition-metal oxides-I. *Journal of Physics and Chemistry of Solids*, 3(1):20–29.

[33] Ebert, H., Kodderitzsch, D., and Minar, J. (2011). Calculating condensed matter properties using the KKR – Green's function method-recent developments and applications. *Reports on Progress in Physics*, 74(9):096501.

[34] Ederer, C. and Komelj, M. (2007). Magnetic coupling in $CoCr_2O_4$ and $MnCr_2O_4$: An LSDA + U study. *Phys. Rev. B*, 76:064409.

[35] Efthimiopoulos, I., Liu, Z. T. Y., Khare, S. V., Sarin, P., Lochbiler, T., Tsurkan, V., Loidl, A., Popov, D., and Wang, Y. (2015). Pressure-induced transition in the multiferroic $CoCr_2O_4$ spinel. *Phys. Rev. B*, 92:064108.

[36] Fennie, C. J. and Rabe, K. M. (2005). Polar phonons and intrinsic dielectric response of the ferromagnetic insulating spinel $CdCr_2S_4$ from first principles. *Phys. Rev. B*, 72:214123.

[37] Fennie, C. J. and Rabe, K. M. (2006). Magnetically induced phonon anisotropy in $ZnCr_2O_4$ from first principles. *Phys. Rev. Lett.*, 96:205505.

[38] Ferreira, T., Waerenborgh, J., Mendonça, M., Nunes, M., and Costa, F. (2003). Structural and morphological characterization of $FeCo_2O_4$ and $CoFe_2O_4$ spinels prepared by a coprecipitation method. *Solid State Sciences*, 5(2):383–392.

[39] Fritsch, D. and Ederer, C. (2010). Epitaxial strain effects in the spinel ferrites $CoFe_2O_4$ and $NiFe_2O_4$ from first principles. *Phys. Rev. B*, 82:104117.

[40] Ganguly, S., Chimata, R., and Sanyal, B. (2015). Overcoming magnetic frustration and promoting half-metallicity in spinel $CoCr_2O_4$ by doping with Fe. *Phys. Rev. B*, 92:224417.

[41] Habjanič, J., Jurić, M., Popović, J., Molčanov, K., and Pajic, D. (2014). A 3D oxalate-based network as a precursor for the $CoMn_2O_4$ spinel: Synthesis and structural and magnetic studies. *Inorganic Chemistry*, 53(18):9633–9643.

[42] Harris, M. (1999). Condensed-matter physics: Taking the frustration out of ice. *Nature*, 399(6734):311–312.

[43] Heyd, J., Scuseria, G. E., and Ernzerhof, M. (2003). Hybrid functionals based on a screened coulomb potential. *The Journal of Chemical Physics*, 118(18):8207–8215.

[44] Hill, R. J., Craig, J. R., and Gibbs, G. V. (1979). Systematics of the spinel structure type. *Physics and Chemistry of Minerals*, 4(4):317–339.

[45] Hohenberg, P. and Kohn, W. (1964). Inhomogeneous electron gas. *Phys. Rev.*, 136:B864–B871.

[46] Hou, Y. H., Zhao, Y. J., Liu, Z. W., Yu, H. Y., Zhong, X. C., Qiu, W. Q., Zeng, D. C., and Wen, L. S. (2010). Structural, electronic and magnetic properties of partially inverse spinel $CoFe_2O_4$: a first-principles study. *Journal of Physics D: Applied Physics*, 43(44):445003.

[47] Hubbard, J. (1967). Electron correlations in narrow energy bands. v. a perturbation expansion about the atomic limit. *Proceedings of the Royal Society of London. Series A, Mathematical and Physical Sciences*, 296(1444):82–99.

[48] Jahn, H. A. and Teller, E. (1937). Stability of polyatomic molecules in degenerate electronic states. i. orbital degeneracy. *Proceedings of the Royal Society of London A: Mathematical, Physical and Engineering Sciences*, 161(905):220–235.

[49] Jiang, C., Sickafus, K. E., Stanek, C. R., Rudin, S. P., and Uberuaga, B. P. (2012). Cation disorder in MgX_2O_4,(X = Al,Ga and In) spinels from first principles. *Phys. Rev. B*, 86:024203.

[50] Jonker, G. (1959). Analysis of the semiconducting properties of cobalt ferrite. *Journal of Physics and Chemistry of Solids*, 9(2):165–175.

[51] Kalvius, G., Krimmel, A., Hartmann, O., Litterst, F., Wappling, R., Tsurkan, V., and Loidl, A. (2009). Magnetism of frustrated $A-$site spinels. *Physica B: Condensed Matter*, 404(5-7):660–662. Proceedings of the Eleventh International Conference on Muon Spin Rotation, Relaxation and Resonance.

[52] Kaplan, T. A. (1960). Classical theory of spin configurations in the cubic spinel. *Phys. Rev.*, 119:1460–1470.

[53] Kim, K.-W., Cho, P.-S., Kim, S.-J., Lee, J.-H., Kang, C.-Y., Kim, J.-S., and Yoon, S.-J. (2007). The selective detection of C_2H_5OH using SnO_2-ZnO thin film gas sensors prepared by combinatorial solution deposition. *Sensors and Actuators B: Chemical*, 123(1):318–324.

[54] Kim, S., Lee, S., and Kim, C. (2001). Mössbauer studies on exchange interactions in $CoFe_2O_4$. *Japanese Journal of Applied Physics*, 40(8R):4897.

[55] Kocsis, V., Bordács, S., Varjas, D., Penc, K., Abouelsayed, A., Kuntscher, C. A., Ohgushi, K., Tokura, Y., and Kézsmárki, I. (2013). Magnetoelasticity in ACr_2O_4 spinel oxides (A = Mn,Fe,Co, Ni, and Cu). *Phys. Rev. B*, 87:064416.

[56] Kohn, W. and Sham, L. J. (1965). Self-consistent equations including exchange and correlation effects. *Phys. Rev.*, 140:A1133–A1138.

[57] Kresse, G. and Furthmüller, J. (1996). Efficiency of ab-initio total energy calculations for metals and semiconductors using a plane-wave basis set. *Computational Materials Science*, 6(1):15–50.

[58] Kriessman, C. J. and Harrison, S. E. (1956). Cation distributions in ferrospinels. magnesium-manganese ferrites. *Phys. Rev.*, 103:857–860.

[59] Kubler, J., Hock, K. H., Sticht, J., and Williams, A. R. (1988). Density functional theory of non-collinear magnetism. *Journal of Physics F: Metal Physics*, 18(3):469.

[60] Kulkarni, J. and Darshane, V. (1985). Effect of high temperatures on cation distribution: NiMn2O4 – FeMn2O4 system. *Thermochimica Acta*, 93:473–476.

[61] Kumar, A., Fennie, C. J., and Rabe, K. M. (2012). Spin-lattice coupling and phonon dispersion of $CdCr_2O_4$ from first principles. *Phys. Rev. B*, 86:184429.

[62] Kumar, R., Padam, R., Rayaprol, S., Siruguri, V., and Pal, D. (2016). Correlation of exchange bias with magneto-structural effects across the compensation temperature of $Co(Cr_{1-x}Fe_x)_2O_4$ (x = 0.05 and 0.075). *Journal of Applied Physics*, 119(12):123903.

[63] L., U. E., G., M. I., and G., K. D. (1997). Synthesis of nano-dimensional iron-cobalt spinel mixed oxides from layered-type carbonate hydroxide precursors. *Bulletin of the Chemical Society of Japan*, 70(8):1985–1993.

[64] Lawes, G., Melot, B., Page, K., Ederer, C., Hayward, M. A., Proffen, T., and Seshadri, R. (2006). Dielectric anomalies and spiral magnetic order in $CoCr_2O_4$. *Phys. Rev. B*, 74:024413.

[65] Lee, M.-J., Han, S., Jeon, S. H., Park, B. H., Kang, B. S., Ahn, S.-E., Kim, K. H., Lee, C. B., Kim, C. J., Yoo, I.-K., Seo, D. H., Li, X.-S., Park, J.-B., Lee, J.-H., and Park, Y. (2009). Electrical manipulation of nanofilaments in transition-metal oxides for resistance-based memory. *Nano Letters*, 9(4):1476–1481.

[66] Lee, S.-H., Broholm, C., Kim, T. H., Ratcliff, W., and Cheong, S.-W. (2000). Local spin resonance and spin-peierls-like phase transition in a geometrically frustrated antiferromagnet. *Phys. Rev. Lett.*, 84:3718–3721.

[67] Li, Y., Ma, B., Chen, N., Lu, J., Wang, A., Liu, L., Liu, Y., Wang, W., Li, X., Cardona, Y., Uwakweh, O., Rong, C., Gao, J., Lu, J., Xu, Z., Ma, X., and Cao, G. (2010). Structural and magnetic properties of $LiMn_{1.5}Fe_{0.5}O_4$ spinel oxide. *Physica B: Condensed Matter*, 405(23):4733–4739.

[68] Liechtenstein, A., Katsnelson, M., Antropov, V., and Gubanov, V. (1987). Local spin density functional approach to the theory of exchange interactions in ferromagnetic metals and alloys. *Journal of Magnetism and Magnetic Materials*, 67(1):65–74.

[69] Liu, S., Ji, D., Xu, J., Li, Z., Tang, G., Bian, R., Qi, W., Shang, Z., and Zhang, X. (2013). Estimation of cation distribution in spinel ferrites $Co_{1+x}Fe_{2-x}O_4$ ($0.0 < x < 2.0$) using the magnetic moments measured at 10 K. *Journal of Alloys and Compounds*, 581:616–624.

[70] Loukes, T. L. (1967). *The Augmented-Plane-Wave Method*. Benjamin,New York.

[71] Lutz, H. D., Müller, B., and Steiner, H. J. (1991). Lattice vibration spectra. LIX. Single crystal infrared and Raman studies of spinel type oxides. *Journal of Solid State Chemistry France*, 90:54–60.

[72] Lyons, D. H., Kaplan, T. A., Dwight, K., and Menyuk, N. (1962). Classical theory of the ground spin-state in cubic spinels. *Phys. Rev.*, 126:540–555.

[73] MacDougall, G. J., Gout, D., Zarestky, J. L., Ehlers, G., Podlesnyak, A., McGuire, M. A., Mandrus, D., and Nagler, S. E. (2009). Kinetically inhibited order in a diamond-lattice antiferromagnet. *Proc Natl Acad Sci U S A*, 108(38):15693–15698.

[74] Martin, R. M. (2003). *Electronic Structure: Basic Theory and Practical Methods*. Cambridge University Press.

[75] McClure, D. S. (1957). The distribution of transition metal cations in spinels. *Journal of Physics and Chemistry of Solids*, 3(3):311–317.

[76] Minh, N. V. and Yang, I.-S. (2004). A raman study of cation-disorder transition temperature of natural $MgAl_2O_4$ spinel. *Vibrational Spectroscopy*, 35(1-2):93–96. The 2nd International Conference on Advanced Vibrational Spectroscopy (ICAVS-2).

[77] Miyahara, S. and Ohnishi, H. (1956). Cation arrangement and magnetic properties of copper ferrite-chromite series. *Journal of the Physical Society of Japan*, 11(12):1296–1297.

[78] Moffitt, W. and Ballhausen, C. J. (1956). Quantum theory. *Annual Review of Physical Chemistry*, 7:107–136.

[79] Murray, P. and (the late) J.W. Linnett (1976a). Cation distribution in the spinels $CoxFe_{3-x}O_4$. *Journal of Physics and Chemistry of Solids*, 37(11):1041–1042.

[80] Murray, P. and (the late) J.W. Linnett (1976b). Mössbauer studies in the spinel system $Co_xFe_{3-x}O_4$. *Journal of Physics and Chemistry of Solids*, 37(6):619 –624.

[81] Mączka, M., Ptak, M., Kurnatowska, M., and Hanuza, J. (2013). Synthesis, phonon and optical properties of nanosized $CoCr_2O_4$. *Materials Chemistry and Physics*, 138(2-3):682–688.

[82] N. Menyuk, K. D. e. A. W. (1965). Ferrimagnetic spiral configurations in cobalt chromite. *J. Phys. France*, 25:528–536.

[83] Navrotsky, A. and Kleppa, O. (1967). The thermodynamics of cation distributions in simple spinels. *Journal of Inorganic and Nuclear Chemistry*, 29(11):2701–2714.

[84] Ndione, P. F., Shi, Y., Stevanovic, V., Lany, S., Zakutayev, A., Parilla, P. A., Perkins, J. D., Berry, J. J., Ginley, D. S., and Toney, M. F. (2014). Control of the electrical properties in spinel oxides by manipulating the cation disorder. *Advanced Functional Materials*, 24(5):610–618.

[85] Neubeck, W., Vettier, C., Fernandez, V., de Bergevin, F., and Giles, C. (1999). Observation of orbital moment in NiO using magnetic X-ray scattering. *Journal of Applied Physics*, 85(8):4847–4849.

[86] O'Neill, H. S., James, M., Dollase, W. A., and Redfern, S. A. T. (2005). Temperature dependence of the cation distribution in $CuAl_2O_4$ spinel. *European Journal of Mineralogy*, 17(4):581–586.

[87] O'Neill, H. S. C. and Navrotsky, A. (1983). Simple spinels; crystallographic parameters, cation radii, lattice energies, and cation distribution. *American Mineralogist*, 68(1-2):181–194.

[88] Padam, R., Pandya, S., Ravi, S., Grover, A. K., and Pal, D. (2013a). Exchange bias effect in $Co(Cr_{0.925}Fe_{0.075})_2O_4$. *AIP Conference Proceedings*, 1512(1):1112–1113.

[89] Padam, R., Pandya, S., Ravi, S., Nigam, A. K., Ramakrishnan, S., Grover, A. K., and Pal, D. (2013b). Magnetic compensation effect and phase reversal of exchange bias field across compensation temperature in multiferroic $Co(Cr_{0.95}Fe_{0.05})_2O_4$. *Applied Physics Letters*, 102(11):112412.

[90] Palin, E. J., Walker, A. M., and Harrison, R. J. (2008). A computational study of order-disorder phenomena in Mg_2TiO_4 spinel (qandilite). *American Mineralogist*, 93:1363–1372.

[91] Perdew, J. P., Burke, K., and Ernzerhof, M. (1996). Generalized Gradient Approximation made simple. *Phys. Rev. Lett.*, 77:3865–3868.

[92] Perdew, J. P., Ruzsinszky, A., Csonka, G. I., Vydrov, O. A., Scuseria, G. E., Constantin, L. A., Zhou, X., and Burke, K. (2008). Restoring the density-gradient expansion for exchange in solids and surfaces. *Phys. Rev. Lett.*, 100:136406.

[93] Pickett, W. E., Erwin, S. C., and Ethridge, E. C. (1998). Reformulation of the LDA + U method for a local-orbital basis. *Phys. Rev. B*, 58:1201–1209.

[94] Ptak, M., Mączka, M., Hermanowicz, K., Pikul, A., and Hanuza, J. (2013). Particle size effects on the magnetic and phonon properties of multiferroic $CoCr_2O_4$. *Journal of Solid State Chemistry*, 199:295–304.

[95] Ptak, M., Mączka, M., Pikul, A., Tomaszewski, P., and Hanuza, J. (2014). *Journal of Solid State Chemistry*, 212:218–226.

[96] Rajender, P. (2014). *Study of Magnetic Properties and Exchange Bias in* $CoCr_{1-x}M_xO_4$,*(*$M = Fe$,Co *and* Al*)*. PhD thesis, IIT Guwahati, Department of Physics Indian Institute of Technology Guwahati, Guwahati-781 039, Assam, India.

[97] Rudolf, T., Kant, C., Mayr, F., Hemberger, J., Tsurkan, V., and Loidl, A. (2007). Spin-phonon coupling in antiferromagnetic chromium spinels. *New Journal of Physics*, 9(3):76.

[98] Sandratskii, L. M. (1998). Noncollinear magnetism in itinerant-electron systems: Theory and applications. *Advances in Physics*, 47(1):91–160.

[99] Santos-Carballal, D., Roldan, A., Grau-Crespo, R., and de Leeuw, N. H. (2015). First-principles study of the inversion thermodynamics and electronic structure of FeM_2X_4 (thio)spinels (M=Cr, Mn,Co, Ni; X=O, S). *Phys. Rev. B*, 91:195106.

[100] Savrasov, S. Y. (1996). Linear-response theory and lattice dynamics: A muffin-tin-orbital approach. *Phys. Rev. B*, 54:16470–16486.

[101] Schwarz, L., Galazka, Z., Gesing, T. M., and Klimm, D. (2015). On the influence of inversion on thermal properties of magnesium gallium spinel. *Crystal Research and Technology*, 50(12):961–966.

[102] Seko, A., Oba, F., and Tanaka, I. (2010). Classification of spinel structures based on first-principles cluster expansion analysis. *Phys. Rev. B*, 81:054114.

[103] Seminovski, Y., Palacios, P., Wahnón, P., and Grau-Crespo, R. (2012). Band gap control via tuning of inversion degree in $CdIn_2S_4$ spinel. *Applied Physics Letters*, 100(10):102112.

[104] Shannon, R. D. (1976). Revised effective ionic radii and systematic studies of interatomic distances in halides and chalcogenides. *Acta Crystallographica Section A*, 32(5):751–767.

[105] Shirane, G., Cox, D. E., and Pickart, S. J. (1964). Magnetic structures in $FeCr_2S_4$ and $FeCr_2O_4$. *Journal of Applied Physics*, 35(3):954–955.

[106] Sickafus, K., Larson, A., Yu, N., Nastasi, M., Hollenberg, G., Garner, F., and Bradt, R. (1995). Cation disorder in high dose, neutron-irradiated spinel. *Journal of Nuclear Materials*, 219:128–134. Fabrication and Properties of Ceramics for Fusion Energy.

[107] Sickafus, K. E., Wills, J. M., and Grimes, N. W. (1999). Structure of spinel. *Journal of the American Ceramic Society*, 82(12):3279–3292.

[108] Sinha, A. P. B., Sanjana, N. R., and Biswas, A. B. (1957). On the structure of some anganites. *Acta Crystallographica*, 10(6):439–440.

[109] Slater, J. C. (1937). Wave functions in a periodic potential. *Phys. Rev.*, 51:846–851.

[110] Slonczewski, J. (1996). Current-driven excitation of magnetic multilayers. *Journal of Magnetism and Magnetic Materials*, 159(1):L1–L7.

[111] Smith, P., Spencer, C., and Stillwell, R. (1978). Co57 and Fe57 mössbauer studies of the spinels $FeCo_2O_4$ and $Fe_{0.5}Co_{2.5}O_4$. *Journal of Physics and Chemistry of Solids*, 39(2):107–111.

[112] Solovyev, I., Hamada, N., and Terakura, K. (1996). t_{2g} versus all 3d localization in $LaMO_3$ perovskites ($M = Ti - Cu$): First-principles study. *Phys. Rev. B*, 53:7158–7170.

[113] Soven, P. (1967). Coherent-potential model of substitutional disordered alloys. *Phys. Rev.*, 156:809–813.

[114] Starkloff, T. and Joannopoulos, J. D. (1977). Local pseudopotential theory for transition metals. *Phys. Rev. B*, 16:5212–5215.

[115] Stig, A. (1965). On the structure of the spinel $CuMn_2O_4$. *Acta Chemica Scandinavica*, 19(1706):1706.

[116] Sushkov, A. B., Tchernyshyov, O., II, W. R., Cheong, S. W., and Drew, H. D. (2005). Probing spin correlations with phonons in the strongly frustrated magnet $ZnCr_2O_4$. *Phys. Rev. Lett.*, 94:137202.

[117] Szotek, Z., Temmerman, W. M., Ködderitzsch, D., Svane, A., Petit, L., and Winter, H. (2006). Electronic structures of normal and inverse spinel ferrites from first principles. *Phys. Rev. B*, 74:174431.

[118] Takahashi, M. and Fine, M. E. (1972). Magnetic behavior of quenched and aged $CoFe_2O_4$-Co_3O_4 alloys. *Journal of Applied Physics*, 43(10):4205–4216.

[119] Tarascon, J.-M. and Armand, M. (2001). Issues and challenges facing rechargeable lithium batteries. *Nature*, 414(6861):359–367.

[120] Teillet, J., Bouree, F., and Krishnan, R. (1993). Magnetic structure of $CoFe_2O_4$. *Journal of Magnetism and Magnetic Materials*, 123(1):93 –96.

[121] Tielens, F., Calatayud, M., Franco, R., Recio, J. M., Perez-Ramirez, J., , and Minot, C. (2006). Periodic dft study of the structural and electronic properties of bulk CoAl_2O_4 spinel. *The Journal of Physical Chemistry B*, 110(2):988–995.

[122] Tishin, A. and Spichkin, Y. (2003). *The Magnetocaloric Effect and its Applications*. IOP.

[123] Tokura, Y. and Nagaosa, N. (2000). Orbital physics in transition-metal oxides. *Science*, 288(5465):462–468.

[124] Tomiyasu, K., Fukunaga, J., and Suzuki, H. (2004). Magnetic short-range order and reentrant-spin-glass-like behavior in $CoCr_2O_4$ and $MnCr_2O_4$ by means of neutron scattering and magnetization measurements. *Phys. Rev. B*, 70:214434.

[125] Topp, W. C. and Hopfield, J. J. (1973). Chemically motivated pseudopotential for sodium. *Phys. Rev. B*, 7:1295–1303.

[126] Torgashev, V. I., Prokhorov, A. S., Komandin, G. A., Anzin, E. S. Z. B., Talanov, V. M., Bush, L. M. R. A., Dressel, M., and Gorshunov, B. P. (2012). Magnetic and dielectric response of cobalt-chromium spinel $CoCr_2O_4$ in the terahertz frequency range. *Physics of the Solid State*, 54:350.

[127] Tsurkan, V., Zherlitsyn, S., Yasin, S., Felea, V., Skourski, Y., Deisenhofer, J., von Nidda, H.-A. K., Wosnitza, J., and Loidl, A. (2013). Unconventional magnetostructural transition in $CoCr_2O_4$ at high magnetic fields. *Phys. Rev. Lett.*, 110:115502.

[128] Turek, I., Drchal, V., Kudrnovsky, J., Sob, M., and Weinberger, P. (1997). *Electronic Structure of Disordered Alloys, Surfaces and Interfaces*. Springer.

[129] Uberuaga, B. P., Bacorisen, D., Smith, R., Ball, J. A., Grimes, R. W., Voter, A. F., and Sickafus, K. E. (2007). Defect kinetics in spinels: Long-time simulations of $MgAl_2O_4$,$MgGa_2O_4$ and $MgIn_2O_4$. *Phys. Rev. B*, 75:104116.

[130] Vanderbilt, D. (1990). Soft self-consistent pseudopotentials in a generalized eigenvalue formalism. *Phys. Rev. B*, 41:7892–7895.

[131] Vitos, L. (2001). Total-energy method based on the exact muffin-tin orbitals theory. *Phys. Rev. B*, 64:014107.

[132] Webster, P. J., Ziebeck, K. R. A., Town, S. L., and Peak, M. S. (1984). Magnetic order and phase transformation in Ni_2MnGa. *Philosophical Magazine Part B*, 49(3):295–310.

[133] Weidenborner, J. E., Stemple, N. R., and Okaya, Y. (1966). Cation distribution and oxygen parameter in magnesium gallate, $MgGa_2O_4$. *Acta Crystallographica*, 20(6):761–764.

[134] Wickham, D. and Croft, W. (1958). Crystallographic and magnetic properties of several spinels containing trivalent ja-1044 manganese. *Journal of Physics and Chemistry of Solids*, 7(4):351–360.

[135] Wickham, D. G. and Goodenough, J. B. (1959). Suggestion concerning magnetic interactions in spinels. *Phys. Rev.*, 115:1156–1158.

[136] Wickham, D. G. and Goodenough, J. B. (1963). *Magnetism and the Chemical Bond*. Inter-science, New York.

[137] Wills, A. S., Raju, N. P., and Greedan, J. E. (1999). Low-temperature structure and magnetic properties of the spinel LiMn2O4:a frustrated antiferromagnet and cathode material. *Chemistry of Materials*, 11(6):1510–1518.

[138] Wu, Z. and Cohen, R. E. (2006). More accurate generalized gradient approximation for solids. *Phys. Rev. B*, 73:235116.

[139] Yafet, Y. and Kittel, C. (1952). Antiferromagnetic arrangements in ferrites. *Phys. Rev.*, 87:290–294.

[140] Yamasaki, Y., Miyasaka, S., Kaneko, Y., He, J.-P., Arima, T., and Tokura, Y. (2006). Magnetic reversal of the ferroelectric polarization in a multiferroic spinel oxide. *Phys. Rev. Lett.*, 96:207204.

[141] Yokaichiya, F., Krimmel, A., Tsurkan, V., Margiolaki, I., Thompson, P., Bordallo, H. N., Buchsteiner, A., Stüßer, N., Argyriou, D. N., and Loidl, A. (2009). Spin-driven phase transitions in $ZnCr_2Se_4$ and $ZnCr_2S_4$ probed by high-resolution synchrotron X-ray and neutron powder diffraction. *Phys. Rev. B*, 79:064423.

[142] Zhang, H. G., Wang, W. H., Liu, E. K., Tang, X. D., Li, G. J., Zhang, H. W., and Wu, G. H. (2013). Compensation effect and magnetostriction in $CoCr_{2-x}Fe_xO_4$. *physica status solidi (b)*, 250(7):1287–1292.

[143] Zhang, H. G., Wang, Z., Liu, E. K., Wang, W. H., Yue, M., and Wu, G. H. (2015). Site preference and compensation behavior in $Co(Cr,Mn)_2O_4$ system. *Journal of Applied Physics*, 117(17):17B735.

[144] Zhang, Y. and Yang, W. (1998). Comment on “Generalized Gradient Approximation made simple”. *Phys. Rev. Lett.*, 80:890–890.

[145] Zhou, N., Buchholz, D. B., Zhu, G., Yu, X., Lin, H., Facchetti, A., Marks, T. J., and Chang, R. P. H. (2014). Ultraflexible polymer solar cells using amorphous zinc-indium-tin oxide transparent electrodes. *Advanced Materials*, 26(7):1098–1104.

Publication in international journals

1. Debashish Das and Subhradip Ghosh : *Density functional theory based comparative study of electronic structures and magnetic properties of spinel* ACr_2O_4 *(A = Mn, Fe, Co, Ni) compounds*, J. Phys. D: Appl. Phys, vol.**48**, (2015) 425001

2. Debashish Das, Rajkumar Biswas and Subhradip Ghosh : *Systematic analysis of structural and magnetic properties of spinel* CoB_2O_4 *(B=Cr, Mn and Fe) compounds from their electronic* , J. Phys.: Condens. Matter, vol. **28** (2016) 446001

3. Debashish Das, Shreemoyee Ganguly, Biplab Sanyal and Subhradip Ghosh : *Effect of Fe doping in the structural, electronic and magnetic properties of* $CoCr_2O_4$ *: insights from ab initio calculations*, Mater. Res. Express, vol. **3** (2016) 106106

4. Debashish Das and Subhradip Ghosh: *First-principles investigations into the thermodynamics of cation disorder and its impact on electronic structure and magnetic properties of spinel* $Co(Cr_{1-x}Mn_x)_2O_4$, J. Phys.: Condens. Matter, vol. **29** (2017) 055805

Communicated in international journals

1. Debashish Das and Subhradip Ghosh : *Site occupancies and their effects on the physical properties of spinel* $Co\,(Cr_{1-x}Fe_x)_2\,O_4$*: an ab initio study*

2. Debashish Das, Biplab Sanyal and Subhradip Ghosh : *Vibrational properties of Fe and Mn substituted* $CoCr_2O_4$

Publications that are not part of the thesis

1. Ram Kumar, R. Padam, Debashish Das, S. Rayaprol, V. Siruguri and D. Pal: *Low temperature neutron diffraction studies on* $Co(Cr_{1-x}Fe_x)_2O_4$ *(x = 0.05 and 0.075)*, RSC Adv., vol. **6**,(2016) 93511

भारतीय प्रौद्योगिकी संस्थान गुवाहाटी
Indian Institute of Technology Guwahati